EXAMINING THE ROLE OF SEA ICE AND METEOROLOGY IN ARCTIC BOUNDARY LAYER HALOGEN CHEMISTRY

By

Peter Kevin Peterson

RECOMMENDED:

Dr. Thomas Douglas

Dr. Carl Tape

Dr. Thomas Trainor

Dr. William Simpson
Advisory Committee Chair

Dr. Thomas Green
Chair, Department of Chemistry and Biochemistry

APPROVED:

Dr. Paul Layer
Dean, College of Natural Science and Mathematics

Dr. John Eichelberger
Dean of the Graduate School

24 April 2015
Date

EXAMINING THE ROLE OF SEA ICE AND METEOROLOGY IN ARCTIC BOUNDARY LAYER HALOGEN CHEMISTRY

A

DISSERTATION

Presented to the Faculty

of the University of Alaska Fairbanks

in Partial Fulfillment of the Requirements

for the Degree of

DOCTOR OF PHILOSOPHY

By

Peter Kevin Peterson, B.S.

Fairbanks, Alaska

May 2015

Abstract

Given the ubiquitous nature of ice, chemistry taking place on ice surfaces has a substantial effect on the environment, particularly in the polar regions. The return of sunlight to the polar regions releases halogen radicals (e.g. Br, Cl and their oxides, e.g. BrO) generated from salts on ice surfaces. These radicals fundamentally alter the chemistry of the Arctic boundary layer through processes such as boundary-layer ozone depletion events and mercury deposition events.

Current understanding of the chemical processes involved in Arctic halogen chemistry is inhibited by a lack of knowledge about the ice surfaces on which this chemistry is thought to take place, as well as the sparsity of long-term field observations of this chemistry and its effects. This dissertation addresses both needs through a combination of laboratory experiments and long-term field studies. First, we use X-ray absorption computed micro-tomography at the Advanced Photon Source to image brine distributions within laboratory grown mimics of sea-ice features. These experiments showed that when brine is introduced to ice via wicking of brine from a saline surface, the resulting brine distribution is heterogeneous, with brine existing in distinct regions within the sample, rather than evenly spreading over the sample surface. To examine the horizontal and vertical extent of halogen chemistry in the Arctic boundary layer, we conducted long-term measurements of BrO at Barrow, Alaska using Multiple-Axis Differential Optical Absorption Spectroscopy (MAX-DOAS). We developed a method to reduce these measurements to timeseries of near-surface and total column amounts of BrO. These measurements showed that the vertical distribution is highly variable, ranging from shallow layer events confined to the lowest 200 m, to distributed column events, which have lower mixing ratios of BrO, but are more distributed throughout approximately the lowest kilometer of the atmosphere. We find that the observed vertical distributions of BrO are influenced by atmospheric stability. We found minimal influence of wind speed on either lower-tropospheric bromine activation (LT-VCD) or the vertical distribution of BrO, while examination of seasonal trends and the temperature dependence of the vertical distribution support the finding that atmospheric stability affects the distribution of BrO. While shallow layer events have higher concentrations of halogens, distributed column events tend to have higher overall amounts of activation, implying that in situ near surface measurements may be insufficient to constrain the role of environmental parameters in the activation of halogens. Examination of multiple years of data at Barrow, Alaska shows that time spent in first year ice (FYI) areas is weakly linearly correlated (R=0.38) with the activation of BrO. However, examining annual averages of BrO shows that despite the non-linear relationship between time in FYI areas and BrO, time spent in FYI areas still influences the interannual variability of BrO.

Table of Contents

Page

List of Figures

Page

List of Tables

List of Appendices

Acknowledgements

I would like to begin by thanking my advisor Bill Simpson, whose encouragement, guidance, and patience were invaluable in the completion of this project. I would also like to thank my committee members; Tom Douglas, Carl Tape, and Tom Trainor all provided valuable input throughout the completion of this dissertation. Working in the Simpson and Trainor labs has provided daily encouragement and guidance, particularly from Chris Iceman, Erin Gleason, Franta Majs, and Nastia Ilgen.

This project has given me the opportunity to collaborate with many excellent scientists. In particular, I would to thank Mark Rivers and the staff of the GSECARS facility at the Advanced Photon Source for their assistance acquiring and analyzing the tomographic data presented in Chapter 2 of this work. Udo Frieß, Johannes Zielcke, and Uli Platt at the Institute for Environmental Physics provided invaluable assistance with the analysis of the MAX-DOAS data presented in Chapters 3 and 4 of this dissertation. Chapter 3 was improved through collaboration with Kerri Pratt, Paul Shepson, Udo Frieß, Johannes Zielcke, Uli Platt, Steve Walsh, and Son Nghiem.

Working in the Arctic has been one of the most rewarding and challenging experiences of my career. I am grateful for assistance of the scientists and crew aboard the CCGS Louis St Laurent, particularly Carlton Rauschenberg and Kris Newhall who took the time to assist and educate me on the particulars of deploying complex instrumentation in remote regions.

Financial support for this work was provided by the National Aeronautics and Space Administration (NASA) Cryospheric Sciences Program, and the National Science Foundation under grant ARC-1023118.

Lastly, I would like to thank my friends and family, first and foremost my wife Holly, who have supported me during this process. My experience at UAF has been filled with great people and I could not possibly name them all here, but their support is appreciated nonetheless.

Chapter 1
Introduction

1.1 Introduction and Motivation

A key process in the removal of various pollutants from the atmosphere is oxidation. In most places, atmospheric oxidation chemistry is driven by ozone photochemistry and the production of hydroxyl radicals. In the Arctic, photochemistry rates of reaction are drastically reduced with the lack of available sunlight during the polar winter. Recent studies have shown that other oxidation mechanisms involving halogen chemistry on ice surfaces play a critical role in determining the fate of pollutants in the Arctic atmosphere (Abbatt et al. (2012) and references therein). While the Arctic is relatively free of anthropogenic pollution sources, long range transport of various pollutants emitted in more populated areas at lower latitudes via mechanisms such as the "Grasshopper" effect (Wania and Mackay, 1996) means that understanding the fate and deposition rates of atmospheric contaminants in the Arctic is critical. The Arctic climate is undergoing rapid changes (Jeffries et al., 2013), and it is imperative that we understand the implications of these changes for the chemistry of the Arctic atmosphere.

Polar sunrise in the Arctic has been associated with production of reactive halogens (e.g. Br, BrO) from sea salt (Abbatt et al., 2012). Multiple studies have detailed the influence of halogen chemistry on the Arctic environment through processes such as boundary-layer ozone depletion events (ODE) (Barrie et al., 1988; Simpson et al., 2007b) and mercury deposition events (MDE) (Schroeder et al., 1998; Steffen et al., 2008). While the production of these halogens is not fully understood, it is thought to be linked to heterogeneous chemistry taking place on saline ice surfaces (e.g saline snow, first year sea ice areas)(Dominé and Shepson, 2002; Abbatt et al., 2012). The conditions required for halogen activation and bromine explosion chemistry are the subject of debate in the literature. Proposed sources of halogens include frost flowers (e.g. Rankin et al., 2002; Kaleschke et al., 2004), saline snow (e.g. Dominé et al., 2004; Simpson et al., 2007a; Pratt et al., 2013; Wren et al., 2013), and blowing snow events (e.g. Yang et al., 2008; Jones et al., 2010; Frieß et al., 2011). Large geographic-scale correlations between first year ice areas and halogen activation have been observed (e.g. Wagner et al., 2001; Frieß, 2004; Simpson et al., 2007a; Nghiem et al., 2012). Given the rapidly changing nature of Arctic sea ice (Nghiem et al., 2007; Kwok, 2007; Maslanik et al., 2011), it is imperative to understand the link between sea ice, particularly first year ice, and halogen chemistry, to fully understand the implications of changes in Arctic sea ice coverage for the chemical composition of the Arctic boundary layer. This dissertation addresses key roadblocks to understanding these halogen activation processes fully and the relative contributions of proposed sources by examining the microstructure (10 micro-meter scale) of surfaces on which these reactions take place and analysis of long term measurements of BrO

throughout the Arctic. This microstructure analysis is done through the use of X-ray absorption computed microtomography (CMT) to image brine distributions on vapor-deposited ice surfaces. To observe relationships between halogen activation and environmental conditions in the field, we measure long timeseries of BrO using multiple axis differential optical absorption spectroscopy (MAX-DOAS).

1.2 Boundary Layer Ozone Depletion Events

Oxidation of pollutants in the atmosphere occurs largely through reactions with hydroxyl radicals, which are formed from the photolysis of ozone (Thompson, 1992). With the return of sunlight in the polar spring, ozone in the Arctic boundary-layer becomes episodically depleted from background levels of 30-40 nmol mol^{-1} to near-zero levels, altering the oxidation of pollutants in the Arctic such as mercury (Schroeder et al., 1998) and non-methyl hydrocarbons (e.g. Jobson et al., 1994; Read et al., 2007). This boundary-layer ozone depletion was first observed in the early 1980s (Oltmans, 1981) and linked to reactive bromine chemistry soon after by Barrie et al. (1988).

Bromine atoms react with ozone (R1) to form BrO. By itself, this reaction does not deplete ozone, because most often BrO is rapidly photolysed (R2), which in combination with R1 causes a rapid interconversion between bromine atoms Br and bromine monoxide BrO. Because there is a rapid interconversion between these two species, we refer to sum of Br and BrO as reactive bromine, or BrO_x. While the combination of these two reactions does not deplete ozone, some BrO can react with itself via R3, in what is known as a "self-reaction", forming molecular oxygen and bromine molecules. This results in a net depletion of ozone while conserving reactive bromine. Molecular bromine is rapidly photolysed (R4) to re-create active bromine.

$$Br + O_3 \rightarrow BrO + O_2 \quad \text{(R1)}$$

$$BrO + h\nu \xrightarrow{O_2} Br + O_3 \quad \text{(R2)}$$

$$BrO + BrO \rightarrow Br_2 + O_2 \quad \text{(R3)}$$

$$Br_2 + h\nu \rightarrow 2Br \quad \text{(R4)}$$

These episodic boundary-layer ozone depletion events (ODE) have been linked to sea ice regions (e.g Bottenheim and Chan, 2006; Gilman et al., 2010; Oltmans et al., 2012), and Oltmans et al. (2012) found the prevalence of ODEs during springtime at Barrow, Alaska has been increasing in recent years.

1.3 Mercury Deposition Events

Mercury (Hg) is ubiquitous in the earth's crust and begins to impact the environment when emitted via natural (e.g. volcanic emission, biomass burning) or anthropogenic (e.g. coal burning, other industrial uses) processes, as gaseous elemental mercury (GEM). Elemental mercury's high volatility allows it to be easily transported. In the atmosphere, GEM typically has a residence time of about a year; however, when oxidized to Hg(II) this lifetime is reduced to timescales on the order of weeks (Steffen et al., 2008). Only 20% of mercury emitted in the US winds up deposited in the US (Selin et al., 2007), implying that the oxidative properties and local weather play more of a role in determining local deposited concentrations than local emissions. At lower latitudes, mercury can be re-emitted and continue to be transported (Strode et al., 2007). Once deposited, Hg(II) can be methylated and enter the food chain, where it readily bio-accumulates.

Measurements of total gaseous mercury and dissolved gaseous mercury in the Arctic Ocean show that the concentration of mercury is enhanced in the Arctic Ocean compared to the North Atlantic. Possible explanations are the sea ice pack inhibiting air/liquid exchange of gaseous mercury, river discharge (Fisher et al., 2012), or enhanced mercury deposition rates (Andersson et al., 2008). The first observations of mercury depletion events in the Arctic were first reported in 1998 (Schroeder et al., 1998) and subsequently found to be a regular springtime occurrence like boundary-layer ozone depletion and photochemical activation of halogens (Steffen et al., 2008). The link between MDEs and boundary-layer ozone depletion events (ODE) suggests a link between MDEs and halogen chemistry (Schroeder et al., 1998; Lu et al., 2001).

This halogen chemistry results in abnormally large mercury concentrations in Arctic snow (1 to 2 orders of magnitude when compared to the rest of Alaska) (Douglas et al., 2005). Additionally, peaks in methyl mercury have been observed during spring runoff and snow melt implying that a large portion of methyl mercury production takes place in snow and enters the food web in pulses during spring melt (Steffen et al., 2008). Given the changing ice conditions in the Arctic, it is thought that deposition rates in the Arctic could increase in the future due to an increased flux of halogens from an ice pack more dominated by saline first year sea ice areas.

Methyl mercury is highly toxic, causing neurological impairment, decreased lung and heart function, and impaired neurological development in infants. Seafood and marine mammals are the primary source for methyl mercury in humans, which is particularly problematic in the Arctic where Hg levels in Arctic native populations are very high due to higher deposition rates and the reliance of native populations on subsistence hunting. Tian et al. (2011) found that, for Inuit in northern Canada, 59% of the children exceeded the WHO intake level for children.

1.4 Reactive Bromine Chemistry

Given the bromine radicals are highly reactive, they participate in reactions other than those listed above. Some of these reactions serve to convert reactive bromine species (BrO_x) to other less reactive "reservoir" bromine species such as HBr and HOBr (See R5 and R7).

$$Br + HO_2 \rightarrow HOBr + O_2 \quad \text{(R5)}$$

These bromine species do not directly participate in oxidation of pollutants, but can re-release BrO_x, so we refer to them as reservoir species. Reservoir species can be re-converted to reactive bromine, either by the rapid photolysis of HOBr (R6), or through heterogeneous reactions as discussed below.

$$HOBr + h\nu \rightarrow OH + Br \quad \text{(R6)}$$

Sometimes conversion to reservoir species acts as a sink of reactive bromine. An example is the reaction of bromine with formaldehyde shown in R7.

$$Br + CH_2O \rightarrow HBr + CHO \quad \text{(R7)}$$

While the resulting HBr can react with the hydroxyl radical to release reactive bromine (R8), more often HBr undergoes deposition to aerosol particles removing it from atmospheric chemical processes.

$$HBr + OH \rightarrow Br + H_2O \quad \text{(R8)}$$

The net result can be sufficient to remove reactive bromine from the atmosphere and terminate ozone depleting chemistry. However, the deposition of HBr to the snowpack does increase the Br^- to Cl^- ratio which improves the ability of the snowpack to participate in later bromine activation (Pratt et al., 2013). Most likely, processes on atmospheric aerosol particles mimic snowpack processes, so deposition of HBr to particles may enhance atmospheric reactivation of bromine.

1.5 Role of Ice Surfaces

Because the normal lifetime of BrO_x is on the order of hours (Platt and Hönninger, 2003), and the depletion of ozone takes place on day timescales (Hausmann and Platt, 1994), it is likely that bromine must be being converted from reservoir species to reactive bromine (recycled) through heterogeneous reactions (McConnell et al., 1992; Platt and Hönninger, 2003) on aerosol particles

or ice surfaces.

$$HOBr_{(aq)} + Br^-_{(aq)} + H^+_{(aq)} \rightarrow Br_2 + H_2O \quad \text{(R9)}$$

This hypothesis is reinforced by the inability of modeling based solely on gas phase chemistry to explain observed rates of boundary-layer ozone depletion. R9 is also the mechanism by which bromide in the brine becomes gas phase bromine which can then be photolysed (R4) to produce bromine radicals. Some of these bromine radicals can then participate in R5 to keep the process going, resulting in a net release of bromide from the brine because the combination of R9 and R4 produces two bromine atoms, only one of which is required for R5. It should be pointed out that the production of HOBr via R5 is contingent on the presence of HO_2, which is consumed during R5.

As ice/brine systems freeze, thermodynamics dictates that brine will separate from the bulk ice, creating distinct areas of brine and ice (Bartels-Rausch et al., 2014). Many studies have examined the chemical behavior of the surfaces resulting from this freezing process (e.g. Huff and Abbatt, 2000, 2002; Wren et al., 2010; Oldridge and Abbatt, 2011; Wren and Donaldson, 2012; Kahan et al., 2014). Additionally, because of the ability of frost flowers, a vapor deposited ice form commonly found in FYI regions, and snow to enhance the amount of ice surface participating in halogen activation, multiple studies have examined the surface area of these types of ice (e.g. Legagneux et al., 2002; Dominé et al., 2005). However, because field studies only provide information on the bulk composition of these systems (e.g. Dominé et al., 2004; Alvarez-Aviles et al., 2008; Krnavek et al., 2012), how much of this surface area actually participates in chemical processes is unclear. Multiple studies have found that aspects of the surface brine other than bromide concentration, such as pH (e.g. Huff and Abbatt, 2000; Wren et al., 2013) and bromide to chloride ratio, play a large role in the release of reactive bromine from snow and ice surfaces (Pratt et al., 2013).

1.6 Potential Sources of Reactive Bromine

1.6.1 Correlation with First Year Sea Ice Areas

Multiple studies in both the Arctic (e.g Bottenheim and Chan, 2006; Simpson et al., 2007a; Gilman et al., 2010; Frieß et al., 2011; Oltmans et al., 2012) and Antarctic (e.g. Frieß, 2004; Jones et al., 2006; Wagner et al., 2007) have implicated sea ice regions, specifically first year ice regions (FYI), which tend to be more saline, in halogen activation and ozone depletion chemistry. While all of these studies agree that FYI regions and the variety of snow and ice surfaces present in those regions play a significant role in the activation of BrO and subsequent depletion of ozone, there

are differing conclusions as to the degree of correlation between time spent in FYI regions and the amount of BrO observed. These differences in correlation could be due to the findings being based on short term field studies rather than long term measurements, or other confounding factors.

1.6.2 Saline Snow

Snow on sea ice wicks brine from the sea ice surface, enhancing the available surface area for halogen chemistry to take place (Dominé et al., 2004); however, wicking mostly contaminates the lower part of sea ice snowpacks. Halides can also be deposited on the top surface of the snow pack by aerosol particle deposition. The salinity of the snowpack is quite variable, with snow generally being more saline in FYI areas and less saline in ice areas that have survived a spring melt season (Krnavek et al., 2012). Work by Legagneux et al. (2002) showed that snow also has a high specific surface area, enhancing the available area for heterogeneous bromine chemistry to take place, although it is unlikely individual snow crystals are completely coated with brine (Dominé et al., 2013; Gleason, 2014). Observations by Stutz et al. (2011) showed that halogen chemistry is occurring in the snowpack at Summit, Greenland, which is far from oceanic bromine sources, indicating that snowpacks not associated with sea ice areas may also be sources of reactive bromine. Wren et al. (2013) and Pratt et al. (2013) also support the idea that the snowpack is a highly effective source of reactive halogens, although there are specific requirements for these surfaces such as acidic pH and enhanced bromide to chloride ratios for optimal release of halogens.

1.6.3 Frost Flowers

Frost flowers are a form of vapor deposited ice commonly observed on freshly frozen sea ice surfaces (Perovich and Richter-Menge, 1994). Frost flowers form on sublimating ice surfaces (Style and Worster, 2009), and are thought to influence the environment in a variety of ways (Barber et al., 2014), including the activation of halogens (Rankin et al., 2002). Given the changes currently occurring in Arctic sea ice regions, it is likely the abundance of frost flowers will change in the future (Douglas et al., 2012), making it important to characterize their role in boundary-layer chemistry. With regards to halogen chemistry, frost flowers are thought to be an effective halogen source due to their high bulk salinity, and specific surface area (SSA) (Rankin et al., 2002). However, multiple studies have raised potential issues with the consideration of frost flowers as a halogen source. Dominé et al. (2005) showed that while frost flowers do have an enhanced surface area compared to sea ice, they have a similar SSA to snow, which is much more prevalent in the Arctic. Kalnajs and Avallone (2006) showed that based on bulk composition measurements,

frost flower surfaces are likely too alkaline to facilitate halogen activation, which proceeds best in an acidic environment (Wren et al., 2010; Pratt et al., 2013). Kaleschke et al. (2004) developed a model for predicting potential areas of frost flowers from remote sensing data based on sea ice concentration and air temperatures. They showed that areas of potential frost flowers (PFF) were correlated with BrO in Antarctic regions, but similar studies in the Arctic (e.g. Simpson et al., 2007a; Frieß et al., 2011) showed little relationship between PFF areas and observed BrO. Modeling work by Piot and von Glasow (2008) showed that frost flowers alone can not explain regularly observed ODEs, and that recycling of halogens on the snow pack is required.

1.6.4 Blowing Snow

Blowing snow events happen frequently in the polar regions when higher wind speeds cause snow grains to separate from the surface snowpack, collide, fragment, and be lofted to higher altitudes. Recent literature has speculated that these events could enhance the surface area available for atmospheric chemistry as well as the vertical extent of this halogen chemistry (e.g. Jones et al., 2009, 2010; Yang et al., 2010; Frieß et al., 2011). This increase in the vertical extent is due either to reactions on the blowing snow itself, or aerosol particle production from sublimation of the blowing snow (Frieß et al., 2011). Because vertical profiling of reactive halogens in the boundary-layer is a recent development (Frieß et al., 2011), much of the available literature on blowing snow events is based on measurements of O_3 (e.g. Jones et al., 2009, 2010). The differing timescales of ozone depletion, recovery, and halogen activation complicate the use of ozone measurements to discuss halogen activation. Jones et al. (2009) used O_3 measurements to argue that two favorable regimes exist for ozone depletion. The first requires low wind speeds and a stable boundary-layer, the second requires high wind speeds to loft blowing snow. While this model worked for the observations in Jones et al. (2009), work by Halfacre et al. (2014) found no relation between O_3 and wind speed. Work by Yang et al. (2010) showed that satellite observations of the total BrO column could be reproduced using a simple model of blowing snow events and Frieß et al. (2011) observed that higher levels of BrO were usually associated with increases in aerosol particle extinction, strengthening the argument that lofted particles are necessary to observe large amounts of BrO.

1.7 Vertical Extent of ODE and halogen chemistry

Work examining the vertical extent of halogen events is fairly limited. However multiple axis differential optical absorption spectroscopy (MAX-DOAS) observations of BrO by Frieß et al. (2011) illustrate that vertical distribution of BrO is highly variable and similar to the vertical extent of ODEs. Given the similarities shown to exist, it is likely that past work on the vertical

extent of ODEs is relevant to halogen chemistry, despite the differing lifetimes of ozone (days) and reactive halogens (minutes in the absence of recycling). The vertical extent of ODEs is typically determined using ozone sondes, which are balloons tethered to an electrochemical instrument that measures ozone as the balloon ascends from the surface to the top of the stratosphere. These profiles are highly variable, with the ozone depleted region varying between 200 and 1000 m thickness (Bottenheim et al., 2002; Jones et al., 2010; Helmig et al., 2012; Oltmans et al., 2012). Oltmans et al. (2012) suggests these variations are tied to air mass origin. Both Tackett et al. (2007) and Moore et al. (2014) show that the levels of ozone observed near the surface are controlled by vertical mixing. In particular, Moore et al. (2014) found that mixing induced by open leads was found to cause recovery of ozone in ozone depleted air masses. Airborne measurements of BrO also showed enhanced vertical columns of BrO, which they interpret as arising from convective mixing over leads (McElroy et al., 1999). However, given the lack of profile measurements of halogens, the influence of lead induced vertical mixing on halogens remains an open question.

1.8 Satellite-based BrO Column Observations

Measurements of the BrO global total column clearly show that the Arctic during springtime is a regional hotspot (Wagner and Platt, 1998). Column measurements of BrO provide extensive temporal and spatial coverage of the Arctic (e.g. Wagner and Platt, 1998; Richter et al., 1998; Chance, 1998); however, they only measure the total column of BrO, exhibit decreased sensitivity in the lower regions of the atmosphere, and do not provide vertical profile information, complicating interpretation of satellite data when examining boundary-layer chemical processes. Stratospheric bromine is variable, and thus satellite BrO "hotspots" can not all be attributed to tropospheric bromine chemistry (Theys et al., 2009; Salawitch et al., 2010). While methods have been developed to separate the stratospheric and tropospheric components of BrO (e.g. Salawitch et al., 2010; Theys et al., 2011; Koo et al., 2012; Sihler et al., 2012), these techniques still suffer from problems with radiative transfer such as cloud masking. Additionally, derived tropospheric BrO partial columns are not yet available as an operational product for use by the broader community. In spite of these issues, satellite observations coupled with modeling have been used to explore multiple hypotheses about halogen activation (e.g. Wagner et al., 2001; Kaleschke et al., 2004; Yang et al., 2008; Nghiem et al., 2012). Wagner et al. (2001) used satellite BrO column observations in conjunction with remotely sensed sea ice data to show that BrO is usually found over areas predominantly composed of first year ice. Similarly, Kaleschke et al. (2004) used satellite column BrO and a model of potential frost flower areas to argue that frost flower contact played a large role in the activation of bromine. More recently, the focus has shifted to blowing snow events, in which a simple parametrization for blowing snow is combined with meteorological modeling to

show that satellite columns of BrO observed in the Arctic can be reproduced with a blowing snow source of halogens (Yang et al., 2008). Using a similar approach, Nghiem et al. (2012) recreated patterns observed in pan-Arctic satellite column BrO using a rising air parcel model in which open leads acted as bromine sources.

1.9 Role of Other Halogens

In 2009, Stephens et al. (2012) examined the relative contributions of various oxidants to MDEs at Barrow, Alaska. Several reactions involving chlorine, bromine, ozone, and the hydroxyl radical were studied. They observed that chlorine and bromine fluctuations were taking place independently, implying that they are participating in different chemistry. It is assumed that because chlorine reacts more readily with organic pollutants, bromine is primarily responsible for ozone depletion chemistry and MDEs. From this work, it is clear that chlorine contributes negligibly to MDEs when compared with bromine (Stephens et al., 2012).

Modeling work shows that iodine monoxide (IO) can potentially enhance the rate of boundary-layer ozone depletion when present in very small amounts (Saiz-Lopez et al., 2007). This enhancement in ozone depletion is primarily due to the reaction between BrO and IO being much faster than the reaction of BrO with itself. While field studies in the Antarctic (Saiz-Lopez et al., 2007) and Hudson Bay (Mahajan et al., 2010) have shown evidence of IO, there are no such results in the Arctic. Pöhler et al. (2010) investigated the possibility of IO in the Arctic using LP-DOAS, but did not observe any over the course of their campaign. However, due to the detection limitations of LP-DOAS, these measurements do not exclude the possibility of IO being present in quantities sufficient to increase rates of ozone depletion (Halfacre et al., 2014). More recently, Prados-Roman et al. (2015) used ship based MAX-DOAS measurements to argue that IO is present throughout the marine boundary-layer in quantities ranging from 0.4 to 1 pmol mol^{-1}, but again, IO in the Arctic boundary-layer has yet to be observed.

1.10 Dissertation Structure

Multiple field studies have provided limited BrO measurements in the boundary-layer over short time scales and at limited locations using a variety of techniques. The findings in these studies make it clear that substantial gaps remain in our understanding of halogen activation. This dissertation describes the use of X-Ray absorption tomography to study the surfaces on which this halogen activation chemistry takes place, as well as the use of multiple autonomous long-term measurement platforms to generate more data about the horizontal and vertical distribution of halogen events in the Arctic. These observations, carried out over unprecedented temporal and

spatial scales, will allow us to examine the influence of weather, ice dynamics, and varying ice surfaces on halogen activation events.

The subsequent chapters detail the results of these studies. Because subsequent chapters have been prepared as individual chapters for publication in peer-reviewed journals, some redundancy exists between this introduction and the introductory material for each chapter.

Chapter 2 describes the results of X-Ray computed microtomography of ice samples at the Advanced Photon Source (APS), Argonne National Laboratory. The goal of these measurements is to ascertain the location of salt elements on vapor-deposited ice that has been allowed to wick brine via capillary action from a saline ice surface. These studies will allow us to examine the chemically active surface area of brine covered ice surfaces to further define their role in the chemistry of the Arctic boundary-layer.

Chapter 3 examines the vertical structure of BrO observed using MAX-DOAS at Barrow, Alaska during the spring of 2012. In this chapter, we detail a procedure to reduce MAX-DOAS measurements to two quantities: the integrated vertical column from the surface through 200 m (VCD_{200m}), and the integrated vertical column from the surface through two km (LT-VCD). By examining the ratio of these two quantities, we can determine how the vertical structure of halogen activation events responds to meteorological factors such as temperature, wind speed, and atmospheric stability.

Chapter 4 uses four years of MAX-DOAS data from Barrow, Alaska, as well as data from drifting instrument packages (O-Buoys, (Knepp et al., 2010)) to examine the relationship between observed BrO LT-VCDs and contact with various ice types including areas that are predominantly first year sea ice (FYI), areas of multiyear ice, and areas of potential frost flowers. Previous studies have examined the relationship over shorter field campaigns (e.g. Frieß, 2004; Simpson et al., 2007a; Frieß et al., 2011) and came to varying conclusions about the degree correlation between time spent in FYI areas and BrO. By examining a longer timeseries, we hope to clarify the role of various types of ice in the activation and subsequent recycling of BrO.

Chapter 5 ties the results of these three studies together and discusses the broader impacts of the work detailed in this dissertation.

1.11 References

Abbatt, J. P. D., Thomas, J. L., Abrahamsson, K., Boxe, C., Granfors, A., Jones, A. E., King, M. D., Saiz-Lopez, A., Shepson, P. B., Sodeau, J., Toohey, D. W., Toubin, C., von Glasow, R., Wren, S. N., and Yang, X.: Halogen activation via interactions with environmental ice and snow in the polar lower troposphere and other regions, Atmospheric Chemistry and Physics, 12, 6237–6271, doi: 10.5194/acp-12-6237-2012, URL http://www.atmos-chem-phys.net/12/6237/2012/, 2012.

Alvarez-Aviles, L., Simpson, W. R., Douglas, T. A., Sturm, M., Perovich, D., and Dominé, F.: Frost flower chemical composition during growth and its implications for aerosol production and bromine activation, Journal of Geophysical Research, 113, 21 304, doi: 10.1029/2008JD010277, URL http://www.agu.org/pubs/crossref/2008/2008JD010277.shtml, 2008.

Andersson, M., Sommar, J., Gårdfeldt, K., and Lindqvist, O.: Enhanced concentrations of dissolved gaseous mercury in the surface waters of the Arctic Ocean, Marine Chemistry, 110, 190–194, doi: 10.1016/j.marchem.2008.04.002, URL http://linkinghub.elsevier.com/retrieve/pii/S0304420308000637, 2008.

Barber, D. G., Ehn, J. K., Pućko, M., Rysgaard, S., Deming, J. W., Bowman, J. S., Papakyriakou, T., Galley, R. J., and Søgaard, D. H.: Frost flowers on young Arctic sea ice: The climatic, chemical and microbial significance of an emerging ice type, Journal of Geophysical Research: Atmospheres, pp. n/a–n/a, doi: 10.1002/2014JD021736, URL http://doi.wiley.com/10.1002/2014JD021736, 2014.

Barrie, L. A., Bottenheim, J. W., Schnell, R. C., Crutzen, P. J., and Rasmussen, R. A.: Ozone destruction and photochemical reactions at polar sunrise in the lower Arctic atmosphere, Nature, 334, 138–141, doi: 10.1038/334138a0, URL http://www.nature.com/doifinder/10.1038/334138a0, 1988.

Bartels-Rausch, T., Jacobi, H.-W., Kahan, T. F., Thomas, J. L., Thomson, E. S., Abbatt, J. P. D., Ammann, M., Blackford, J. R., Bluhm, H., Boxe, C., Dominé, F., Frey, M. M., Gladich, I., Guzmán, M. I., Heger, D., Huthwelker, T., Klán, P., Kuhs, W. F., Kuo, M. H., Maus, S., Moussa, S. G., McNeill, V. F., Newberg, J. T., Pettersson, J. B. C., Roeselová, M., and Sodeau, J. R.: A review of air-ice chemical and physical interactions (AICI): liquids, quasi-liquids, and solids in snow, Atmospheric Chemistry and Physics, 14, 1587–1633, doi: 10.5194/acp-14-1587-2014, URL http://www.atmos-chem-phys.net/14/1587/2014/acp-14-1587-2014.html, 2014.

Bottenheim, J. W. and Chan, E.: A trajectory study into the origin of spring time Arctic boundary layer ozone depletion, Journal of Geophysical Research, 111, D19 301, doi: 10.1029/2006JD007055, URL http://doi.wiley.com/10.1029/2006JD007055, 2006.

Bottenheim, J. W., Fuentes, J. D., Tarasick, D. W., and Anlauf, K. G.: Ozone in the Arctic lower troposphere during winter and spring 2000 (ALERT2000), Atmospheric Environment, 36, 2535–2544, doi: 10.1016/S1352-2310(02)00121-8, URL http://www.sciencedirect.com/science/article/pii/S1352231002001218, 2002.

Chance, K.: Analysis of BrO measurements from the Global Ozone Monitoring Experiment, Geophysical Research Letters, 25, 3335–3338, doi: 10.1029/98GL52359, 1998.

Dominé, F. and Shepson, P. B.: Air-snow interactions and atmospheric chemistry., Science (New York, N.Y.), 297, 1506–10, doi: 10.1126/science.1074610, URL http://www.ncbi.nlm.nih.gov/pubmed/12202818, 2002.

Dominé, F., Sparapani, R., Ianniello, A., and Beine, H. J.: The origin of sea salt in snow on Arctic sea ice and in coastal regions, Atmospheric Chemistry and Physics, 4, 2259–2271, doi: 10.5194/acp-4-2259-2004, URL http://www.atmos-chem-phys.net/4/2259/2004/, 2004.

Dominé, F., Taillandier, A. S., Simpson, W. R., and Severin, K.: Specific surface area, density and microstructure of frost flowers, Geophysical Research Letters, 32, 2–5, doi: 10.1029/2005GL023245, URL http://www.agu.org/pubs/crossref/2005/2005GL023245.shtml, 2005.

Dominé, F., Bock, J., Voisin, D., and Donaldson, D. J.: Can we model snow photochemistry? Problems with the current approaches., The journal of physical chemistry. A, 117, 4733–49, doi: 10.1021/jp3123314, URL http://www.ncbi.nlm.nih.gov/pubmed/23597185, 2013.

Douglas, T. A., Sturm, M., Simpson, W. R., Brooks, S., Lindberg, S., and Perovich, D. K.: Elevated mercury measured in snow and frost flowers near Arctic sea ice leads, Geophysical Research Letters, 32, doi: 10.1029/2004GL022132, URL http://www.agu.org/pubs/crossref/2005/2004GL022132.shtml, 2005.

Douglas, T. A., Dominé, F., Barret, M., Anastasio, C., Beine, H. J., Bottenheim, J., Grannas, A., Houdier, S., Netcheva, S., Rowland, G., Staebler, R., and Steffen, A.: Frost flowers growing in the Arctic ocean-atmosphere-sea ice-snow interface: 1. Chemical composition, Journal of Geophysical Research, 117, D00R09, doi: 10.1029/2011JD016460, URL http://doi.wiley.com/10.1029/2011JD016460, 2012.

Fisher, J. A., Jacob, D. J., Soerensen, A. L., Amos, H. M., Steffen, A., and Sunderland, E. M.: Riverine source of Arctic Ocean mercury inferred from atmospheric observations, Nature Geoscience, 5, 499–504, doi: 10.1038/ngeo1478, URL http://dx.doi.org/10.1038/ngeo1478, 2012.

Frieß, U.: Dynamics and chemistry of tropospheric bromine explosion events in the Antarctic coastal region, Journal of Geophysical Research, 109, D06 305, doi: 10.1029/2003JD004133, URL http://doi.wiley.com/10.1029/2003JD004133, 2004.

Frieß U., Sihler, H., Sander, R., Pöhler, D., Yilmaz, S., and Platt, U.: The vertical distribution of BrO and aerosols in the Arctic: Measurements by active and passive differential optical absorption spectroscopy, Journal of Geophysical Research, 116, doi: 10.1029/2011JD015938, URL http://www.agu.org/pubs/crossref/2011/2011JD015938.shtml, 2011.

Gilman, J. B., Burkhart, J. F., Lerner, B. M., Williams, E. J., Kuster, W. C., Goldan, P. D., Murphy, P. C., Warneke, C., Fowler, C., Montzka, S. A., Miller, B. R., Miller, L., Oltmans, S. J., Ryerson, T. B., Cooper, O. R., Stohl, A., and de Gouw, J. A.: Ozone variability and halogen oxidation within the Arctic and sub-Arctic springtime boundary layer, Atmospheric Chemistry and Physics, 10, 10 223–10 236, doi: 10.5194/acp-10-10223-2010, URL http://www.atmos-chem-phys.org/10/10223/2010/acp-10-10223-2010.html, 2010.

Gleason, E.: Properties of sodium chloride brine on laboratory ice, Masters thesis, University of Alaska Fairbanks, 2014.

Halfacre, J. W., Knepp, T. N., Shepson, P. B., Thompson, C. R., Pratt, K. A., Li, B., Peterson, P. K., Walsh, S. J., Simpson, W. R., Matrai, P. A., Bottenheim, J. W., Netcheva, S., Perovich, D. K., and Richter, A.: Temporal and spatial characteristics of ozone depletion events from measurements in the Arctic, Atmospheric Chemistry and Physics, 14, 4875–4894, doi: 10.5194/acp-14-4875-2014, URL http://www.atmos-chem-phys.net/14/4875/2014/acp-14-4875-2014.html, 2014.

Hausmann, M. and Platt, U.: Spectroscopic measurement of bromine oxide and ozone in the high Arctic during Polar Sunrise Experiment 1992, Journal of Geophysical Research, 99, 25 399, doi: 10.1029/94JD01314, URL http://doi.wiley.com/10.1029/94JD01314, 1994.

Helmig, D., Boylan, P., Johnson, B., Oltmans, S., Fairall, C., Staebler, R., Weinheimer, A., Orlando, J., Knapp, D. J., Montzka, D. D., Flocke, F., Frieß, U., Sihler, H., and Shepson, P. B.: Ozone dynamics and snow-atmosphere exchanges during ozone depletion events at Barrow, Alaska, Journal of Geophysical Research: Atmospheres, 117, doi: 10.1029/2012JD017531, URL http://doi.wiley.com/10.1029/2012JD017531, 2012.

Huff, A. K. and Abbatt, J. P. D.: Gas-Phase Br_2 Production in Heterogeneous Reactions of Cl_2 , HOCl, and BrCl with Halide-Ice Surfaces, The Journal of Physical Chemistry A, 104, 7284–7293, doi: 10.1021/jp001155w, URL http://pubs.acs.org/doi/abs/10.1021/jp001155w, 2000.

Huff, A. K. and Abbatt, J. P. D.: Kinetics and Product Yields in the Heterogeneous Reactions of HOBr with Ice Surfaces Containing NaBr and NaCl, The Journal of Physical Chemistry A, 106, 5279–5287, doi: 10.1021/jp014296m, URL http://pubs.acs.org/doi/abs/10.1021/jp014296m, 2002.

Jeffries, M., Richter-Menge, J., and Overland, J.: Arctic Report Card, 2013.

Jobson, B. T., Niki, H., Yokouchi, Y., Bottenheim, J., Hopper, F., and Leaitch, R.: Measurements of C 2 -C 6 hydrocarbons during the Polar Sunrise1992 Experiment: Evidence for Cl atom and Br atom chemistry, Journal of Geophysical Research, 99, 25 355, doi: 10.1029/94JD01243, URL http://doi.wiley.com/10.1029/94JD01243, 1994.

Jones, A. E., Anderson, P. S., Wolff, E. W., Turner, J., Rankin, A. M., and Colwell, S. R.: A role for newly forming sea ice in springtime polar tropospheric ozone loss? Observational evidence from Halley station, Antarctica, Journal of Geophysical Research, 111, D08 306, doi: 10.1029/2005JD006566, URL http://doi.wiley.com/10.1029/2005JD006566, 2006.

Jones, A. E., Anderson, P. S., Begoin, M., Brough, N., Hutterli, M. A., Marshall, G. J., Richter, A., Roscoe, H. K., and Wolff, E. W.: BrO, blizzards, and drivers of polar tropospheric ozone depletion events, Atmospheric Chemistry and Physics, 9, 4639–4652, doi: 10.5194/acp-9-4639-2009, URL http://www.atmos-chem-phys.net/9/4639/2009/, 2009.

Jones, A. E., Anderson, P. S., Wolff, E. W., Roscoe, H. K., Marshall, G. J., Richter, A., Brough, N., and Colwell, S. R.: Vertical structure of Antarctic tropospheric ozone depletion events: characteristics and broader implications, Atmospheric Chemistry and Physics, 10, 7775–7794, doi: 10.5194/acp-10-7775-2010, URL http://www.atmos-chem-phys.net/10/7775/2010/, 2010.

Kahan, T. F., Wren, S. N., and Donaldson, D. J.: A pinch of salt is all it takes: chemistry at the frozen water surface., Accounts of chemical research, 47, 1587–94, doi: 10.1021/ar5000715, URL http://dx.doi.org/10.1021/ar5000715, 2014.

Kaleschke, L., Richter, A., Burrows, J., Afe, O., Heygster, G., Notholt, J., Rankin, A. M., Roscoe, H. K., Hollwedel, J., Wagner, T., and Jacobi, H. W.: Frost flowers on sea ice as a source of sea salt and their influence on tropospheric halogen chemistry, Geophysical Research Letters, 31, doi: 10.1029/2004GL020655, URL http://www.agu.org/pubs/crossref/2004/2004GL020655.shtml, 2004.

Kalnajs, L. E. and Avallone, L. M.: Frost flower influence on springtime boundary-layer ozone depletion events and atmospheric bromine levels, Geophysical Research Letters, 33, L10 810, doi: 10.1029/2006GL025809, URL http://www.agu.org/pubs/crossref/2006/2006GL025809.shtml, 2006.

Knepp, T. N., Bottenheim, J., Carlsen, M., Carlson, D., Donohoue, D., Friederich, G., Matrai, P. A., Netcheva, S., Perovich, D. K., Santini, R., Shepson, P. B., Simpson, W., Valentic, T., Williams, C., and Wyss, P. J.: Development of an autonomous sea ice tethered buoy for the study of ocean-atmosphere-sea ice-snow pack interactions: the O-buoy, Atmospheric Measurement Techniques, 3, 249–261, doi: 10.5194/amt-3-249-2010, URL http://www.atmos-meas-tech.net/3/249/2010/, 2010.

Koo, J.-H., Wang, Y., Kurosu, T. P., Chance, K., Rozanov, A., Richter, A., Oltmans, S. J., Thompson, A. M., Hair, J. W., Fenn, M. A., Weinheimer, A. J., Ryerson, T. B., Solberg, S., Huey, L. G., Liao, J., Dibb, J. E., Neuman, J. A., Nowak, J. B., Pierce, R. B., Natarajan, M., and Al-Saadi, J.: Characteristics of tropospheric ozone depletion events in the Arctic spring: analysis of the ARCTAS, ARCPAC, and ARCIONS measurements and satellite BrO observations, Atmospheric Chemistry and Physics, 12, 9909–9922, doi: 10.5194/acp-12-9909-2012, URL http://www.atmos-chem-phys.net/12/9909/2012/, 2012.

Krnavek, L., Simpson, W. R., Carlson, D., Dominé, F., Douglas, T. A., and Sturm, M.: The chemical composition of surface snow in the Arctic: Examining marine, terrestrial, and atmospheric influences, Atmospheric Environment, 50, 349 – 359, doi: http://dx.doi.org/10.1016/j.atmosenv.2011.11.033, URL http://www.sciencedirect.com/science/article/pii/S1352231011012192, 2012.

Kwok, R.: Near zero replenishment of the Arctic multiyear sea ice cover at the end of 2005 summer, Geophysical Research Letters, 34, L05 501, doi: 10.1029/2006GL028737, URL http://doi.wiley.com/10.1029/2006GL028737, 2007.

Legagneux, L., Cabanes, A., and Dominé, F.: Measurement of the specific surface area of 176 snow samples using methane adsorption at 77 K, Journal of Geophysical Research, 107, doi: 10.1029/2001JD001016, URL http://www.agu.org/pubs/crossref/2002/2001JD001016.shtml, 2002.

Lu, J. Y., Schroeder, W. H., Barrie, L. A., Steffen, A., Welch, H. E., Martin, K., Lockhart, L., Hunt, R. V., Boila, G., and Richter, A.: Magnification of atmospheric mercury deposition to polar regions in springtime: The link to tropospheric ozone depletion chemistry, Geophysical Research Letters, 28, 3219, doi: 10.1029/2000GL012603, URL http://www.agu.org/pubs/crossref/2001/2000GL012603.shtml, 2001.

Mahajan, A. S., Shaw, M., Oetjen, H., Hornsby, K. E., Carpenter, L. J., Kaleschke, L., Tian-Kunze, X., Lee, J. D., Moller, S. J., Edwards, P., Commane, R., Ingham, T., Heard, D. E., and Plane, J. M. C.: Evidence of reactive iodine chemistry in the Arctic boundary layer, Journal of Geophysical Research, 115, D20 303, doi: 10.1029/2009JD013665, URL http://doi.wiley.com/10.1029/2009JD013665, 2010.

Maslanik, J., Stroeve, J., Fowler, C., and Emery, W.: Distribution and trends in Arctic sea ice age through spring 2011, Geophysical Research Letters, 38, n/a–n/a, doi: 10.1029/2011GL047735, URL http://doi.wiley.com/10.1029/2011GL047735, 2011.

McConnell, J. C., Henderson, G. S., Barrie, L., Bottenheim, J., Niki, H., Langford, C. H., and Templeton, E. M. J.: Photochemical bromine production implicated in Arctic boundary-layer ozone depletion, Nature, 355, 150–152, doi: 10.1038/355150a0, URL http://dx.doi.org/10.1038/355150a0, 1992.

McElroy, C., McLinden, C., and McConnell, J.: Evidence for bromine monoxide in the free troposphere during the Arctic polar sunrise, Nature, 397, 2–5, URL http://www.nature.com/nature/journal/v397/n6717/abs/397338a0.html, 1999.

Moore, C. W., Obrist, D., Steffen, A., Staebler, R. M., Douglas, T. A., Richter, A., and Nghiem, S. V.: Convective forcing of mercury and ozone in the Arctic boundary layer induced by leads in sea ice., Nature, doi: 10.1038/nature12924, URL http://www.ncbi.nlm.nih.gov/pubmed/24429521, 2014.

Nghiem, S. V., Rigor, I. G., Perovich, D. K., Clemente-Colón, P., Weatherly, J. W., and Neumann, G.: Rapid reduction of Arctic perennial sea ice, Geophysical Research Letters, 34, L19 504, doi: 10.1029/2007GL031138, URL http://www.agu.org/pubs/crossref/2007/2007GL031138.shtml, 2007.

Nghiem, S. V., Rigor, I. G., Richter, A., Burrows, J. P., Shepson, P. B., Bottenheim, J., Barber, D. G., Steffen, A., Latonas, J., Wang, F., Stern, G., Clemente-Colón, P., Martin, S., Hall, D. K., Kaleschke, L., Tackett, P., Neumann, G., and Asplin, M. G.: Field and satellite observations of the formation and distribution of Arctic atmospheric bromine above a rejuvenated sea ice cover, Journal of Geophysical Research, 117, D00S05, doi: 10.1029/2011JD016268, URL http://www.agu.org/pubs/crossref/2012/2011JD016268.shtml, 2012.

Oldridge, N. W. and Abbatt, J. P. D.: Formation of gas-phase bromine from interaction of ozone with frozen and liquid NaCl/NaBr solutions: quantitative separation of surficial chemistry from bulk-phase reaction., The Journal of Physical Chemistry A, 115, 2590–8, doi: 10.1021/jp200074u, URL http://www.ncbi.nlm.nih.gov/pubmed/21388165, 2011.

Oltmans, S. J.: Surface ozone measurements in clean air, Journal of Geophysical Research, 86, 1174, doi: 10.1029/JC086iC02p01174, URL http://doi.wiley.com/10.1029/JC086iC02p01174, 1981.

Oltmans, S. J., Johnson, B. J., and Harris, J. M.: Springtime boundary layer ozone depletion at Barrow, Alaska: Meteorological influence, year-to-year variation, and long-term change, Journal of Geophysical Research, 117, D00R18, doi: 10.1029/2011JD016889, URL http://doi.wiley.com/10.1029/2011JD016889, 2012.

Perovich, D. K. and Richter-Menge, J. A.: Surface characteristics of lead ice, Journal of Geophysical Research, 99, 16 341–16 350, doi: 10.1029/94JC01194, 1994.

Piot, M. and von Glasow, R.: The potential importance of frost flowers, recycling on snow, and open leads for ozone depletion events, Atmospheric Chemistry and Physics, 8, 2437–2467, doi: 10.5194/acp-8-2437-2008, URL http://www.atmos-chem-phys.net/8/2437/2008/, 2008.

Platt, U. and Hönninger, G.: The role of halogen species in the troposphere., Chemosphere, 52, 325–38, doi: 10.1016/S0045-6535(03)00216-9, URL http://www.ncbi.nlm.nih.gov/pubmed/12738256, 2003.

Pöhler, D., Vogel, L., Friess, U., and Platt, U.: Observation of halogen species in the Amundsen Gulf, Arctic, by active long-path differential optical absorption spectroscopy., Proceedings of the National Academy of Sciences of the United States of America, 107, 6582–7, doi: 10.1073/pnas.0912231107, URL http://www.ncbi.nlm.nih.gov/pmc/articles/PMC2872394/, 2010.

Prados-Roman, C., Cuevas, C. A., Hay, T., Fernandez, R. P., Mahajan, A. S., Royer, S.-J., Galí, M., Simó, R., Dachs, J., Großmann, K., Kinnison, D. E., Lamarque, J.-F., and Saiz-Lopez, A.: Iodine oxide in the global marine boundary layer, Atmospheric Chemistry and Physics, 15, 583–593, doi: 10.5194/acp-15-583-2015, URL http://www.atmos-chem-phys.net/15/583/2015/acp-15-583-2015.html, 2015.

Pratt, K. A., Custard, K. D., Shepson, P. B., Douglas, T. A., Pöhler, D., General, S., Zielcke, J., Simpson, W. R., Platt, U., Tanner, D. J., Gregory Huey, L., Carlsen, M., and Stirm, B. H.: Photochemical production of molecular bromine in Arctic surface snowpacks, Nature Geoscience, doi: 10.1038/ngeo1779, URL http://www.nature.com/doifinder/10.1038/ngeo1779, 2013.

Rankin, A. M., Wolff, E. W., and Martin, S.: Frost flowers: Implications for tropospheric chemistry and ice core interpretation, Journal of Geophysical Research, 107, doi: 10.1029/2002JD002492, URL http://www.agu.org/pubs/crossref/2002/2002JD002492.shtml, 2002.

Read, K. A., Lewis, A. C., Salmon, R. A., Jones, A. E., and Bauguitte, S.: OH and halogen atom influence on the variability of non-methane hydrocarbons in the Antarctic Boundary Layer, Tellus B, 59, 22–38, doi: 10.1111/j.1600-0889.2006.00227.x, URL http://www.tellusb.net/index.php/tellusb/article/view/16966, 2007.

Richter, A., Wittrock, F., Eisinger, M., and Burrows, J. P.: GOME Observations of Tropospheric BrO in Northern Hemispheric Spring and Summer 1997, Geophys. Res. Lett., 25, 2683 – 2686, 1998.

Saiz-Lopez, A., Mahajan, A. S., Salmon, R. A., Bauguitte, S. J.-B., Jones, A. E., Roscoe, H. K., and Plane, J. M. C.: Boundary layer halogens in coastal Antarctica., Science (New York, N.Y.), 317, 348–351, doi: 10.1126/science.1141408, URL http://www.ncbi.nlm.nih.gov/pubmed/17641195, 2007.

Salawitch, R. J., Canty, T., Kurosu, T., Chance, K., Liang, Q., da Silva, A., Pawson, S., Nielsen, J. E., Rodriguez, J. M., Bhartia, P. K., Liu, X., Huey, L. G., Liao, J., Stickel, R. E., Tanner, D. J., Dibb, J. E., Simpson, W. R., Donohoue, D., Weinheimer, A., Flocke, F., Knapp, D., Montzka, D., Neuman, J. A., Nowak, J. B., Ryerson, T. B., Oltmans, S., Blake, D. R., Atlas, E. L., Kinnison, D. E., Tilmes, S., Pan, L. L., Hendrick, F., Van Roozendael, M., Kreher, K., Johnston, P. V., Gao, R. S., Johnson, B., Bui, T. P., Chen, G., Pierce, R. B., Crawford, J. H., and Jacob, D. J.: A new interpretation of total column BrO during Arctic spring, Geophysical Research Letters, 37, L21 805, doi: 10.1029/2010GL043798, URL http://doi.wiley.com/10.1029/2010GL043798, 2010.

Schroeder, W., Anlauf, K., Barrie, L., and Lu, J.: Arctic springtime depletion of mercury, Nature, pp. 16–17, doi: 10.1038/28530, URL http://www.nature.com/nature/journal/v394/n6691/abs/394331a0.html, 1998.

Selin, N. E., Jacob, D. J., Park, R. J., Yantosca, R. M., Strode, S., Jaeglé, L., and Jaffe, D.: Chemical cycling and deposition of atmospheric mercury: Global constraints from observations, Journal of Geophysical Research, 112, doi: 10.1029/2006JD007450, URL http://www.agu.org/pubs/crossref/2007/2006JD007450.shtml, 2007.

Sihler, H., Platt, U., Beirle, S., Marbach, T., Kühl, S., Dörner, S., Verschaeve, J., Frieß, U., Pöhler, D., Vogel, L., Sander, R., and Wagner, T.: Tropospheric BrO column densities in the Arctic derived from satellite: retrieval and comparison to ground-based measurements, Atmospheric Measurement Techniques, 5, 2779–2807, doi: 10.5194/amt-5-2779-2012, URL http://www.atmos-meas-tech.net/5/2779/2012/, 2012.

Simpson, W. R., Carlson, D., Hönninger, G., Douglas, T. A., Sturm, M., Perovich, D., and Platt, U.: First-year sea-ice contact predicts bromine monoxide (BrO) levels at Barrow, Alaska better than potential frost flower contact, Atmospheric Chemistry and Physics, 7, 621–627, doi: 10.5194/acp-7-621-2007, URL http://www.atmos-chem-phys.net/7/621/2007/, 2007a.

Simpson, W. R., von Glasow, R., Riedel, K., Anderson, P., Ariya, P., Bottenheim, J., Burrows, J., Carpenter, L. J., Frieß, U., Goodsite, M. E., Heard, D., Hutterli, M., Jacobi, H.-W., Kaleschke, L., Neff, B., Plane, J., Platt, U., Richter, A., Roscoe, H., Sander, R., Shepson, P., Sodeau, J., Steffen, A., Wagner, T., and Wolff, E.: Halogens and their role in polar boundary-layer ozone depletion, Atmospheric Chemistry and Physics, 7, 4375–4418, doi: 10.5194/acp-7-4375-2007, URL http://www.atmos-chem-phys.net/7/4375/2007/, 2007b.

Steffen, A., Douglas, T., Amyot, M., Ariya, P., Aspmo, K., Berg, T., Bottenheim, J., Brooks, S., Cobbett, F., Dastoor, A., Dommergue, A., Ebinghaus, R., Ferrari, C., Gardfeldt, K., Goodsite, M. E., Lean, D., Poulain, A. J., Scherz, C., Skov, H., Sommar, J., and Temme, C.: A synthesis of atmospheric mercury depletion event chemistry in the atmosphere and snow, Atmospheric Chemistry and Physics, 8, 1445–1482, doi: 10.5194/acp-8-1445-2008, URL http://www.atmos-chem-phys.net/8/1445/2008/, 2008.

Stephens, C. R., Shepson, P. B., Steffen, A., Bottenheim, J. W., Liao, J., Huey, L. G., Apel, E., Weinheimer, A., Hall, S. R., Cantrell, C., Sive, B. C., Knapp, D. J., Montzka, D. D., and Hornbrook, R. S.: The relative importance of chlorine and bromine radicals in the oxidation of atmospheric mercury at Barrow, Alaska, Journal of Geophysical Research, 117, D00R11, doi: 10.1029/2011JD016649, URL http://www.agu.org/pubs/crossref/2012/2011JD016649.shtml, 2012.

Strode, S. A., Jaeglé, L., Selin, N. E., Jacob, D. J., Park, R. J., Yantosca, R. M., Mason, R. P., and Slemr, F.: Air-sea exchange in the global mercury cycle, Global Biogeochemical Cycles, 21, GB1017, doi: 10.1029/2006GB002766, URL http://www.agu.org/pubs/crossref/2007/2006GB002766.shtml, 2007.

Stutz, J., Thomas, J. L., Hurlock, S. C., Schneider, M., von Glasow, R., Piot, M., Gorham, K., Burkhart, J. F., Ziemba, L., Dibb, J. E., and Lefer, B. L.: Longpath DOAS observations of surface BrO at Summit, Greenland, Atmospheric Chemistry and Physics, 11, 9899–9910, doi: 10.5194/acp-11-9899-2011, URL http://www.atmos-chem-phys.net/11/9899/2011/acp-11-9899-2011.html, 2011.

Style, R. W. and Worster, M. G.: Frost flower formation on sea ice and lake ice, Geophysical Research Letters, 36, doi: 10.1029/2009GL037304, URL http://www.agu.org/pubs/crossref/2009/2009GL037304.shtml, 2009.

Tackett, P. J., Cavender, A. E., Keil, A. D., Shepson, P. B., Bottenheim, J. W., Morin, S., Deary, J., Steffen, A., and Doerge, C.: A study of the vertical scale of halogen chemistry in the Arctic troposphere during Polar Sunrise at Barrow, Alaska, Journal of Geophysical Research, 112, D07 306, doi: 10.1029/2006JD007785, URL http://doi.wiley.com/10.1029/2006JD007785, 2007.

Theys, N., Van Roozendael, M., Errera, Q., Hendrick, F., Daerden, F., Chabrillat, S., Dorf, M., Pfeilsticker, K., Rozanov, A., Lotz, W., Burrows, J. P., Lambert, J.-C., Goutail, F., Roscoe, H. K., and De Mazière, M.: A global stratospheric bromine monoxide climatology based on the BASCOE chemical transport model, Atmospheric Chemistry and Physics, 9, 831–848, doi: 10.5194/acp-9-831-2009, URL http://www.atmos-chem-phys.net/9/831/2009/, 2009.

Theys, N., Van Roozendael, M., Hendrick, F., Yang, X., De Smedt, I., Richter, A., Begoin, M., Errera, Q., Johnston, P. V., Kreher, K., and De Mazière, M.: Global observations of tropospheric BrO columns using GOME-2 satellite data, Atmospheric Chemistry and Physics, 11, 1791–1811, doi: 10.5194/acp-11-1791-2011, URL http://www.atmos-chem-phys.net/11/1791/2011/, 2011.

Thompson, A. M.: The Oxidizing Capacity of the Earth's Atmosphere: Probable Past and Future Changes, Science, 256, 1157–1165, doi: 10.1126/science.256.5060.1157, URL http://www.sciencemag.org/content/256/5060/1157.short, 1992.

Tian, W., Egeland, G. M., Sobol, I., and Chan, H. M.: Mercury hair concentrations and dietary exposure among Inuit preschool children in Nunavut, Canada., Environment international, 37, 42–8, doi: 10.1016/j.envint.2010.05.017, URL http://www.ncbi.nlm.nih.gov/pubmed/20673686, 2011.

Wagner, T. and Platt, U.: Satellite mapping of enhanced BrO concentrations in the troposphere, Nature, 395, 486 – 490, 1998.

Wagner, T., Leue, C., Wenig, M., Pfeilsticker, K., and Platt, U.: Spatial and temporal distribution of enhanced boundary layer BrO concentrations measured by the GOME instrument aboard ERS-2, Journal of Geophysical Research, 106, 24 225, doi: 10.1029/2000JD000201, URL http://doi.wiley.com/10.1029/2000JD000201, 2001.

Wagner, T., Ibrahim, O., Sinreich, R., Frieß, U., von Glasow, R., and Platt, U.: Enhanced tropospheric BrO over Antarctic sea ice in mid winter observed by MAX-DOAS on board the research vessel Polarstern, Atmospheric Chemistry and Physics, 7, 3129–3142, doi: 10.5194/acp-7-3129-2007, URL http://www.atmos-chem-phys.net/7/3129/2007/acp-7-3129-2007.html, 2007.

Wania, F. and Mackay, D.: Tracking the distribution of persistent organic pollutants, Environmental science & technology, 30, 390A–6A, doi: 10.1021/es962399q, URL http://dx.doi.org/10.1021/es962399q, 1996.

Wren, S. N. and Donaldson, D. J.: How does deposition of gas phase species affect pH at frozen salty interfaces?, Atmospheric Chemistry and Physics, 12, 10 065–10 073, doi: 10.5194/acp-12-10065-2012, URL http://www.atmos-chem-phys.net/12/10065/2012/, 2012.

Wren, S. N., Kahan, T. F., Jumaa, K. B., and Donaldson, D. J.: Spectroscopic studies of the heterogeneous reaction between $O_{3(g)}$ and halides at the surface of frozen salt solutions, Journal of Geophysical Research, 115, 1–8, doi: 10.1029/2010JD013929, URL http://www.agu.org/pubs/crossref/2010/2010JD013929.shtml, 2010.

Wren, S. N., Donaldson, D. J., and Abbatt, J. P. D.: Photochemical chlorine and bromine activation from artificial saline snow, Atmospheric Chemistry and Physics, 13, 9789–9800, doi: 10.5194/acp-13-9789-2013, URL http://www.atmos-chem-phys.net/13/9789/2013/, 2013.

Yang, X., Pyle, J. A., and Cox, R. A.: Sea salt aerosol production and bromine release: Role of snow on sea ice, Geophysical Research Letters, 35, L16 815, doi: 10.1029/2008GL034536, URL http://doi.wiley.com/10.1029/2008GL034536, 2008.

Yang, X., Pyle, J. A., Cox, R. A., Theys, N., and Van Roozendael, M.: Snow-sourced bromine and its implications for polar tropospheric ozone, Atmospheric Chemistry and Physics, 10, 7763–7773, doi: 10.5194/acp-10-7763-2010, URL http://www.atmos-chem-phys.net/10/7763/2010/, 2010.

Chapter 2

Observations of Brine on Ice Using X-ray Absorption Edge Computed Microtomography[1]

2.1 Abstract

On sea ice, one of the mechanisms for enhancing the effective saline surface area available for heterogeneous halogen activation chemistry is the wicking of brine on vapor deposited ice or snow. In order to determine the potential effects of ice contaminated by the wicking of brine on boundary layer chemistry, it is essential to understand the motion of brine on these surfaces, as well as the resulting surface coverage and overall distribution of brine within the ice. We used X-ray absorption edge computed microtomography (CMT) to explore the effective surface coverage of laboratory-grown vapor deposited ice samples via brine wicking at environmentally relevant temperatures by generating a three dimensional map of the brine in relation to the ice. These data show that the wicking process does not result in a homogeneous distribution of brine, with the majority of the observed brine located near the base of the sample, and decreasing salinity toward the top of the sample. 2-D slices through the sample show the horizontal distribution of brine is also heterogeneous with brine being in concentrated regions, rather than evenly spread over the ice surface. These findings show that knowledge of the bulk composition of ice/brine systems is insufficient to model the influence of ice/brine systems formed from wicking of brine from sea ice surfaces on atmospheric chemistry.

2.2 Introduction

Because of the ubiquitous nature of ice, chemistry taking place on ice surfaces has a substantial effect on the environment, particularly in the polar regions through processes such as halogen activation (Abbatt et al., 2012). As sea ice forms, thermodynamics drives impurities present in seawater to separate from the pure bulk ice leading to a concentrated layer of salt solution (brine) on the ice surface (Perovich and Richter-Menge, 1994). In the polar spring, a process known as the "bromine explosion" (Wennberg, 1999) causes bromine radicals to be released into the Arctic atmospheric boundary layer from bromide ions present in brine on sea ice surfaces. Once in the atmosphere, these bromine radicals cause events such as episodic boundary layer ozone depletion (Barrie et al., 1988; Simpson et al., 2007b) and mercury deposition (Schroeder et al., 1998; Steffen et al., 2008).

Multiple studies show that time spent in large geographic regions that are predominantly first year sea ice (FYI) is correlated with halogen activation and related processes (e.g. Wagner et al., 2001; Frieß, 2004; Simpson et al., 2007a). However, given the variability in ice surfaces found in

[1] P. K. Peterson, W. R. Simpson, M. L. Rivers, and T. P. Trainor, Observations of Brine on Ice Using X-ray Absorption Edge Computed Microtomography. Prepared for submission to The Cryosphere

FYI regions, how specific ice features found in FYI regions facilitate halogen activation remains an open question. First year ice areas have a variety of features that have been implicated in halogen activation processes including saline snow, which has been shown to have a high bulk salinity (Dominé and Shepson, 2002; Simpson et al., 2005; Krnavek et al., 2012), open leads which lead to convective mixing and potentially more bromine release (McElroy et al., 1999; Nghiem et al., 2012; Moore et al., 2014), and the presence of frost flowers, a vapor-deposited ice form shown to have high salinity (Kalnajs and Avallone, 2006; Alvarez-Aviles et al., 2008).

Frost flowers form on sublimating ice surfaces at low air temperatures, a situation that commonly occurs in sea ice areas (Style and Worster, 2009). Rankin et al. (2002) implicated frost flowers in boundary layer halogen chemistry because of their high bulk salinity and presumed high surface area. Later work by Dominé et al. (2005) showed that the surface area of frost flowers was comparable to that of snow, suggesting that snow, which is much more abundant in the Arctic, is a more important source of active halogens. Kaleschke et al. (2004) showed a relationship between areas of potential frost flowers and BrO observed using satellite in Antarctica, however this relationship has not been observed in the Arctic. Modeling work by Piot and von Glasow (2008) showed that the ability of frost flowers to explain observed levels of boundary layer ozone depletion requires recycling of halogens in the snowpack in addition to frost flowers. The high salinity of frost flowers is due to a process referred to as "wicking" where brine moves from the brine layer on freshly formed sea ice onto other ice surfaces via capillary action. This wicking process leads to brine concentrations much higher than that of seawater (Perovich and Richter-Menge, 1994; Alvarez-Aviles et al., 2008). This wicking of brine can also be a source of halogens for the snowpack overlying sea ice (Dominé et al., 2004; Krnavek et al., 2012).

A combination of laboratory and field studies have studied the physical and chemical properties of saline ice surfaces and ice brine systems, including bulk composition (e.g. Perovich and Richter-Menge, 1994; Kalnajs and Avallone, 2006; Alvarez-Aviles et al., 2008; Roscoe et al., 2011; Krnavek et al., 2012), specific surface area (e.g. Legagneux et al., 2002; Dominé et al., 2005; Roscoe et al., 2011), and surface chemical properties (e.g. Wren et al., 2010; Oldridge and Abbatt, 2011; Wren and Donaldson, 2012). However, knowledge of these properties alone does not answer questions about the availability of brine for reaction with the atmosphere. In particular, bulk composition measurements require melting of the ice sample prior to analysis, which destroys any information about the microstructure and surface composition of these systems. Study of the ice surfaces on which heterogeneous chemical reactions take place can provide important information on the mechanism by which bromide in the brine becomes available to the atmosphere, as well as how much brine is available to react (Bartels-Rausch et al., 2014).

Modeling the impacts of brine coated ice on the chemistry requires one to make assumptions about the distribution of brine in relation to the ice. A common assumption made in modeling studies is that bromide and chloride are excluded from the ice on freezing and form a concentrated layer at the ice surface (e.g. Thomas et al., 2011). The thickness of this layer is estimated by multiplying the brine volume fraction by the ratio of volume to surface area (Kuo et al., 2011). While this approach is reasonable given current knowledge of the microstructure of ice brine systems, there are potential problems with this approach. While thermodynamics dictates the exclusion of brine from the overall ice matrix on freezing, the phase diagram of the ice brine system does not provide any information on where that brine is excluded to. Some possibilities include brine being excluded to the air ice interface, isolated pockets within the sample, or grain boundaries (Dominé et al., 2013). Multiple studies have shown that ionic impurities are at the air ice interface (e.g Oldridge and Abbatt, 2011; Kahan et al., 2014); however, ascertaining the relationship between bulk salinity and surface brine concentrations requires knowledge of the three dimensional micro-structure of the ice brine system. This knowledge is also required to model the role of ice brine systems in the chemistry of the atmosphere effectively (Piot and von Glasow, 2008).

This paper details the investigation of brine wicking and the resulting brine distributions using X-ray absorption edge computed micro-tomography (CMT). Previous studies used polychromatic X-ray CMT to observe the thermal evolution of brine in large single crystals of sea ice (e.g. Golden et al., 2007; Pringle et al., 2009). Use of a monochromatic synchrotron rather than a polychromatic laboratory based X-ray source allows us to calculate the density of ionic impurities, in addition to the location of brine in the sample using absorption edge CMT (Sutton et al., 2002). We used this technique to quantify three dimensional brine distributions resulting from wicking of brine up the ice crystal from a saline surface. Additionally, we used 2-D X-ray movies to observe the vertical motion of brine onto clean ice in real time.

2.3 Methods

2.3.1 Sample Preparation

We grew samples by freezing 0.5 molar CsCl solutions, which approximate the ionic content of sea water, using techniques detailed in Martin et al. (1995, 1996). The CsCl has a similar phase diagram to NaCl (Monnin and Dubois, 1999), the primary component of sea salt, but has a higher energy cesium K absorption edge (35.984 KeV) than sodium allowing for greater contrast with ice on the collected tomograms. Figure 2.1 shows a photographic image of the resulting vapor deposited ice

samples. The image shows the samples are dendritic crystals exhibiting similar morphology to natural frost flowers seen in Dominé et al. (2005).

2.3.2 Sample Composition

The thermodynamic properties of low temperature CsCl are well studied (Dubois et al., 1993; Monnin and Dubois, 1999). At the eutectic temperature of $-23.7\,^{\circ}\mathrm{C}$, the system consists of ice and solid CsCl (Dubois et al., 1993). The concentration of CsCl is 56.87% by mass or 7.67 M (Monnin and Dubois, 1999).

2.3.3 Cold Stage Design

Figure 2.2 shows a diagram of the cold stage used to image the sample over environmentally relevant temperatures in a room that is room temperature. The stage needs to allow for imaging while maintaining the temperature of the sample and allowing for unconstrained rotation of the sample, which is required for synchrotron based CMT. Inhibiting the samples rotation causes image artifacts due to the sample rotation axis not being perfectly vertical. The cold stage's rotating base consists of a teflon baseplate with an aluminum post in the center where we place the sample prior to imaging. This post is in thermal contact with two stacked thermoelectric coolers (TEC), which move heat away from the sample. A liquid (50/50 ethylene glycol and H_2O) cooled copper heatsink cools the TECs to increase the ability of the TECs to remove heat from the sample chamber. These heatsinks are attached to a circulating chiller using coiled tubing that allows the baseplate to rotate freely. We then enclose the sample with an eighth-inch thick rectangular copper chamber cooled in the same manner as the sample base and insulated with one inch foam. The cap has two one inch diameter double-pane Kapton windows to allow for imaging. Because the ability to obtain tomographic data with minimal artifacts is contingent on the ability to rotate the sample without constraint, the cap remains stationary throughout the imaging process while the baseplate rotates. We also connected the cap to a helium purge line to prevent additional vapor deposition on the ice crystal during the imaging process.

We controlled the voltage of the TEC's using a DC power supply with integrated temperature controllers. The temperature controllers use type K thermocouples placed between the TEC and the metal components of the cold stage to regulate the TECs. This setup allows for stable TEC cold plate set points down to $-40\,^{\circ}\mathrm{C}$. Given the volume of the cold sample chamber (154 cm^3), it is likely that the TEC set points are not representative of the sample temperature. To obtain a more representative reading, we placed an additional type K thermocouple in the sample chamber to read the interior air temperature. Taking this interior measurement to be the best approximation

of sample temperature, we are able to image brine distributions at temperatures as low as $-24\,^{\circ}\mathrm{C}$, which is below the eutectic temperature of CsCl.

We prepared samples for imaging by attaching the sample to the baseplate in a chest freezer using vacuum grease with tools kept in the chest freezer to minimize heat transfer to the sample. We then removed the thermo-electrically cooled baseplate from the chest freezer and placed it beneath the already cooled copper cap.

2.3.4 X-ray Absorption Edge CMT

X-ray absorption edge CMT yields a three dimensional map of the attenuation of the X-ray beam (tomogram) through reconstruction of two dimensional images. We generated 2-D images by placing the sample in the path of a monochromatic X-ray beam and measuring the transmitted X-ray intensity. We measured the intensity by capturing an image of the transmitted X-ray beam using a single crystal YAG scintillator to convert the X-rays to visible light and taking a picture of the scintillator with a CCD camera. The field of view was 8.9mm wide by 6mm tall with a pixel resolution of 12.84 microns. We then rotated the sample 180 degrees in 0.25 degree steps to generate the 720 2-D images that we then reconstructed to obtain a 3-D representation of the attenuation in each voxel (3-D equivalent of a pixel). We obtained these data at GeoSoilEnviroCARS (Sector 13), Advanced Photon Source (APS), Argonne National Laboratory. Sutton et al. (2002) provides more detailed information on the data collection setup.

To allow for quantitative study of the brine via absorption edge methods, we collected two tomograms bracketing the Cesium K absorption edge of 35.984 KeV (Obtained from NIST (Hubbell and Seltzer, 2004)). We took the above edge data sets at an energy of 36.085 keV, and the below edge data sets at an energy of 35.885 keV. The images presented in this work are all taken below the CsCl eutectic temperature of $-23.7\,^{\circ}\mathrm{C}$ (Monnin and Dubois, 1999).

2.3.5 Reconstruction and Segmentation

We initially reconstructed each tomogram from the 2-D images using software developed by Rivers and Gualda (2009). Figure 2.3 shows a 2-D slice through the reconstructed volume at the different X-ray energies used in this study. The top panel shows the above edge image, while the bottom panel shows the below edge image. This figure illustrates the edge contrast in the two sets of images, with the brighter spots on the top panel indicating the location of the brine pockets in relation to the overall ice structure. To analyze these data further, we classified each voxel in the tomogram by segmenting the tomogram into ice, brine, and background classes.

The first step of the segmentation procedure requires the calculation of the cesium distribution in the tomogram. We used the attenuation difference between above and below absorption edge tomograms to calculate the average brine concentration in each voxel. The attenuation of each voxel is a dimensionless quantity dependent on the voxel size, density, and mass attenuation coefficients of the elements in each voxel. Figure 2.4 shows that the difference in attenuation due to chloride and ice between the two tomograms taken at an energy difference of 0.2 keV is negligible, while the attenuation due to Cs is increased. The left panel of Fig. 2.5 shows histograms of the voxel attenuation in both the above (blue line) and below (red line) edge tomograms. The histogram of the above edge tomogram shows a heavy tail in the positive direction that can be attributed to Cs. Thus, the difference of the above and below edge tomograms is solely dependent on the concentration of Cs in each voxel, allowing us to generate a three-dimensional map of the average cesium concentration in the sample. The right panel of Fig. 2.5 shows the histogram of the calculated average brine concentrations for each voxel. This histogram is a zero-centered Gaussian distribution with a heavy tail in the positive direction. From this histogram, we calculated a 2 σ detection limit for this technique of 0.12 M, which we indicate using a red line on the right panel of Fig. 2.5. We classify voxels containing brine above the detection limit as brine voxels.

The second step requires the separation of the sample ice from the air background, which we do by filtering the below edge tomogram with a 3-D median filter (Pringle et al., 2009). We then use the brine density map generated in the first step to calculate the attenuation in the below edge tomogram due to cesium and chloride, which are present in equimolar amounts due to charge balance, and subtract this attenuation from each voxel. Figure 2.6 shows the resulting histogram of the attenuation not due to CsCl derived from the below-edge image. While the resulting histogram is asymmetric, there is no unambiguous separation of background and ice voxels. Thus, we require a physically motivated threshold to separate the ice from the air background. To obtain this threshold we calculated the theoretical attenuation due to a full ice voxel using the density of ice and the attenuation of water at the below edge X-ray energy. Figure 2.6 indicates this theoretical value using a black vertical line. We then set the threshold for segmentation by taking half of this value to approximate the attenuation of a half-filled voxel. We show this threshold value using a red vertical line on Fig. 2.6. While this selection theoretically eliminates voxels that are less then half full, the width of the exponential noise or observed attenuation values causes overlap of ice and air voxels, as the red line on Fig. 2.6 illustrates. We performed an additional median filtering after setting voxel attenuations below the threshold equal to zero to reduce noise in the thresholded image. Figure 2.7 shows the results of this segmentation procedure. Sample ice voxels are shown in teal, while voxels containing brine are shown in red. Note there is still some remaining noise from the segmentation procedure due to the low distinction between ice and

background. We used this thresholded image to index the reconstructed tomograms for analysis of the Cs and ice distributions.

2.4 Results

2.4.1 3-D Rendering

Figure 2.8 shows a three dimensional rendering of an ice sample made using the 3D viewing plugin for ImageJ (Abramoff et al., 2004). There are regions of discontinuous ice in the image that may be attributed to the high energy of the X-Rays used for imaging or the rendering procedure used by ImageJ, which bases voxel brightness on the voxel attenuation. This rendering uses increasing brightness to show the location of Cs in relation to the ice. The brighter regions of Fig. 2.8 show that the brine is not evenly distributed over the sample surface and has instead preferentially wicked up certain regions of the sample covering about a third of the sample. This uneven coverage is also seen in the 2-D slices shown in Fig. 2.7, which indicate that only the right island contains large amounts of Cs.

2.4.2 Calculation of Average Brine Distribution

Figure 2.9 shows a histogram comparing the relative brine content of both ice and brine voxels. The left panel of Fig. 2.9 shows that about 60% of the non-air voxels do not contain brine above our detection limit of 0.12 M, which is indicated with a red line. The right panel shows the distribution of voxels with average brine concentrations above the detection limit. This plot shows that it is rare for voxels to have concentrations of brine above 1 M. For reference, the theoretical concentration of CsCl at the eutectic temperature is 7.67 M (Monnin and Dubois, 1999). Examining the two dimensional slices shown in Fig. 2.7 shows that there are brine channels that potentially traverse the interior of the sample, and the brine voxels seem to be clustered in concentrated pockets within the sample, rather than at the sample surface. Of the voxels that do contain brine, most of them contain less than 0.5 M average brine concentrations. However, it is likely that the brine is at a uniform concentration, thus the reasonable interpretation of variable average concentrations of brine in a voxel is that the voxel is only partially filled with brine. Even in designated brine voxels, these voxels contain some ice. Figure 2.7 shows brine pockets on the top right ice form that appear to traverse the width of the sample; however, these channels may be blocked by ice and there may be brine inclusions in these regions, rather than all of this brine being accessible to the atmosphere.

2.4.3 Vertical Distribution of Brine

Figure 2.10, left panel, shows the vertical distribution of brine in the sample (red), as well as the distribution of ice (blue). We smoothed each distribution with a moving average over 5 (12.84 μm thick) slices. The ice distribution is slightly uneven, with more ice being present at the base of the sample, which is consistent with the rendering shown in Fig. 2.8. While the field of view is 6 mm high, we truncated the plot at the top of the sample, which is 4.04 mm tall. The distribution shows that brine in quantities above the detection limit does not make it all the way up the sample and the majority of the brine is located in the lower third of the sample. While the majority of the ice is at the base of the sample as well, the fraction of total ice at the base is smaller than the fraction of total brine, indicating that the vertical distribution of brine is different than the vertical distribution of ice. Figure 2.10, right panel, shows the ratio of brine to ice as a function of height. Aside from the top of the sample, which has very little ice and brine, and is more influenced by noise, this plot shows the ratio of brine to ice also decreases with height, mirroring the trends in overall salinity.

2.4.4 2-D X-ray Movies of Brine Motion

We can observe the response of brine to temperature change in real time by taking 2-D X-ray movies. We do this by placing a pure ice crystal onto frozen CsCl and warming the sample from -22°C to -15°C. Concurrently, we generate a 100 frame movie by fixing the orientation of the sample relative to the X-Ray beam and taking an image of the scintillator every five seconds. Figure 2.11 shows five frames taken during the warming. Given the low attenuation of ice at these X-Ray energies, brine is primarily visible. In the top left panel, there are two regions labeled A and B, that show the evolution of the brine in response to increasing temperature. As seen in each subsequent frame the brine moves further up the sample as the temperature increases. In real time the movies show that brine wicks up certain regions preferentially as the temperature increases rather than uniformly coating the sample surface. This uneven distribution of brine is also seen in the 3-D rendering of a frost flower sample in Figure 2.8. We also observed that the wicking is a pulsed rather than a continuous process with long periods of time between brine motion.

2.5 Discussion

2.5.1 Comparison to Environmental Vapor Deposited Ice

Figure 2.8 shows the sample exhibits the 120 degree angles one would expect for hexagonal ice crystals and the overall structure is similar to that seen in photomicrographs of wet frost flowers (Dominé et al., 2005). The sample width and height are on the order of mm, while the

sample thickness ranges from approximately 300 microns at the base to less than 100 microns toward the tips of the sample. This aspect ratio is what one would expect from vapor-deposited ice, reinforcing the idea that the laboratory grown samples studied in this work do not exhibit noticeably different morphology than naturally occurring frost flowers. Alvarez-Aviles et al. (2008) suggested two potential configurations for the ice/brine systems resulting from brine wicking up ice growing via vapor deposition. The first was that the ice skeleton grew and then brine wicked up that skeleton. The second was that ice also grew around pockets of brine, creating brine inclusions and brine channels. These data support both mechanisms, as Fig. 2.3 shows brine in channels through the sample as well as pockets of brine on the sample surface. Figure 2.10 shows the vertical distribution of brine, which indicates more brine toward the base and decreasing brine higher up the sample indicates that brine is wicking up the sample, and the size of the brine regions is decreasing. The drop in surface brine in the upper regions of the sample is likely a combination of two factors. One, the brine layer could be thinning as it moves up the sample; and two, Fig. 2.8 shows the ice volume decreases toward the top of the sample.

2.5.2 Variability of Brine Layer Thickness

The thermodynamics of the system imply that the brine in the sample should have a uniform concentration of 7.67 M at the eutectic temperature, thus the variability of concentrations observed in sample brine voxels is likely indicative of variations in the thickness of the brine layer on the surface and partially filled voxels. Note that the right panel of Fig. 2.5 shows that the majority of voxels have brine concentrations less than half the eutectic concentration and no voxels are above the eutectic concentration. Additionally, Fig. 2.3 shows thickness of observed brine layer on the sample ranges from sub-voxel thicknesses to hundreds of microns, which is in contrast with previous models that assume a uniform layer thickness based on the ratio of surface area to volume to model the impacts of ice brine systems on the chemistry of the atmosphere (e.g. Kuo et al., 2011). The observed variable thickness of the brine layer is not necessarily surprising, given that the formation of a brine coated surface is not energetically favorable when compared to the formation of distinct brine regions (Dominé et al., 2013).

Given that chemical reactions happen on sub-nanometer length scales rather than 12 microns, which is the resolution of these data, it is necessary to consider to what degree our resolution limitations impact our ability to draw conclusions about surface coverage with this technique. Figure 2.9 shows the majority of the brine voxels are partially filled, which is likely a common occurrence on the sample surface. It is clear we can detect layers that are thinner than 12 microns; However, we are unable to detect it at sufficiently low concentrations to rule out the presence of tens of nanometer scale layers where heterogeneous chemistry can occur, even on surface voxels

that appear free of brine. It is also important to note that our segmentation procedure does not allow for unambiguous detection of the sample surface, as some surface voxels are likely less than half full of ice, and considered background in our thresholded tomogram. Additionally, given the noise in these data, it is likely that some voxels more than half full of ice also appear empty.

A potential complication in evaluating the reactivity of ice surfaces is the presence of the quasi-liquid layer (QLL) (Dash and Wettlaufer, 2006). The QLL is a disordered layer of varying thickness at the surface of the ice crystal, because this layer is still part of the ice matrix, it is not a separate liquid phase and has different properties than liquid water (Dominé et al., 2013). The existence of a QLL and the lack of understanding of the thermodynamics of brine interacting with the QLL is a potential issue when modeling the impact of ice/brine systems on the atmosphere (Piot and von Glasow, 2008). However, recent work by Kahan et al. (2014) has shown that the chemical behavior of ice/brine surfaces is well explained by assuming the surface is a normal liquid phase, rather than a QLL. Additionally, given the complex nature of the brine distribution shown in this work, it is likely that accounting for the heterogeneous nature of the brine coated surface is more important than accounting for the QLL when modeling the impact of ice/brine systems on the atmosphere.

Despite these issues, the fact that this system exhibits similar morphology to frost flowers grown via vapor deposition on frozen solutions with similar ionic content to sea water shows that the study of these ice brine systems allows one to draw some conclusions about the nature of brine on environmental ices. Figure 2.10 shows uneven wicking of brine up the ice skeleton with most of the brine located toward the bottom of the sample, and steadily decreasing salinity as brine moves up the sample. This agrees with previous observations of the regional dependence of frost flower salinity (e.g. Perovich and Richter-Menge, 1994; Alvarez-Aviles et al., 2008). Figure 2.3 also indicates the presence of segregated brine regions rather than an evenly coated ice surface. Figure 2.11 shows that the brine distribution and surface coverage vary with time, with brine migrating higher up the ice skeleton over time, increasing the surface coverage. When observed in real time through 2-D X-ray movies, the brine moves in distinct pulses, rapidly transitioning between different brine distributions, then remaining stationary for comparatively long periods of time.

2.6 Conclusions

We used absorption microtomography to quantitatively image the location and concentration of brine in relation to ice on vapor deposited ice. The results show that the samples exhibit distinct regions of brine and ice. These images show that the brine is not uniformly distributed through the sample, and the degree of surface coverage varies with time. Most of the sample does not contain detectable brine, and when examining the voxels that do contain brine, it is clear that the

distribution of brine is heterogeneous, with the sample showing decreased salinity away from the base of the sample. The lack of a uniform brine coating on the sample surface shows that the thickness of the brine layer on the sample surface is variable ranging from tens of microns to sub-micron thicknesses. Examination of brine motion in real time through the use of 2-D X-ray movies shows enhanced brine motion and surface coverage with increasing temperatures.

Given the heterogeneous nature of the brine distribution and the presence of distinct brine regions, it is clear that knowing bulk concentration alone is insufficient to determine the effects of this ice brine system on the chemistry of the atmosphere. It is evident that rather than relying solely on information about bulk composition of the system, the separation of brine from ice during the freezing process and the resulting effects on brine distribution and ice microstructure need to be taken into account in atmospheric chemical models to provide an accurate assessment of the effect of ice interface chemistry on the atmosphere.

2.7 Acknowledgements

This work was performed at GeoSoilEnviroCARS (Sector 13), Advanced Photon Source (APS), Argonne National Laboratory. GeoSoilEnviroCARS is supported by the National Science Foundation - Earth Sciences (EAR-1128799) and Department of Energy- GeoSciences (DE-FG02-94ER14466). This research used resources of the Advanced Photon Source, a U.S. Department of Energy (DOE) Office of Science User Facility operated for the DOE Office of Science by Argonne National Laboratory under Contract No. DE-AC02-06CH11357.

2.8 References

Abbatt, J. P. D., Thomas, J. L., Abrahamsson, K., Boxe, C., Granfors, A., Jones, A. E., King, M. D., Saiz-Lopez, A., Shepson, P. B., Sodeau, J., Toohey, D. W., Toubin, C., von Glasow, R., Wren, S. N., and Yang, X.: Halogen activation via interactions with environmental ice and snow in the polar lower troposphere and other regions, Atmospheric Chemistry and Physics, 12, 6237–6271, doi: 10.5194/acp-12-6237-2012, URL http://www.atmos-chem-phys.net/12/6237/2012/, 2012.

Abramoff, M., Magelhaes, P., and Ram, S.: Image Processing with ImageJ, Biophotonics International, 11, 36–42, URL http://rsb.info.nih.gov/ij/, 2004.

Alvarez-Aviles, L., Simpson, W. R., Douglas, T. A., Sturm, M., Perovich, D., and Dominé, F.: Frost flower chemical composition during growth and its implications for aerosol production and bromine activation, Journal of Geophysical Research, 113, 21 304, doi: 10.1029/2008JD010277, URL http://www.agu.org/pubs/crossref/2008/2008JD010277.shtml, 2008.

Barrie, L. A., Bottenheim, J. W., Schnell, R. C., Crutzen, P. J., and Rasmussen, R. A.: Ozone destruction and photochemical reactions at polar sunrise in the lower Arctic atmosphere, Nature, 334, 138–141, doi: 10.1038/334138a0, URL http://www.nature.com/doifinder/10.1038/334138a0, 1988.

Bartels-Rausch, T., Jacobi, H.-W., Kahan, T. F., Thomas, J. L., Thomson, E. S., Abbatt, J. P. D., Ammann, M., Blackford, J. R., Bluhm, H., Boxe, C., Dominé, F., Frey, M. M., Gladich, I., Guzmán, M. I., Heger, D., Huthwelker, T., Klán, P., Kuhs, W. F., Kuo, M. H., Maus, S., Moussa, S. G., McNeill, V. F., Newberg, J. T., Pettersson, J. B. C., Roeselová, M., and Sodeau, J. R.: A review of air-ice chemical and physical interactions (AICI): liquids, quasi-liquids, and solids in snow, Atmospheric Chemistry and Physics, 14, 1587–1633, doi: 10.5194/acp-14-1587-2014, URL http://www.atmos-chem-phys.net/14/1587/2014/acp-14-1587-2014.html, 2014.

Dash, J. G. and Wettlaufer, J. S.: The physics of premelted ice and its geophysical consequences, Reviews of Modern Physics, 78, 695–741, doi: 10.1103/RevModPhys.78.695, URL http://link.aps.org/doi/10.1103/RevModPhys.78.695, 2006.

Dominé, F. and Shepson, P. B.: Air-snow interactions and atmospheric chemistry., Science (New York, N.Y.), 297, 1506–10, doi: 10.1126/science.1074610, URL http://www.ncbi.nlm.nih.gov/pubmed/12202818, 2002.

Dominé, F., Sparapani, R., Ianniello, A., and Beine, H. J.: The origin of sea salt in snow on Arctic sea ice and in coastal regions, Atmospheric Chemistry and Physics, 4, 2259–2271, doi: 10.5194/acp-4-2259-2004, URL http://www.atmos-chem-phys.net/4/2259/2004/, 2004.

Dominé, F., Taillandier, A. S., Simpson, W. R., and Severin, K.: Specific surface area, density and microstructure of frost flowers, Geophysical Research Letters, 32, 2–5, doi: 10.1029/2005GL023245, URL http://www.agu.org/pubs/crossref/2005/2005GL023245.shtml, 2005.

Dominé, F., Bock, J., Voisin, D., and Donaldson, D. J.: Can we model snow photochemistry? Problems with the current approaches., The journal of physical chemistry. A, 117, 4733–49, doi: 10.1021/jp3123314, URL http://www.ncbi.nlm.nih.gov/pubmed/23597185, 2013.

Dubois, M., Royer, J., Weisbrod, A., and Shutka, A.: Reconstruction of low-temperature binary phase diagrams using a constrained least squares method: Application to the H2O-CsCl system, European Journal of Mineralogy, 5, 1145–1152, URL http://cat.inist.fr/?aModele=afficheN\&cpsidt=4022663, 1993.

Frieß, U.: Dynamics and chemistry of tropospheric bromine explosion events in the Antarctic coastal region, Journal of Geophysical Research, 109, D06 305, doi: 10.1029/2003JD004133, URL http://doi.wiley.com/10.1029/2003JD004133, 2004.

Golden, K. M., Eicken, H., Heaton, A. L., Miner, J., Pringle, D. J., and Zhu, J.: Thermal evolution of permeability and microstructure in sea ice, Geophysical Research Letters, 34, doi: 10.1029/2007GL030447, URL http://www.agu.org/pubs/crossref/2007/2007GL030447.shtml, 2007.

Hubbell, J. H. and Seltzer, S. M.: Tables of X-Ray Mass Attenuation Coefficients and Mass Energy-Absorption Coefficients from 1 keV to 20 MeV for Elements Z = 1 to 92 and 48 Additional Substances of Dosimetric Interest, URL http://www.nist.gov/pml/data/xraycoef/index.cfm, 2004.

Kahan, T. F., Wren, S. N., and Donaldson, D. J.: A pinch of salt is all it takes: chemistry at the frozen water surface., Accounts of chemical research, 47, 1587–94, doi: 10.1021/ar5000715, URL http://dx.doi.org/10.1021/ar5000715, 2014.

Kaleschke, L., Richter, A., Burrows, J., Afe, O., Heygster, G., Notholt, J., Rankin, A. M., Roscoe, H. K., Hollwedel, J., Wagner, T., and Jacobi, H. W.: Frost flowers on sea ice as a source of sea salt and their influence on tropospheric halogen chemistry, Geophysical Research Letters, 31, doi: 10.1029/2004GL020655, URL http://www.agu.org/pubs/crossref/2004/2004GL020655.shtml, 2004.

Kalnajs, L. E. and Avallone, L. M.: Frost flower influence on springtime boundary-layer ozone depletion events and atmospheric bromine levels, Geophysical Research Letters, 33, L10 810, doi: 10.1029/2006GL025809, URL http://www.agu.org/pubs/crossref/2006/2006GL025809.shtml, 2006.

Krnavek, L., Simpson, W. R., Carlson, D., Dominé, F., Douglas, T. A., and Sturm, M.: The chemical composition of surface snow in the Arctic: Examining marine, terrestrial, and atmospheric influences, Atmospheric Environment, 50, 349 – 359, doi: http://dx.doi.org/10.1016/j.atmosenv.2011.11.033, URL http://www.sciencedirect.com/science/article/pii/S1352231011012192, 2012.

Kuo, M. H., Moussa, S. G., and McNeill, V. F.: Modeling interfacial liquid layers on environmental ices, Atmospheric Chemistry and Physics, 11, 9971–9982, doi: 10.5194/acp-11-9971-2011, URL http://www.atmos-chem-phys.net/11/9971/2011/, 2011.

Legagneux, L., Cabanes, A., and Dominé, F.: Measurement of the specific surface area of 176 snow samples using methane adsorption at 77 K, Journal of Geophysical Research, 107, doi: 10.1029/2001JD001016, URL http://www.agu.org/pubs/crossref/2002/2001JD001016.shtml, 2002.

Martin, S., Drucker, R., and Fort, M.: A laboratory study of frost flower growth on the surface of young sea ice, Journal of Geophysical Research, 100, 7027–7036, doi: 10.1029/94JC03243, URL http://www.agu.org/pubs/crossref/1995/94JC03243.shtml, 1995.

Martin, S., Yu, Y., and Drucker, R.: The temperature dependence of frost flower growth on laboratory sea ice and the effect of the flowers on infrared observations of the surface, Journal of Geophysical Research, 101, 12 111–12 125, doi: 10.1029/96JC00208, URL http://www.agu.org/pubs/crossref/1996/96JC00208.shtml, 1996.

McElroy, C., McLinden, C., and McConnell, J.: Evidence for bromine monoxide in the free troposphere during the Arctic polar sunrise, Nature, 397, 2–5, URL http://www.nature.com/nature/journal/v397/n6717/abs/397338a0.html, 1999.

Monnin, C. and Dubois, M.: Thermodynamics of the CsCl-H 2 0 system at low temperatures, European Journal of Mineralogy, pp. 477–482, 1999.

Moore, C. W., Obrist, D., Steffen, A., Staebler, R. M., Douglas, T. A., Richter, A., and Nghiem, S. V.: Convective forcing of mercury and ozone in the Arctic boundary layer induced by leads in sea ice., Nature, doi: 10.1038/nature12924, URL http://www.ncbi.nlm.nih.gov/pubmed/24429521, 2014.

Nghiem, S. V., Rigor, I. G., Richter, A., Burrows, J. P., Shepson, P. B., Bottenheim, J., Barber, D. G., Steffen, A., Latonas, J., Wang, F., Stern, G., Clemente-Colón, P., Martin, S., Hall, D. K., Kaleschke, L., Tackett, P., Neumann, G., and Asplin, M. G.: Field and satellite observations of the formation and distribution of Arctic atmospheric bromine above a rejuvenated sea ice cover, Journal of Geophysical Research, 117, D00S05, doi: 10.1029/2011JD016268, URL http://www.agu.org/pubs/crossref/2012/2011JD016268.shtml, 2012.

Oldridge, N. W. and Abbatt, J. P. D.: Formation of gas-phase bromine from interaction of ozone with frozen and liquid NaCl/NaBr solutions: quantitative separation of surficial chemistry from bulk-phase reaction., The Journal of Physical Chemistry A, 115, 2590–8, doi: 10.1021/jp200074u, URL http://www.ncbi.nlm.nih.gov/pubmed/21388165, 2011.

Perovich, D. K. and Richter-Menge, J. A.: Surface characteristics of lead ice, Journal of Geophysical Research, 99, 16 341–16 350, doi: 10.1029/94JC01194, 1994.

Piot, M. and von Glasow, R.: The potential importance of frost flowers, recycling on snow, and open leads for ozone depletion events, Atmospheric Chemistry and Physics, 8, 2437–2467, doi: 10.5194/acp-8-2437-2008, URL http://www.atmos-chem-phys.net/8/2437/2008/, 2008.

Pringle, D. J., Miner, J. E., Eicken, H., and Golden, K. M.: Pore space percolation in sea ice single crystals, Journal of Geophysical Research, 114, 1–14, doi: 10.1029/2008JC005145, 2009.

Rankin, A. M., Wolff, E. W., and Martin, S.: Frost flowers: Implications for tropospheric chemistry and ice core interpretation, Journal of Geophysical Research, 107, doi: 10.1029/2002JD002492, URL http://www.agu.org/pubs/crossref/2002/2002JD002492.shtml, 2002.

Rivers, M. L. and Gualda, G. A. R.: 'tomo_display' and 'vol_tools': IDL VM packages for tomography data reconstruction; processing; and visualization, Eos (Transactions; American Geophysical Union), 90, 2009.

Roscoe, H. K., Brooks, B., Jackson, A. V., Smith, M. H., Walker, S. J., Obbard, R. W., and Wolff, E. W.: Frost flowers in the laboratory: Growth, characteristics, aerosol, and the underlying sea ice, Journal of Geophysical Research, 116, D12 301, doi: 10.1029/2010JD015144, URL http://doi.wiley.com/10.1029/2010JD015144, 2011.

Schroeder, W., Anlauf, K., Barrie, L., and Lu, J.: Arctic springtime depletion of mercury, Nature, pp. 16–17, doi: 10.1038/28530, URL http://www.nature.com/nature/journal/v394/n6691/abs/394331a0.html, 1998.

Simpson, W., Alvarez-Aviles, L., Douglas, T. A., Sturm, M., and Dominé, F.: Halogens in the coastal snow pack near Barrow, Alaska: Evidence for active bromine air-snow chemistry during springtime, Geophysical Research Letters, 32, doi: 10.1029/2004GL021748, 2005.

Simpson, W. R., Carlson, D., Hönninger, G., Douglas, T. A., Sturm, M., Perovich, D., and Platt, U.: First-year sea-ice contact predicts bromine monoxide (BrO) levels at Barrow, Alaska better than potential frost flower contact, Atmospheric Chemistry and Physics, 7, 621–627, doi: 10.5194/acp-7-621-2007, URL http://www.atmos-chem-phys.net/7/621/2007/, 2007a.

Simpson, W. R., von Glasow, R., Riedel, K., Anderson, P., Ariya, P., Bottenheim, J., Burrows, J., Carpenter, L. J., Frieß, U., Goodsite, M. E., Heard, D., Hutterli, M., Jacobi, H.-W., Kaleschke, L., Neff, B., Plane, J., Platt, U., Richter, A., Roscoe, H., Sander, R., Shepson, P., Sodeau, J., Steffen, A., Wagner, T., and Wolff, E.: Halogens and their role in polar boundary-layer ozone depletion, Atmospheric Chemistry and Physics, 7, 4375–4418, doi: 10.5194/acp-7-4375-2007, URL http://www.atmos-chem-phys.net/7/4375/2007/, 2007b.

Steffen, A., Douglas, T., Amyot, M., Ariya, P., Aspmo, K., Berg, T., Bottenheim, J., Brooks, S., Cobbett, F., Dastoor, A., Dommergue, A., Ebinghaus, R., Ferrari, C., Gardfeldt, K., Goodsite, M. E., Lean, D., Poulain, A. J., Scherz, C., Skov, H., Sommar, J., and Temme, C.: A synthesis of atmospheric mercury depletion event chemistry in the atmosphere and snow, Atmospheric Chemistry and Physics, 8, 1445–1482, doi: 10.5194/acp-8-1445-2008, URL http://www.atmos-chem-phys.net/8/1445/2008/, 2008.

Style, R. W. and Worster, M. G.: Frost flower formation on sea ice and lake ice, Geophysical Research Letters, 36, doi: 10.1029/2009GL037304, URL http://www.agu.org/pubs/crossref/2009/2009GL037304.shtml, 2009.

Sutton, S. R., Bertsch, P. M., Newville, M., Rivers, M., Lanzirotti, A., and Eng, P.: Microfluorescence and Microtomography Analyses of Heterogeneous Earth and Environmental Materials, Reviews in Mineralogy and Geochemistry, 49, 429–483, doi: 10.2138/rmg.2002.49.8, URL http://rimg.geoscienceworld.org/cgi/doi/10.2138/rmg.2002.49.8, 2002.

Thomas, J. L., Stutz, J., Lefer, B., Huey, L. G., Toyota, K., Dibb, J. E., and von Glasow, R.: Modeling chemistry in and above snow at Summit, Greenland âĂŞ Part 1: Model description and results, Atmospheric Chemistry and Physics, 11, 4899–4914, doi: 10.5194/acp-11-4899-2011, URL http://www.atmos-chem-phys.net/11/4899/2011/, 2011.

Wagner, T., Leue, C., Wenig, M., Pfeilsticker, K., and Platt, U.: Spatial and temporal distribution of enhanced boundary layer BrO concentrations measured by the GOME instrument aboard ERS-2, Journal of Geophysical Research, 106, 24 225, doi: 10.1029/2000JD000201, URL http://doi.wiley.com/10.1029/2000JD000201, 2001.

Wennberg, P. O.: Bromine explosion, Nature, 397, 299–301, doi: 10.1038/16805, URL http://dx.doi.org/10.1038/16805, 1999.

Wren, S. N. and Donaldson, D. J.: How does deposition of gas phase species affect pH at frozen salty interfaces?, Atmospheric Chemistry and Physics, 12, 10 065–10 073, doi: 10.5194/acp-12-10065-2012, URL http://www.atmos-chem-phys.net/12/10065/2012/, 2012.

Wren, S. N., Kahan, T. F., Jumaa, K. B., and Donaldson, D. J.: Spectroscopic studies of the heterogeneous reaction between $O_{3(g)}$ and halides at the surface of frozen salt solutions, Journal of Geophysical Research, 115, 1–8, doi: 10.1029/2010JD013929, URL http://www.agu.org/pubs/crossref/2010/2010JD013929.shtml, 2010.

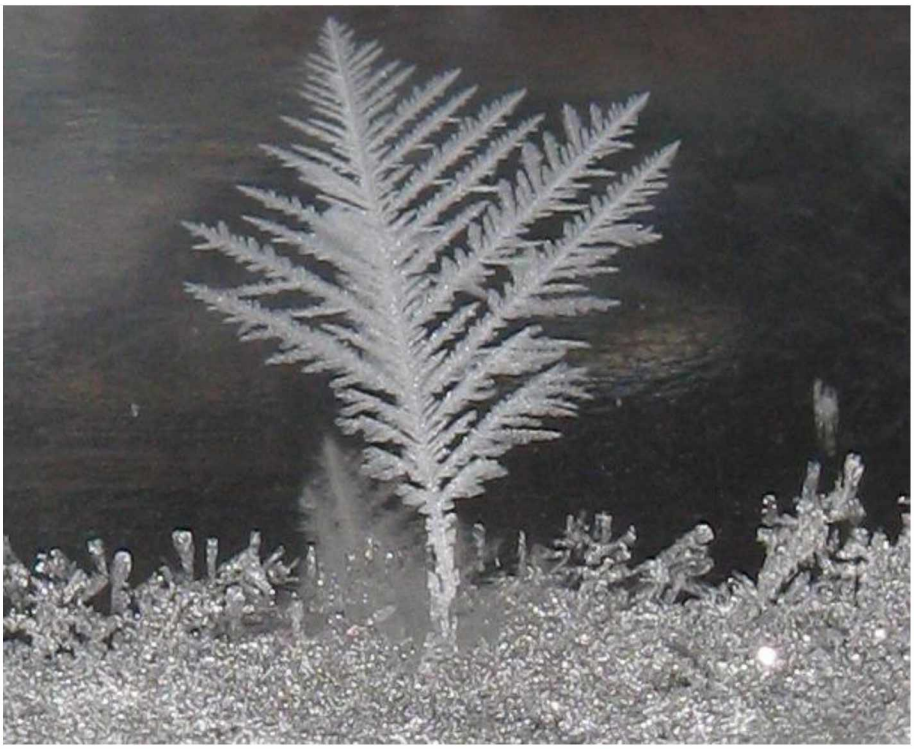

Figure 2.1: An example of a sample grown for analysis in this study.

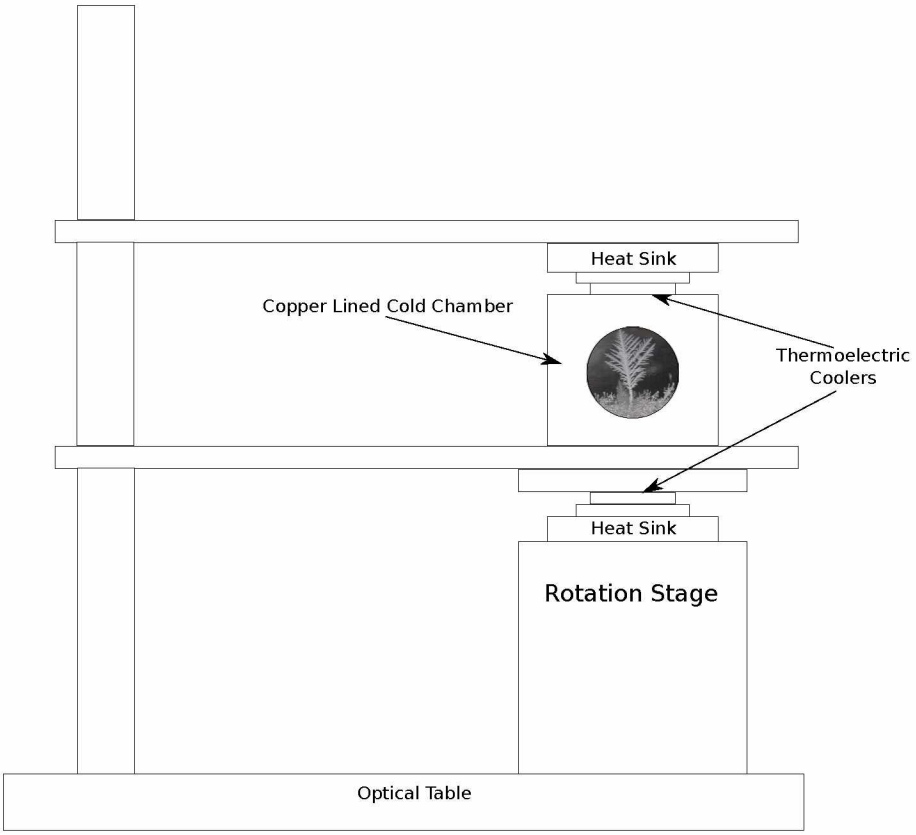

Figure 2.2: Sketch of the cold stage to regulate sample temperature. The cold chamber and thermoelectric coolers are encased in 1" foam (omitted in this schematic for clarity) to insulate the sample chamber. The apparatus is shown perpendicular to the X-ray beam, the scintillator sits approximately 6 inches behind the sample window.

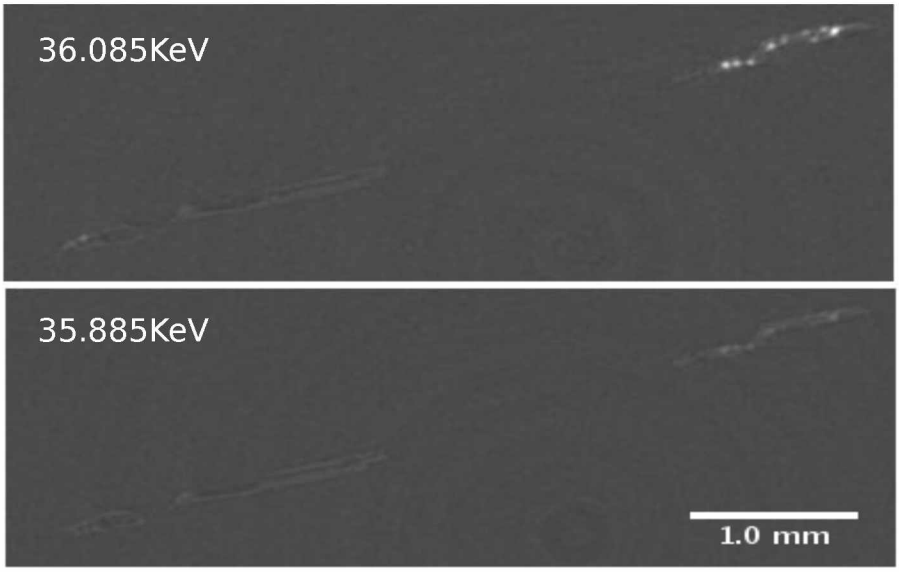

Figure 2.3: Sample cross-section obtained above and below the Cs absorption edge. The vertical axis of the sample is perpendicular to the page. The top image was obtained above the Cs edge and the bottom one below the Cs absorption edge. Above the absorption edge the Cs becomes much more visible.

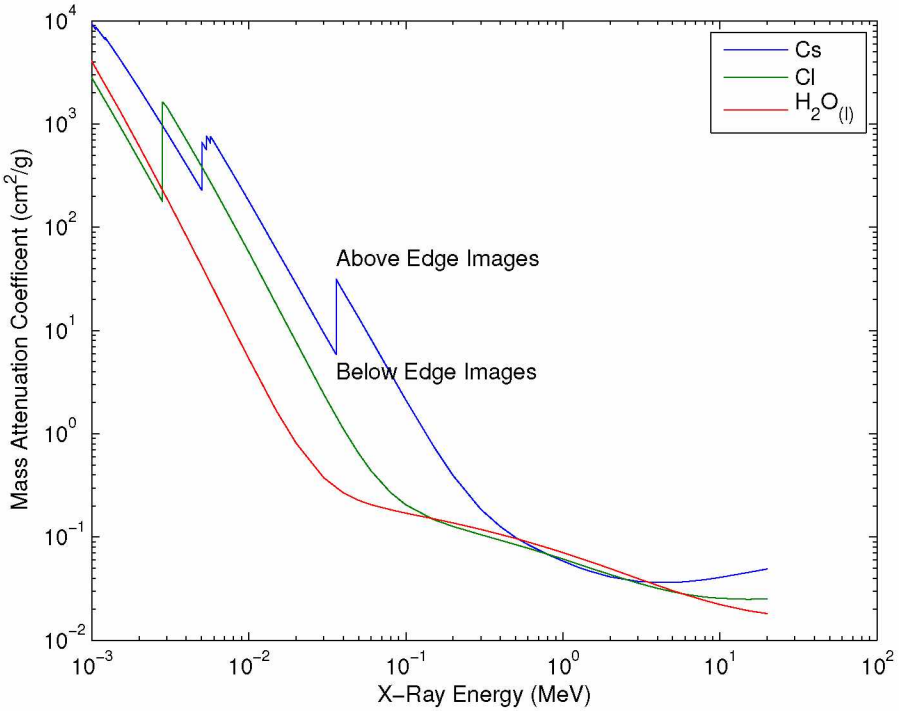

Figure 2.4: X-ray energies at which these data are collected as well as the attenuation of each of the sample components. Because the energy difference between the above and below edge tomograms is only .2 keV, the attenuation of the other elements is essentially static between the two images. (Data from NIST (Hubbell and Seltzer, 2004))

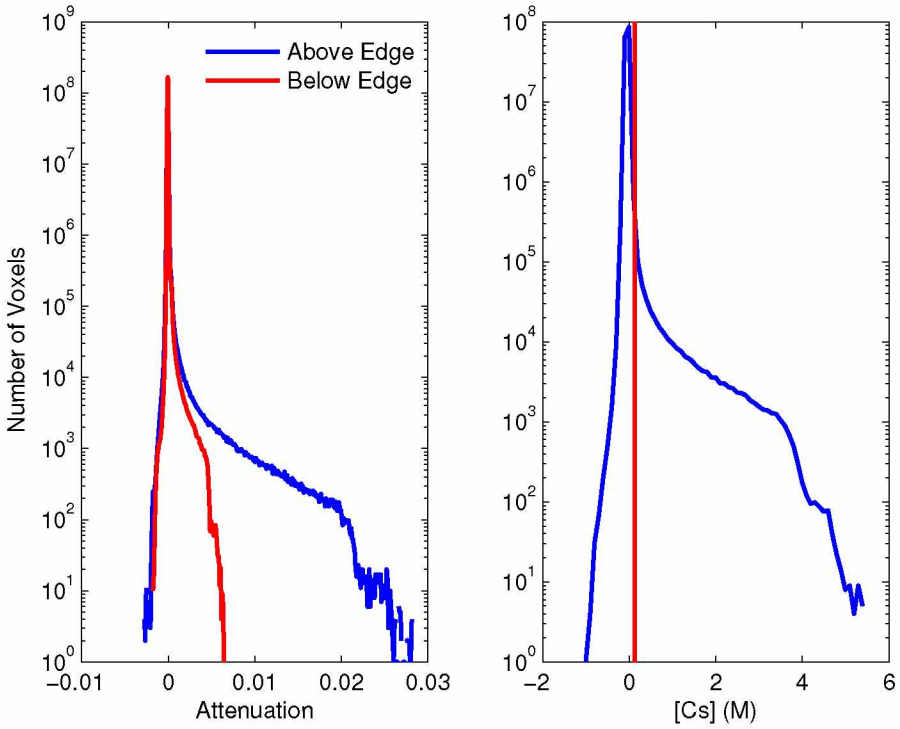

Figure 2.5: The distribution of voxel averaged cesium concentrations is calculated from the difference of above and below edge tomograms. The left panel shows histograms for both the above (blue) and below (red) images. The right panel shows the resulting histogram of voxel averaged cesium concentrations. The red line indicates the threshold value used to distinguish brine voxels from the background. Note that in both panels, the y axis is a log scale

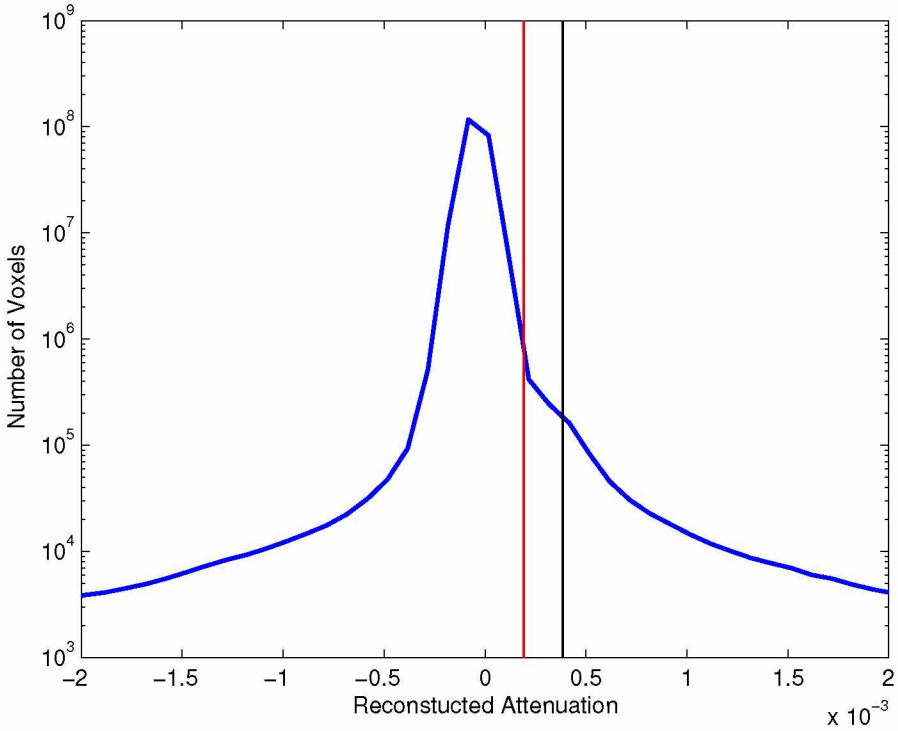

Figure 2.6: The distribution of reconstructed attenuation values for the Cs subtracted below edge tomogram. The red line indicates the threshold value used to separate background and ice, while the black line indicates the theoretical attenuation of voxels that are 100% full of ice. Note that the y axis is a log scale.

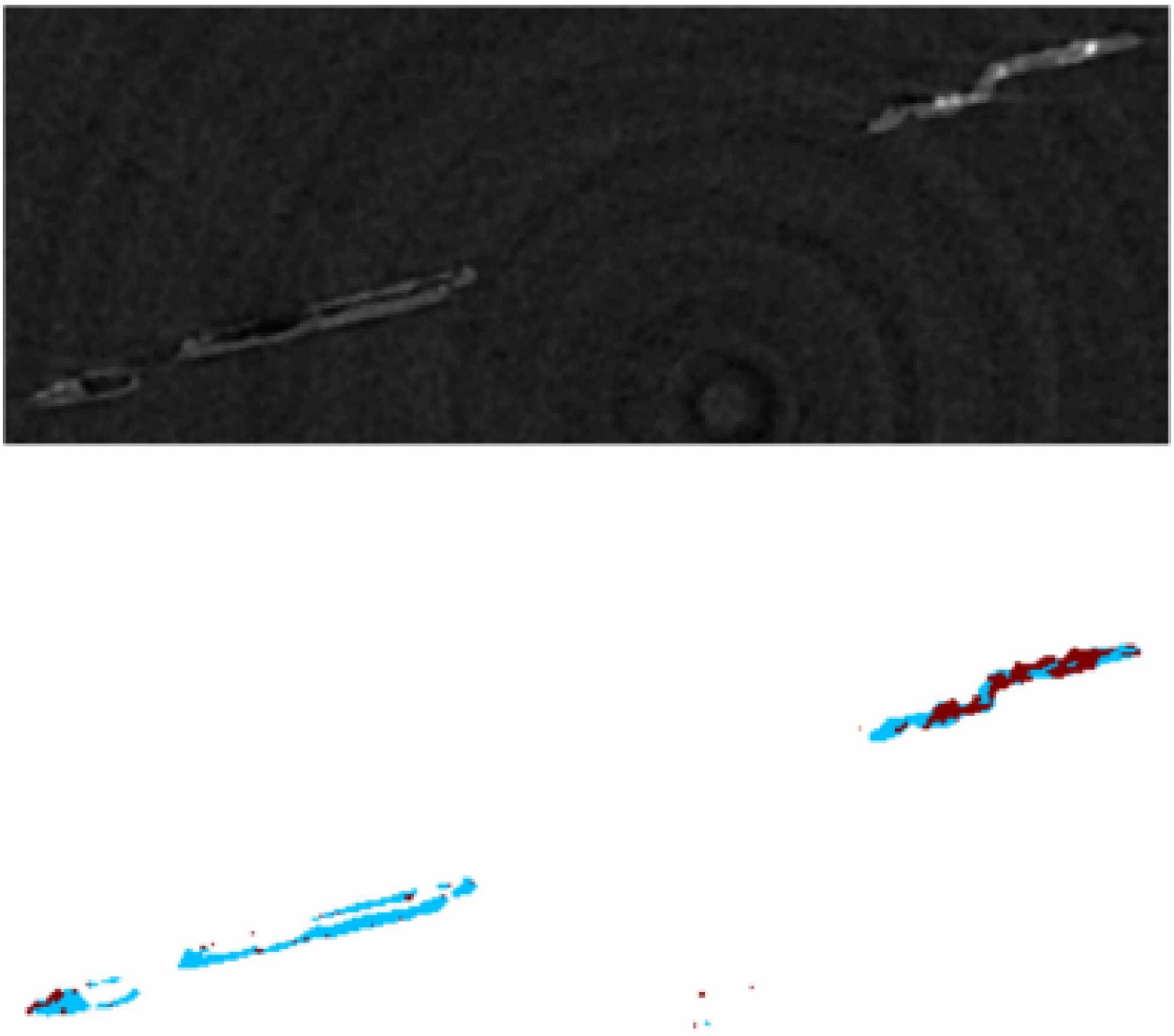

Figure 2.7: Results of the segmentation procedure are shown here on the bottom panel. Ice voxels with no brine are shown in teal, and voxels with detectable brine are shown in red. The top panel shows the original image for comparison.

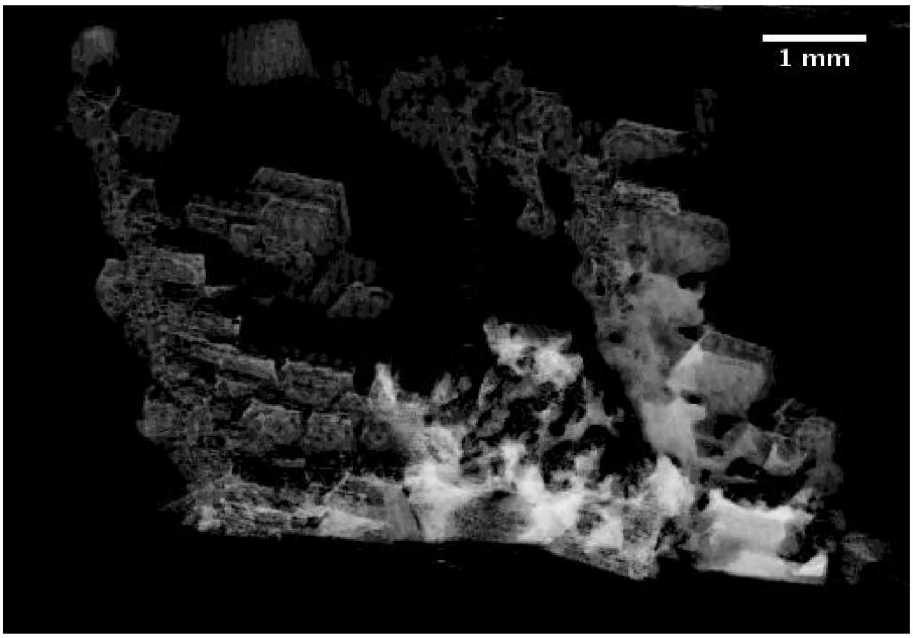

Figure 2.8: Three dimensional rendering of frost flower tomographic data taken below the Cs absorption edge. The brighter regions represent CsCl wicking up the frost flower. The data was obtained at a temperature of $-24\,^{\circ}$C and an X-ray energy of 35.885 keV.

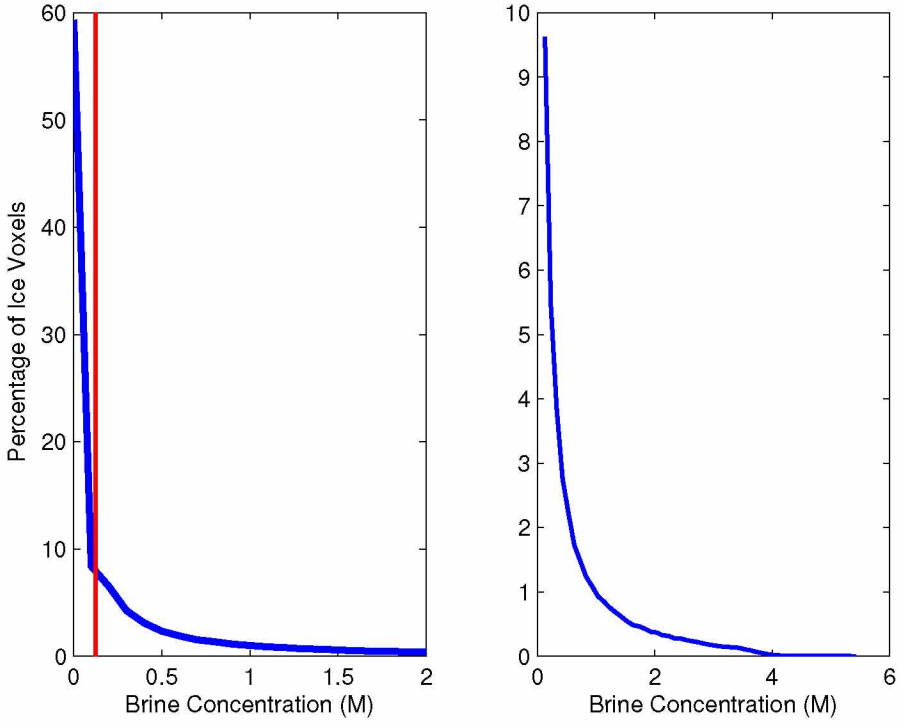

Figure 2.9: Histograms of voxel brine content in a vapor deposited ice sample. The left panel shows the distribution of voxel brine content for the entire sample. The red line indicates the brine detection limit. The right panel is calculated in the same manner as the left, but only shows the distribution of brine voxels above the detection limit. Note that the scales of the y axis in each panel are different.

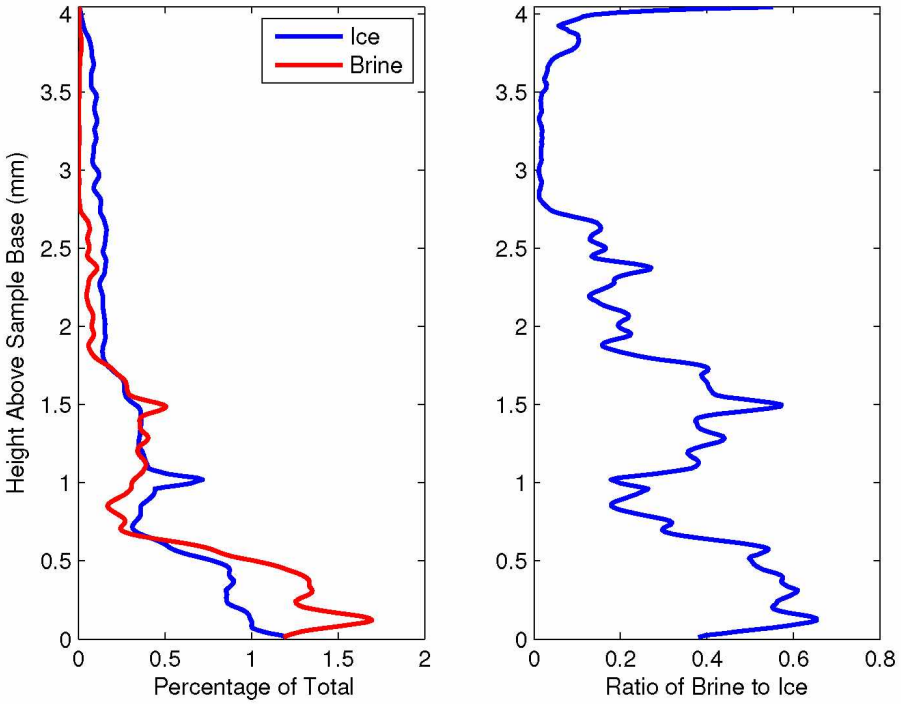

Figure 2.10: The left panel shows distributions of ice (blue), and brine (red) as a function of height. The right panel shows the ratio of brine to ice in each slice as a function of height. In each panel, the y axis is truncated at the top of the sample.

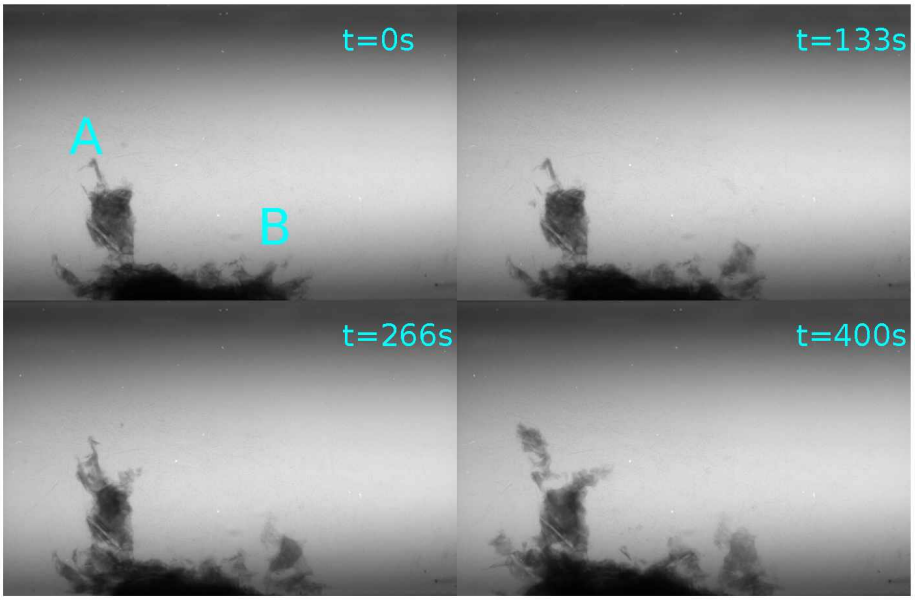

Figure 2.11: Four still frames taken from a 2-D X-ray movie of a warming sample. Regions A and B, marked on the top left frame show evolution of the brine distribution over the duration of the movie. Dark spots indicate increased attenuation due to brine. The sample is rotated to maximize the sample surface perpendicular to the X-ray beam.

Chapter 3

Dependence of the Vertical Distribution of Bromine Monoxide in the Lower Troposphere on Meteorological Factors such as Wind Speed and Stability [1]

3.1 Abstract

Multiple axis differential absorption spectroscopy (MAX-DOAS) measurements of bromine monoxide (BrO) probed the vertical structure of halogen activation events during March–May 2012 at Barrow, Alaska. An analysis of the BrO averaging kernels and degrees of freedom obtained by optimal-estimation-based inversions from raw MAX-DOAS measurements reveals the information is best represented by reducing the retrieved BrO profile to two quantities: the integrated column from the surface through 200 m ($VCD_{200\,m}$), and the lower tropospheric vertical column density (LT-VCD), which represents the integrated column of BrO from the surface through 2 km. The percentage of lower tropospheric BrO in the lowest 200 m was found to be highly variable ranging from shallow layer events, where BrO is present primarily in the lowest 200 m, to distributed column events where BrO is observed at higher altitudes. The highest observed LT-VCD events occurred when BrO was distributed throughout the lower troposphere, rather than concentrated near the surface. Atmospheric stability in the lowest 200 m influenced the percentage of LT-VCD that is in the lowest 200 m, with inverted temperature structures having a first-to-third quartile range (Q1–Q3) of $VCD_{200\,m}$/LT-VCD from 15–39 %, while near-neutral-temperature structures had a Q1–Q3 range of 7–13 %. Data from this campaign show no clear influence of wind speed on either lower tropospheric bromine activation (LT-VCD) or the vertical distribution of BrO, while examination of seasonal trends and the temperature dependence of the vertical distribution supported the conclusion that the atmospheric stability affects the vertical distribution of BrO.

3.2 Introduction

The seasonal return of sunlight during late winter in the polar regions is associated with production of reactive halogens (e.g., Br, BrO, Cl) from saline ice surfaces (Abbatt et al., 2012; Saiz-Lopez and von Glasow, 2012). These halogen species influence boundary layer chemistry through phenomena such as boundary layer ozone depletion events (ODEs) (Barrie et al., 1988; Simpson et al., 2007b) and mercury deposition events (MDEs) (Schroeder et al., 1998; Steffen et al., 2008). While the production mechanism of these halogens is not fully understood, modeling (e.g., Fan and Jacob, 1992; Mozurkewich, 1995; Lehrer et al., 2004; Piot and von Glasow, 2007; Yang et al.,

[1] Published as Peterson, P. K., Simpson, W. R., Pratt, K. A., Shepson, P. B., Frieß, U., Zielcke, J., Platt, U., Walsh, S. J., and Nghiem, S. V.: Dependence of the vertical distribution of bromine monoxide in the lower troposphere on meteorological factors such as wind speed and stability, Atmos. Chem. Phys., 15, 2119-2137, doi:10.5194/acp-15-2119-2015, 2015.

2010; Parrella et al., 2012; Toyota et al., 2014), laboratory (e.g., Fickert et al., 1999; Huff and Abbatt, 2000; Wren et al., 2013) and field studies (e.g., Foster et al., 2001; Spicer et al., 2002; Toom-Sauntry and Barrie, 2002; Krnavek et al., 2012; Pratt et al., 2013; Liao et al., 2014) point to heterogeneous chemistry involving salts present on ice surfaces (e.g., NaBr, NaCl) as important sources of reactive halogens.

Multiple studies have examined the vertical extent of ODEs that result from halogen chemistry and have shown ODE vertical structure to be highly variable (Bottenheim et al., 2002; Jones et al., 2010; Helmig et al., 2012; Oltmans et al., 2012). Jones et al. (2010) suggest a link between ozone depletion at higher altitudes and low-pressure systems (storms) from Antarctic observations, but also point out that this relationship may not be the case in the Arctic due to differing meteorology. Ozonesonde data from ARCTAS/ARCPAC and OASIS campaigns presented in Oltmans et al. (2012) show the vertical extent of ozone depletion varies between 200 and 1000 m, and that this difference may be tied to the origin of the observed air masses in addition to the local meteorology. Although the profile of ozone depletion gives some insights into the vertical structures of the reactive halogens that deplete ozone, the differing chemical lifetimes of ozone (a day to longer) and reactive halogens (minutes to hour unless recycled by heterogeneous chemistry on particles) may mean that halogen vertical profiles differ from ozone depletion profiles. Tackett et al. (2007) present a view from tethered balloon measurements of a stratified lower boundary layer, in which the rates of ozone and Hg depletion are determined by downward mixing into the halogen-chemistry-active surface layer. Moore et al. (2014) found that both ozone and mercury levels recovered to higher levels when vertical mixing induced by sea ice leads had recently influenced the observed air masses, but the effect of this mixing on reactive halogens is not known. The work of Frieß et al. (2011) used MAX-DOAS (multiple axis differential absorption spectroscopy) observations along with optimal-estimation-based inversions to retrieve BrO concentration profiles and showed significant variability in vertical structure with reactive halogens typically being in the lowest ~ 1 km of the atmosphere, similar to the ozone-depleted layer.

The physical mechanisms for the transport of reactive halogens from the snowpack to the boundary layer and recycling of those halogens aloft are still poorly understood. Given the short lifetime of BrO in the absence of heterogeneous recycling (McConnell et al., 1992; Platt and Hönninger, 2003), it is likely that some sort of aerosol particles (Fan and Jacob, 1992), either from blowing snow or other sources, are required to sustain halogen activation aloft. Recent literature in particular has focused on the role of blowing snow events in halogen activation (e.g., Jones et al., 2009, 2010; Yang et al., 2010; Frieß et al., 2011). In particular, Jones et al. (2009) used O_3 observations at Halley station in Antarctica to derive a model for the dependence of ODEs on wind speed. Jones

et al. (2009) suggest that there are two environmental regimes that favor local halogen activation and subsequent ozone depletion. One regime consists of low wind speeds and a stable boundary layer, the other requires high winds and the presence of blowing snow. Blowing snow events occur when high winds loft snow, potentially enhancing available snow surface area available for reaction. Blowing snow may shift reactive halogens aloft through reactions on the blowing snow or aerosol particles produced by sublimed blowing snow (Jones et al., 2009, 2010; Yang et al., 2010; Frieß et al., 2011). Comparison of satellite-observed column BrO data with modeling results by Yang et al. (2010) suggests that blowing snow events may be sufficient to explain the majority of halogen activation events observed via satellite. In contrast, Halfacre et al. (2014) conducted an analysis at a variety of locations across the Arctic and found no relationship between observed ozone and wind speed, suggesting that high wind speeds and, consequently, blowing snow may not play a major role in ozone depletion. Again, because of the differing chemical lifetimes of ozone and reactive halogens, using ozone depletion as a proxy for halogen activation requires caution.

To examine these ideas further, it is necessary to observe both the total amount of reactive halogens, and their distribution throughout the lower troposphere. While satellite measurements (e.g., Wagner and Platt, 1998; Richter et al., 1998; Chance, 1998) provide extensive spatial coverage of the Arctic, they only measure the total column of BrO, and do not provide vertical profile or near-surface information. Multiple methods exist to separate total column measurements into stratospheric and tropospheric components (e.g., Theys et al., 2011; Salawitch et al., 2010; Koo et al., 2012; Sihler et al., 2012). However, discrepancies still exist between ground-based and satellite-based measurements, potentially due to clouds masking portions of the tropospheric BrO column from satellite views. Additionally, Theys et al. (2009) and Salawitch et al. (2010) showed that some of the variability of total column BrO arises from stratospheric variability; thus, not all satellite-detected BrO "hotspots" are actually lower tropospheric halogen activation events. In situ chemical ionization mass spectrometry (e.g., Liao et al., 2011; Pratt et al., 2013; Liao et al., 2014) and long-path differential optical absorption spectroscopy (LP-DOAS) (e.g., Tuckermann et al., 1997; Pöhler et al., 2010) fail to capture the vertical extent of halogen activation, except in the case of limited aircraft-based campaigns (e.g., Neuman et al., 2010; Liao et al., 2012) and, thus, cannot address questions about the total amount of halogen activation taking place at a given time. However, the Tackett et al. (2007) work implied that much of the halogen chemistry is occurring in the lowest ~ 200 m of the boundary layer.

MAX-DOAS has the ability to retrieve vertical profiles of BrO in the lowest few kilometers and, thus, can examine the variability of the vertical distribution of BrO over time (Frieß et al., 2011). The present work builds on the method of Frieß et al. (2011) by considering the BrO averaging

kernels, which provide information on the sensitivity of these BrO measurements (Payne et al., 2009), to identify what observations are independent of the a priori assumed profile of BrO and creating a consistent time series of these data over a field campaign. Through this analysis, we identify two relevant properties of the BrO vertical profile, the partial vertical column density (VCD) of BrO in the lowest 200 m (termed VCD_{200m}) and the lower tropospheric partial VCD (termed LT-VCD). The present work explores the dependence of these BrO profile properties on environmental factors to investigate activation of BrO and its propagation outside of the near-surface layer over time. This present work focuses on measurements occurring near Barrow, Alaska, during the Bromine, Ozone, and Mercury Experiment (BROMEX) campaign (Nghiem et al., 2013) from 6 March to 15 May 2012. The primary MAX-DOAS observations were made from the roof of the Barrow Arctic Research Center (BARC) building at 71.325° N, 156.668° W, which is about 6 km northeast of the city of Barrow, Alaska, with a viewing azimuth of 27° east of true north.

3.3 Methods

3.3.1 MAX-DOAS measurements

MAX-DOAS probes vertical distributions of trace gases above a measurement site through a combination of spectroscopic measurements of scattered sunlight and modeling of vertical profiles consistent with those observations (Hönninger et al., 2004). The instrument measures spectra of scattered sunlight in a region where the molecule of interest absorbs as a function of elevation angle of a telescope receiving the light. Measurements at all elevation angles contain absorption features due to stratospheric and higher tropospheric gases and, because most sunlight is scattered in the lower atmosphere, these stratospheric absorption features are common to observations at all elevation angles. Measurements at low-elevation angles contain enhanced absorption for gases present near the ground, due to the tangent geometry of the light's final path to enter the telescope at a low elevation. Therefore, analysis of the relative absorption spectrum comparing light at low-elevation angles to high-elevation angles provides high sensitivity to near-ground absorbers with greatly reduced sensitivity to stratospheric and upper tropospheric gases.

The instrument used in this study is similar to the one described in Carlson et al. (2010) with a few improvements. In this study, we measured scattered sunlight using a QE-65000 (Ocean Optics) spectrometer with spectral range from 309 to 397 nm and optical resolution of 0.39 nm full width at half maximum. This new spectrometer is improved by using a thermoelectrically cooled detector, stabilized at −15 °C. The spectrometer optical bench is heated to 38 °C, with a standard deviation of 0.6 °C over the full campaign, to improve optical alignment stability.

Another improvement of the instrument is the use of a MEMS (micro-electromechanical system) tiltmeter (SignalQuest SQ-SI-360DA-3.3R-HMP-HP-IND-S) mounted on the moving telescope that directly measures the elevation angle of the observation. The scan pattern measures scattered sunlight at elevation angles of 90 (zenith), 20, 10, 5, 2, and 1° over a period of approximately 30 min.

We used QDOAS software (Fayt et al., 2011) to fit the relative absorption spectrum between near-temporally coincident low-elevation and zenith observations to a linear combination of possible absorbing spectra to quantify the differential slant column density (dSCD) of each absorbing gas at each elevation angle. We performed this analysis in the wavelength window between 346 and 364 nm. The absorber cross sections are detailed in Table 4.1 and are convoluted with an instrumental transfer function measured from the 334 nm line of a low-pressure mercury lamp. In addition to gaseous absorbers, we include a third-order polynomial to account for Rayleigh and Mie scattering by gases and particles in the atmosphere, and a spectral offset to account for stray light within the spectrometer. The mean residual root mean square (rms) of our dSCD retrieval was 3.9×10^{-4}. Data collected during low-light conditions conditions (solar zenith angle $> 85°$), rms $> 10^{-3}$, or when frost is detected on the instrument's optical window are discarded. The dSCD fitting errors (1σ) over the campaign average 1.9×10^{13} molecules cm^{-2} for BrO and 5.1×10^{41} molecules^2 cm^{-5} for O_4. The sensitivity of the rms and dSCD errors to the elevation angle was small ($< 15\,\%$) and is documented in the Supplement.

3.3.2 Retrieval of vertical profiles

Retrieval of trace gas vertical profiles from dSCD data is a two-step procedure. First, we determine the aerosol particle extinction vertical profile from O_2 collisional dimer (O_4) dSCD measurements using an optimal estimation procedure detailed in Frieß et al. (2006) and briefly described here. The observed O_4 dSCD values are strongly dependent on atmospheric visibility and light scattering, which we are able to deduce because we know the vertical profile of O_4. Measured O_4 dSCDs are compared to values modeled using the SCIATRAN radiative transfer model (Rozanov et al., 2005), which depend on a variable aerosol particle extinction profile and static parameters such as the viewing geometry and aerosol particle light scattering properties. Assumptions made about the aerosol optical properties are set to values typical for clean ice crystals, following the procedures detailed in Frieß et al. (2011). Because the measured O_4 data alone do not provide enough information to retrieve the profile, we used an assumed a priori profile to further constrain the solution, as described by Rodgers (2000). We used a variable a priori profile that peaks at the surface and exponentially decays with altitude. Initially, the profile peaks at the surface with an aerosol particle extinction value of 0.05 km^{-1} and exponentially decays with a scale height of 1 km.

The initial a priori covariance matrix is constructed with the diagonal elements being the square root of 3 times the a priori extinction and the off-diagonal elements being set to 0. The a priori covariance matrix is changed with every iteration (Frieß et al., 2006). In following iterations, the a priori is set to the retrieved profile and smoothed using a boxcar average with a width of 300 m (Frieß et al., 2006). The final output of this first step is a vertical profile of aerosol particle extinction.

The procedure to retrieve the BrO profile from BrO dSCD measurements is described in detail in Frieß et al. (2011). Briefly, we used the above-retrieved aerosol particle extinction profiles as input to a Monte Carlo radiative transfer model (McArtim, Deutschmann et al., 2011) that simulates BrO dSCDs as a function of a variable BrO vertical concentration profile. The vertical profile of BrO is varied to give best fit to the BrO dSCD observations, again by optimal estimation. In the case of BrO, the a priori profile peaks at the surface with a value of $10\,\mathrm{pmol\,mol^{-1}}$ and exponentially decays with a scale height of 400 m. The result of the second step is the average BrO mixing ratio every 100 m from the ground to an altitude of 2 km. An example of the retrieved profile is shown in green in Fig. 3.1. Note that while our general retrieval uses a 400 m scale height for the a priori profile of BrO, Fig. 3.1 also includes the effect of modifying the a priori profile to have a different (1000 m) scale height (dashed blue line), as described below.

3.3.3 Information content of the profile

The retrieved BrO profiles contain average mixing ratios in twenty 100 m thick layers from the surface to 2 km; however, they are based on only five low-elevation spectral measurements of BrO dSCD. Therefore, it is clear that our observations contain less information about the true vertical profile than is represented in Fig. 3.1. The optimal estimation method used the assumed a priori information to constrain the fit in the absence of further information, but the actual vertical profile of BrO is not known. In fact, the results of this study indicate that both the BrO abundance and vertical profile shape vary over time. Therefore, the full profile, as retrieved by optimal estimation, lends itself to overinterpretation of the observations and we seek to find a method to determine the actual information content, as well as to reduce the number of derived properties to reflect the true observations more accurately.

As described in Rodgers (2000), the retrieved profile contains true profile information as well as a bias toward the assumed a priori profile. The extent to which the retrieved profile depends on the dSCD measurement data is determined by examining the averaging kernel matrix. An example of the BrO averaging kernels for a MAX-DOAS retrieval is given in the left panel of Fig. 3.2. If the value of the diagonal element of the averaging kernel at some altitude were unity (1), it would indicate that all of the information content at that layer is constrained by observational

data and none of the information at that altitude comes from the a priori assumption. Nonzero off-diagonal elements indicate that the retrieved parameter in that layer is not independently resolved and is influenced by results in other layers. There are two peaks in the averaging kernels, one at the surface and one aloft at an altitude of about 300 m. We can understand the sharp peak at the surface easily because MAX-DOAS spectroscopy always has highest sensitivity and greatest vertical resolution in the layer in which the observer resides. In this study, that is the lowest portion of the boundary layer when the measured photons traverse a path tangent to the ground prior to being detected. The broader peak aloft, centered at about 300 m, in this example comes from the observations at higher elevation angles, which view through those aloft layers, but do not provide enough information to independently resolve mixing ratios in 100 m thick layers at higher altitudes. The trace (sum of diagonal elements) of the averaging kernel matrix gives the degrees of freedom (DOF), which represents the total number of independent pieces of information contained in the retrieval. For BrO retrieval using this technique and our instrumentation, the distribution of DOF is well fit by a Gaussian function, with a mean of 2.0 DOF and $\sigma = 0.27$. Our retrievals also exhibit a distinct lack of sensitivity to changes in individual 100 m layers at altitudes over 1000 m. The DOF for this example is 1.99, implying our retrieved profile contains two independent pieces of information, rather than the 20 we retrieved.

To illustrate the influence of our a priori assumptions, Fig. 3.1 also shows a retrieved profile with a different assumed BrO scale height, 1000 m instead of the normal 400 m assumption. The influence of a priori selection in the retrieved BrO mixing ratio in the lowest 200 m is minimal, showing that our instrument is most independent of a priori assumptions about the BrO profile near the surface. However, aloft the effects of a priori selection are clearly visible. What appeared to be a relatively sharp peak at $\approx$ 650 m when the 400 m a priori was assumed becomes much broader with the 1000 m assumed scale height. Note that both optimally estimated results fit the observational data with similar figure of merit (χ^2), so the difference in profile is not due to poor fitting in one case or the other but instead a consequence of the a priori influencing the resultant BrO profile.

3.3.4 Reduction of the full profile

A method for mapping the BrO profile retrieved on a fine grid to a coarse grid such that the DOF are represented as physical quantities without the influence of a priori information, is outlined in von Clarmann and Grabowski (2007). They suggest moving to a variable coarse altitude grid where one would select grid points such that each grid point would represent one DOF. The lowest layer's upper boundary would be determined by summing the diagonal elements of the BrO averaging kernel matrix until the sum reached 1. This process would be repeated to obtain

additional layer boundary altitudes. However, this approach is not practical for long-term time series analysis because the vertical resolution would vary over time, making comparisons difficult. As a compromise, we calculated coarse grid points by examining the ensemble of profile retrievals over this campaign and splitting them into two layers by determining the average altitudes such that each layer contains 1 degree of freedom. This method led us to represent 1 degree of freedom as the abundance of BrO from the surface to 200 m, and another as the abundance of BrO from 200 m to 2.0 km. These two layers differ in thickness due to the enhanced vertical resolution at the surface and decreased vertical resolution aloft, so we choose to represent the abundance in each layer is a partial VCD within each layer. The vertical column density is also useful because satellite total column retrievals of BrO use the same unit of abundance. Thus, our two quantities ($VCD_{200\,m}$ and VCD_{Aloft}) represent a surface layer VCD and a lofted layer VCD, respectively.

Figure 3.1 shows the partial VCDs in each layer derived from the grid coarsening procedure, for an example retrieval. While the profiles look fairly different, particularly aloft, the partial VCDs in each of the layers are only around 10 % different from each other as an effect of the assumed a priori profile. This example shows how the grid coarsening procedure gives results that are less dependent on the unknown but assumed BrO profile.

Payne et al. (2009) describe how to calculate general averaging kernels for a coarsened grid, which we applied to our BrO retrievals. An example of the coarse-grid BrO averaging kernels is shown in Fig. 3.2. The DOF has been reduced, meaning we have lost some information in the transfer to a coarse grid; however, both parameters have averaging kernels that peak within the desired layer and at a value close to unity, implying most of the information comes from the observations. Payne et al. (2009) suggested a cutoff of 0.7 for the diagonal element of the averaging kernel within a layer as sufficiently close to unity to consider the observations as derived from the data and independent of the a priori assumption. We chose to adopt the same cutoff of 0.7 degrees of freedom in the present work.

The right panel of Fig. 3.3 shows the dependence of the aloft information content on the aerosol optical depth. As Fig. 3.3 shows, our ability to retrieve information beyond the near-surface layer is heavily dependent on the aerosol optical depth, while our ability to retrieve information near the surface is less influenced by aerosol particles. In addition to the degrees of freedom cutoff, over the course of the campaign we also observed limited times when the retrieved aerosol optical depth was large, in excess of 2, which indicates that the visibility is insufficient to obtain an accurate profile of aerosol particle extinction or BrO. During these periods, we do not consider the VCD_{Aloft} due to insufficient degrees of freedom, and we also disregard the $VCD_{200\,m}$. This approach is consistent with methods used in comparison of near-surface MAX-DOAS and LP-DOAS BrO measurements by Frieß et al. (2011).

When both quantities have averaging kernels peaking at 0.7 or higher, we refer to the sum as the lower tropospheric vertical column density (LT-VCD). It is important to note that this quantity does not represent a new degree of freedom, as it is derived from and not independent of the other two measurements. To evaluate the vertical distribution of BrO, we examine the ratio of the $VCD_{200\,m}$ / LT-VCD as well as the total amount of observed activation in the lower tropospheric (LT-VCD) and near-surface amounts ($VCD_{200\,m}$). A time series of these three quantities, along with the aerosol optical depth over a portion of the campaign is presented in Fig. 3.4. The rest of the time series can be found in the Supplement. This time series will be discussed below, but here we note that the fraction of BrO in the lower layer varies between a few percent and up to $\approx 80\,\%$. The a priori profile, exponentially decaying with a scale height of 400 m, would have a constant fraction of BrO in the lowest 200 m, approximately 34 %. It is clear that the data show substantially more vertical profile variability than the assumed profile. Therefore, we use the grid-coarsened data to represent the information content from our MAX-DOAS observations over this long time period.

An additional advantage of the coarsened grid is that the resulting quantities are less sensitive to errors in forward model parameters. As an example, the aerosol particle extinction profile required for the BrO retrieval is also an optimally estimated quantity, and not the true profile. This will introduce errors in the BrO retrieval. We estimated the errors in BrO retrieval due to uncertainties in the aerosol particle extinction profile by examining the sensitivity of the BrO retrieval to perturbations in the aerosol particle extinction profile. To do so, we retrieved BrO profiles from the same BrO dSCD data over an ensemble of varying aerosol particle extinction profiles observed during this study, and examined the resulting variability in the quantities further discussed in this manuscript. We found that the LT-VCD was not heavily influenced by changes in the aerosol profile, with an estimated error of 4.6 % (1σ), which is lower than error introduced by uncertainties in the BrO dSCD measurements. The $VCD_{200\,m}$/LT-VCD ratios retrieved have an estimated error of 4.9 % (1σ). Thus, it is reasonable to conclude that the vertical structure of halogen events retrieved using MAX-DOAS at Barrow is not substantially influenced by errors in aerosol retrieval.

3.3.5 Other field sites

Figure 3.5 shows locations for various measurements used in this study. While this paper focuses on MAX-DOAS measurements from the BARC building, Sect. 3.3 makes use of data from multiple field sites to evaluate the effectiveness of our near-surface BrO retrieval. We deployed a second MAX-DOAS instrument, IL1, at 71.355° N, 155.668° W, which is on landfast sea ice east of the BARC building with a viewing azimuth of 2° east of true north. This instrument is identical to

instrument on the BARC building with the exception of the spectrometer, which is an Avantes (AvaSpec-ULS2048x64-USB2) with spectral range from 291 to 457 nm and optical resolution of 0.37 nm full width at half maximum. This spectrometer is housed in a highly insulated enclosure that is stabilized at 10 °C using air cooling. We analyzed MAX-DOAS data from IL1 using the techniques previously described. For IL1, the mean rms of our dSCD retrieval is 5.2×10^{-4}. IL1 dSCD fitting errors (1σ) over the campaign average 9.7×10^{12} molecules cm^{-2} for BrO and 1.7×10^{42} molecules^2 cm^{-5} for O_4 .

Additional surface BrO measurements were conducted near Barrow, AK, from 12 to 28 March 2012 at a measurement site about 5 km inland (71.275° N, 156.641° W), shown in Fig. 3.5, using a chemical ionization mass spectrometer (CIMS), described by Liao et al. (2011). Using hydrated $I^-(I \cdot (H_2O)_n^-)$ as the reagent ion, BrO was measured at mass 222 ($I^{79}BrO^-$) and 224 ($I^{81}BrO^-$). Background measurements were performed every 15 min by passing the air flow through a glass wool scrubber. Br_2 calibrations were performed every 2 h by adding Br_2, from a permeation source, in 21 mL min^{-1} N_2 to the air flow. A relative sensitivity of BrO (mass 224) relative to Br_2 (mass 287) of 0.47 was utilized for BrO calibration (Liao et al., 2011). The presence of BrO was confirmed by the ratio of mass 222 / mass 224 (background-subtracted raw signals), calculated to be 1.01 ($R^2 = 0.94$).

For a measurement cycle of 10.6 s, mass 224 ($I^{81}BrO^-$) was monitored for 0.5 s, giving a 5 % duty cycle. The 3σ limit of detection for BrO, using mass 224, was calculated to be 1.6 pmol mol^{-1}, on average, for a 2.8 s integration period (corresponding to 1 min of CIMS measurements). Since the variance in the background is likely due to counting statistics (Liao et al., 2011), the limit of detection for 30 min averaging is estimated at 0.3 pmol mol^{-1}. The uncertainty in the reported BrO concentrations was calculated to be 30 % +0.3 pmol mol^{-1}. Additional sampling details are provided in the Supplement.

To examine relationships between BrO and ozone, as well as local meteorology, we used ozone data and meteorological data from the National Oceanic and Atmospheric Administration (NOAA) Earth Systems Research Laboratory/Global Monitoring Division (ESRL/GMD). These data included near-surface ozone mixing ratios, temperature, wind speed, wind direction, pressure, as well as twice daily meteorological balloon sounding data from the Barrow Airport (PABR), which was used to calculate the temperature gradient (dT/dz) near the surface. These soundings take place twice daily, at 00:00 UTC (universal time coordinated), which is in the daylight hours, 15:00 AKST (Alaska standard time), at Barrow, and 12:00 UTC, which is at night and not used in this study.

3.4 Results

3.4.1 Relationship between visibility and retrieval information content

The ability of MAX-DOAS to observe BrO beyond the near-surface layer is heavily influenced by the optical properties of the atmosphere (e.g., visibility) at the time of the measurement. The methods outlined above allow us to identify times when MAX-DOAS measurements are sensitive to BrO beyond the near-surface layer and restrict our further analysis of the vertical distribution of BrO to these periods. Figure 3.3 details the relationship between the aerosol optical depth and the information content of the measurement. As the aerosol optical depth increases, the ability to observe the full LT-VCD sharply decreases. As seen in Fig. 3.3, we can retrieve the full LT-VCD 50 % of the time. We excluded periods where we are unable to fully observe the LT-VCD from further analysis of the vertical distribution of BrO.

3.4.2 Influence of ozone

Ambient ozone levels influence the partitioning of reactive halogen species between atomic (e.g., Br atoms) and oxide (e.g., BrO) forms. MAX-DOAS measurements retrieve only BrO and thus only constrain one component of BrO_x (BrO + Br). Therefore, it is important to consider effects of gas-phase partitioning of BrO_x on subsequent conclusions about halogen activation. Under ordinary ozone conditions (ozone mixing ratios of 30–40 $\mathrm{nmol\,mol^{-1}}$), BrO will make up the majority of BrO_x; however, as ozone levels go below approximately 1 $\mathrm{nmol\,mol^{-1}}$, a common occurrence during the ozone depletion event season, our BrO-only measurements could be insufficient to observe reactive halogens, as shown in Helmig et al. (2012). We term this effect "ozone titration" and seek to avoid interpretation of BrO data below some threshold where the effect dominates. The threshold depends on the photolysis rate of BrO, which varies depending on cloud cover and solar zenith angle, among other factors. For the purposes of this study, we used an ozone threshold of $< 1\,\mathrm{nmol\,mol^{-1}}$ to identify potentially titrated air masses to exclude from further analysis (Simpson et al., 2007a). Figure 3.4 shows times when ozone is below 1 $\mathrm{nmol\,mol^{-1}}$ as shaded in gray. Note that, for the most part, BrO LT-VCD and VCD_{200m} are small during ozone titration, as would be expected, and also observed by Neuman et al. (2010).

3.4.3 Influence of air mass history

Air mass history, particularly time spent in sea ice areas, can influence observed BrO at coastal sites (e.g Frieß, 2004; Simpson et al., 2007a). To examine the variability in air mass history during BROMEX, we calculated time spent in sea ice areas over the 72 h prior to each measurement using methods detailed in Simpson et al. (2007a). During BROMEX, all measured air masses spent at

least 25 % of the past 72 h in contact with sea ice while 90 % of measured air masses spent over 75 % of the past 72 h over sea ice. While there is an influence of air mass history on the observed BrO, given the high levels of sea ice contact observed throughout the campaign, it is unlikely that the variability of BrO observed during this campaign can be attributed to variations in air mass history.

3.4.4 Performance of surface BrO retrieval

To evaluate the effectiveness of the BrO retrieval near the surface, we used in situ BrO measurements made using chemical ionization mass spectrometry (CIMS) to evaluate our retrieval in the lowest 100 m. While the mixing ratio in the lowest 100 m is not one of the grid coarsened quantities, because MAX-DOAS is most sensitive near the surface, the near-surface mixing ratio has similar information content to the $VCD_{200\,m}$ while minimizing the effects of vertical averaging in comparison with in situ measurements. Figure 3.6, shows a time series of the average BrO mixing ratio retrieved in the lowest 100 m by MAX-DOAS (red) and in situ CIMS measurements taken 1 m above the snowpack (green). The error associated with 100 m mixing ratios retrieved using MAX-DOAS varies depending on the state of the atmosphere at the time of the measurement. The error associated with each retrieval is determined by examining the sensitivity of the retrieval to dSCD errors associated with the measurement data (Rodgers, 2000). Average errors (2σ) were $4.2\,\mathrm{pmol\,mol^{-1}}$ for our MAX-DOAS measurements. Uncertainties are estimated at $30\,\% + 0.3\,\mathrm{pmol\,mol^{-1}}$ for CIMS measurements. Because the CIMS instrument was also used to conduct snow chamber experiments during BROMEX, and MAX-DOAS observations are daytime only, there are some gaps in the time series shown in Fig. 3.6.

Because CIMS measures in one discrete location just above the snowpack, while MAX-DOAS measurements are spatially averaged both horizontally over 10–20 km and vertically over approximately 100 m, it is expected that large changes in the environment in the view direction of the MAX-DOAS will cause differences between the CIMS and MAX-DOAS observations. We also expect that because the snowpack is a source of Br_2 (Pratt et al., 2013), there may be a significant near-surface BrO gradient. Figure 3.6 shows a time series of near-surface BrO measurements from the CIMS, as well as MAX-DOAS measurements at the BARC building. Since the BARC data originate at ~ 4 m, and average over the lowest 100 m, we might expect MAX-DOAS data to be lower than the CIMS, which measures closer to the snowpack. Figure 3.6 shows agreement for the majority of concurrent observations, excluding the period shaded in gray, during which we observed substantial gradients in the near-surface amounts of BrO at IL1 (blue line) and BARC (red line), which could explain discrepancies between the MAX-DOAS measurements at the BARC building and the CIMS measurements. Figure 3.5 shows the MAX-DOAS instrument on the BARC

building views across a large lead that is not sampled by the IL1 view direction, which could potentially explain a local gradient in BrO. Figure 3.7 shows the overall correlation between MAX-DOAS measurements at the BARC building and the CIMS, each averaged to hourly bins. Points occurring during the gray period marked in Fig. 3.6 are shown in red open circles. Outside times of disagreement between the two MAX-DOAS instruments, shown in gray in Fig. 3.6, the correlation observed between the DOAS data and CIMS data is $R = 0.70$, which is similar to correlation of MAX-DOAS and long-path DOAS measurements observed by Frieß et al. (2011). The CIMS and LP-DOAS were previously shown to agree well, particularly during times of moderate wind speeds (3–8 m s^{-1}) and low NO (< 100 pmol mol^{-1} (Liao et al., 2011).

3.4.5 Relationship between amount observed and vertical distribution of BrO

Figure 3.4 shows the time series of the $VCD_{200\,m}$ and LT-VCD. LT-VCD values over the course of this study ranged from 0 to 8×10^{13} molecules cm^{-2} with an average of 1.46×10^{13} molecules cm^{-2} and the top quartile being above 2.0×10^{13} molecules cm^{-2}, which we will later consider to be "highly activated" events. LT-VCD retrieval errors had a mean of 3.9×10^{12} molecules cm^{-2} over the course of the campaign. Figure 3.8 shows the percentage of the LT-VCD present in the lowest 200 m ranges from shallow layer events observed primarily below 200 m to distributed column events that are also observed at higher altitudes. The third panel of Fig. 3.4 shows a time series of this ratio. Surface layer percentages over this campaign ranged between near 0 and 80 %, with the highest LT-VCD observed during distributed column events with $VCD_{200\,m}$/LT-VCD percentages of around 10 %. As the coloration in Fig. 3.8 indicates, high near-surface mixing ratios do not always imply high LT-VCD. In most cases, high LT-VCDs are associated with distributed column events.

3.4.6 Dependence on local meteorology

To examine atmospheric stability, we used meteorological balloon sounding data to calculate the temperature gradient (dT/dz) near the surface. We calculated the slope of a linear fit of the first three data points of the sounding, which typically corresponds to an altitude range from the surface to 200 m a.g.l. Because MAX-DOAS data are daylight only, to compare our BrO measurements with the sounding data, we used daily averages of the fraction of near-surface BrO to LT-VCD from each day and examined the relationship between daily averaged ratios and the corresponding temperature gradients obtained from the local daytime sounding. Figure 3.9 shows the relationship between these two quantities. This box and whisker plot is generated by splitting daily observations into three bins of about 20 days each. The median is given by the

red lines and shows the general trend that more stable atmospheres with inverted temperature structures (right bin) have more BrO present in the surface layer, while unstable atmospheres (left bin) tend to have BrO more distributed throughout the lower troposphere. Given that the temperature gradient likely varies at a higher rate than captured by daily sounding data, there is likely to be a smoothing effect that worsens the relationship between BrO vertical distribution and local stability. However, a clear relationship is still observed in Fig. 3.9.

The left panel of Fig. 3.10 illustrates the relationship between surface temperature and the amount of BrO in the near-surface layer. On average, there is a higher fraction of BrO in the near-surface layer when temperatures are below $-25\,^{\circ}\mathrm{C}$, with more distributed column BrO events being observed at higher temperatures. Figure 3.10 (right panel) shows that activation events in excess of 2×10^{13} molecules cm^{-2} occur at various temperatures.

Additionally, we examine the response of both the total activation as measured by the LT-VCD and the vertical distribution of BrO to wind speed. Figure 3.11 (left panel) shows LT-VCD values in excess of 2×10^{13} molecules cm^{-2} at various wind speeds and, as shown by the red line, there is no obvious relationship between the LT-VCD and wind speed. The observed lack of dependence of the LT-VCD on wind speed and temperature is consistent with the observations of Halfacre et al. (2014). However, the vertical distribution of BrO is influenced by wind speed. The right panel of Fig. 3.11 shows the majority of shallow layer events occur during times when wind speeds are between 3 and $6\,\mathrm{m\,s}^{-1}$. Additionally, events at wind speeds in excess of $8\,\mathrm{m\,s}^{-1}$ tend to be more distributed throughout the column.

3.5 Discussion

3.5.1 Role of atmospheric stability

The third panel of Fig. 3.4 shows the vertical structure of BrO was highly variable over the course of this study. Events range from shallow layer events where most of the observed BrO is found in the lowest 200 m to distributed column events with BrO present throughout the lower troposphere. Figure 3.8 shows the highest observed LT-VCDs were observed during distributed column events while shallow layer events, despite their enhanced near-surface mixing ratios, did not result in large amounts of total activation, as measured by the LT-VCD. This finding points out the difficulty in comparing satellite BrO column retrievals with surface observations (e.g., Sihler et al., 2012). Figure 3.9 shows the vertical distribution of BrO is clearly influenced by the observed atmospheric stability. During times of inversion, bromine activation events tend toward the shallow layer end of the spectrum. When the atmosphere is less stable, events tend to be distributed throughout the column. Given that this study only uses daily sounding data, and

knowing that convective mixing has a strong diurnal variability, it is likely this study represents a lower bound on the influence of atmospheric stability.

Ozone depletion events have been shown to be highly variable in vertical extent (e.g., Bottenheim et al., 2002; Tarasick and Bottenheim, 2002; Jones et al., 2010; Oltmans et al., 2012; Helmig et al., 2012). More recently, Moore et al. (2014) observed that opening of leads enhanced vertical mixing leading to a recovery of ozone and gaseous elemental mercury in the near-surface layer. This mixing potentially impacts the vertical distribution of halogens as well. McElroy et al. (1999) observed high total tropospheric BrO events and interpreted them as arising from convective vertical mixing associated with open leads that brought near-surface BrO to the free troposphere. Therefore, it is reasonable that vertical mixing or hindered mixing due to atmospheric stability affects the vertical structure of BrO.

Seasonal and temperature trends are consistent with atmospheric stability's influence on the BrO vertical structure. Figure 3.10 shows that at lower temperatures, which are more prevalent early in the season, events tend to be observed in shallow layers and transition to more vertically distributed as the surface temperature increases. These observations are consistent with the idea that the distribution of BrO is primarily influenced by atmospheric stability.

The right panel of Fig. 3.10 indicates that significant activation events happen at a variety of temperatures. Pöhler et al. (2010) observed there was a linear trend of decreasing near-surface maximum BrO, observed with LP-DOAS, as temperature increased up to $-15\,^{\circ}\mathrm{C}$. When examining the whole LT-VCD, rather than a near-surface concentration, this trend does not appear; however, Fig. 3.10 (left panel) shows a distinct preference toward near-surface distributions of BrO at lower temperatures which, as Fig. 3.8 shows, often contain higher near-surface amounts of BrO, but have a lower overall LT-VCD. The observation of Pöhler et al. (2010) of decreasing surface BrO mixing ratio at higher temperatures could therefore reflect increased vertical mixing of surface-sourced BrO that dilutes the surface concentration upon warming rather than being indicative of decreased halogen activation chemistry at higher temperatures. Figure 3.12 illustrates the diurnal behavior of both the LT-VCD, shown in blue, and the $\mathrm{VCD}_{200\mathrm{m}}$ shown in red. Boylan et al. (2014) observed diurnal boundary layer growth at Barrow in 2009, although this was less pronounced during times of strong inversion. The $\mathrm{VCD}_{200\mathrm{m}}$ observed in Fig. 3.12 is similar to surface concentration data observed by Pöhler et al. (2010) as well as Stutz et al. (2011). Stutz et al. (2011) suggest this pattern is indicative of snow-sourced reactive bromine diluting through a growing boundary layer. The link between atmospheric stability and the vertical distribution of BrO demonstrated in this work supports the idea that the diurnal cycling observed is due to dilution of snow-sourced reactive bromine. The MAX-DOAS observations of the present study also allow observing the BrO LT-VCD, which Fig. 3.12 shows increases to a peak in the

late afternoon, which is not fully explained by dilution of a surface source because dilution would leave the LT-VCD unchanged. This growth in LT-VCD with increased mixing was also observed in the modeling work of Toyota et al. (2014). Potential explanations for this observed growth in the LT-VCD include an enhancement of reactive bromine production in the snowpack due to increased sunlight, enhanced activation of bromine occurring aloft, potentially due to heterogeneous recycling on aerosol particles, and an increased BrO lifetime aloft.

3.5.2 Role of wind speed

Figure 3.11 (left panel) shows that activation events with BrO LT-VCDs in the top quartile occur across a spectrum of wind speeds, rather than at just the low surface wind speeds associated with stable boundary layers, or high wind speeds associated with blowing snow events. The right panel of Fig. 3.11 shows a peak in shallow layer events between 3 and $6\,\mathrm{m\,s^{-1}}$, suggesting that some ventilation of the snowpack, which has been shown to be an effective source of Br_2 (Pratt et al., 2013), is required for the release of BrO during shallow layer events. For the most part, observed wind speeds exceeding $8\,\mathrm{m\,s^{-1}}$ led to vertically distributed events; however, beyond that there is little evidence to support the need for high winds or blowing snow to sustain halogen activation aloft, consistent with the conclusions of Halfacre et al. (2014). This finding suggests that, during the course of this study, high wind events and blowing snow were not required to observe significant halogen activation. Activation events in the top quartile were observed across a range of wind speeds, particularly at more moderate wind speeds, with 66 % of highly activated events occurring at wind speeds between 3 and $8\,\mathrm{m\,s^{-1}}$. This distribution suggests that enhanced ventilation of the snowpack, and subsequent vertical mixing of snowpack-influenced air masses, is likely responsible for the majority of elevated LT-VCDs observed over the course of this study.

Jones et al. (2009) and Yang et al. (2010) rely on satellite observations of BrO rather than ground-based measurements to draw conclusions about the role of wind in halogen activation events. The differing viewing geometry could potentially affect the interpretation of the data when clouds are present, as shallow layer events occurring below clouds would potentially be masked from the satellite view but observable with ground-based MAX-DOAS. In contrast, BrO above a cloud that would be potentially observed by a satellite would not be detected by ground-based MAX-DOAS. Sihler et al. (2012) observed that satellite measurements could underestimate the amount of BrO during shallow layer events, implying events with distributed column vertical structure are more likely to be satellite detectable. This idea that shallow layer events may not be satellite detectable is also supported by the modeling work of Toyota et al. (2014). Enhanced visibility of the larger in magnitude and more vertically distributed BrO events could potentially explain why satellite remote sensing of BrO may show a relationship to wind speed. These differences

should be considered when trying to resolve differences between ground-based and satellite-based measurements.

3.5.3 Relationship between activation and aerosol particles

The near-surface aerosol particle extinction retrieved from our MAX-DOAS measurements is a proxy for suspended particulate surface area that enhances recycling of halogens, allowing us to examine the relationship between BrO and aerosol particles. The left panel of Fig. 3.13 shows an increase in the $VCD_{200\,m}$ with increased aerosol particle extinction, while the right panel shows that the relationship between aerosol particles and the LT-VCD is less clear. Laboratory studies (e.g., Huff and Abbatt, 2000; Wren et al., 2013) and field studies (e.g., Pratt et al., 2013) indicate that pH is an important control on heterogeneous recycling of halogens. Although we are unable to determine the pH of these particles by MAX-DOAS, we simply point out that not only is the presence of suspended surface area important but also that the chemical composition of that surface is likely a controlling factor.

Prior to using these data to consider the role of blowing snow in observed halogen activation during this study, it is important to point out that the lack of LT-VCD observations at high aerosol optical depth, shown in Fig. 3.3, could potentially lead to preferential exclusion of blowing snow events from further analysis of the total amount of activation as measured by the LT-VCD. To examine the potential impacts of data exclusions, we examined the amount of data at high wind speeds discarded by the application of methods described in Sect. 2.4. Of the 147 measurements occurring when wind speeds exceeded an $8\,m\,s^{-1}$ threshold used for blowing snow in Jones et al. (2009), 86 of those were rejected due to insufficient information content. If one were to presume these were all blowing snow events and belonged in the top quartile of observed activation events, they would represent 9.6 % of LT-VCD observations and 29 % of events where the LT-VCD exceeded 2×10^{13} molecules cm^{-2}. Therefore, we find that the exclusion of low-visibility data at high wind speed could only explain a small fraction of halogen activation events. While we end up discarding a significant amount of data, these filtered data still provide a fair idea of the role of high wind events, blowing snow or otherwise, in halogen activation.

While the increase in $VCD_{200\,m}$ during times of high aerosol particle extinction supports blowing snow as one source of halogens, examining the dependence of the aerosol particle extinction on wind speed, shown by the coloration in the left panel of Fig. 3.13, shows there is no apparent increase in extinction at high wind speeds, which we would expect if blowing snow was the only source of particulate surface area for halogen recycling. The observation of aerosol particle extinction values in excess of 10^{-1} km^{-1} across a variety of wind speeds suggests that

blowing snow is not the only source of the aerosol particles needed to sustain halogen activation aloft.

Additionally, it is interesting to note that LT-VCDs above 2×10^{13} molecules cm^{-2} often occur at wind speeds well below typical thresholds for blowing snow ($8\,m\,s^{-1}$; Jones et al., 2009), as shown in the left panel of Fig. 3.11. While blowing snow is not simply a univariate function of wind speed (Sturm and Stuefer, 2013), given 9 % of observations occurred when wind speeds exceeded $8\,m\,s^{-1}$ and halogen activation events in excess of 2×10^{13} molecules cm^{-2} occurred 25 % of the time, immediate activation during blowing snow events is not the sole driver of halogen activation over the course of this study and likely some other aerosol particle source is required. Frieß et al. (2011) postulated that aerosol particles produced by sublimation of blowing snow could transport and increase observed aerosol particle extinction while also providing a suspended surface for the recycling of halogens aloft. Furthermore, in the Arctic springtime, Hara et al. (2002) observed bromide loss from coarse sea salt particles and addition to fine sulfate particles, supporting the suggestion of bromine recycling on aerosol particles.

3.6 Conclusions

The methods described in this paper outline the reduction of vertical profiles retrieved from MAX-DOAS observations using optimal estimation to produce two quantities – the lower tropospheric vertical column density (LT-VCD), and the near-surface vertical column density in the lowest 200 m ($VCD_{200\,m}$) – that appropriately reflect the information content of ground-based MAX-DOAS measurements for time series analysis. Consideration of BrO averaging kernels and degrees of freedom resulting from optimal estimation validates that these quantities are most appropriate to express the 2 degrees of freedom observed. This method allows for identification of time periods when MAX-DOAS measurements contain information about BrO beyond the near-surface layer, and evaluate how the vertical structure of BrO responds to various environmental factors. Application of these methods shows retrieval of LT-VCDs by ground-based MAX-DOAS is highly dependent on visibility. During this study, we retrieved the LT-VCD 50 % of the time.

The vertical structure of BrO is highly variable, with the fraction of lower tropospheric BrO in the lowest 200 m varying from near 0 to nearly 80 %. The vertical distribution of activation events is clearly influenced by the atmospheric stability. This influence also manifests itself when examining the influence of temperature and seasonality. Later in the season, higher temperatures, and likely enhanced vertical mixing, tend to result in more BrO aloft than early in the season, where activation takes place in shallower layers. LT-VCD values in excess of 2×10^{13} molecules cm^{-2} occur across a variety of temperatures and wind speeds, but they are typically associated with distributed column events rather than shallow layer events. Events that

have larger observed near-surface mixing ratios are typically of the shallow layer variety and do not typically have large amounts of BrO spread through the lower troposphere, potentially implying less overall ozone depletion and deposition of mercury from these events. This implies that both surface and upper profile measurements are necessary to appropriately identify the impact of environmental variables on O_3 depletion and Hg oxidation rates and extent.

The observed BrO VCD_{200m} showed diurnal cycling, suggesting a surface snow source of reactive bromine diluting through an expanded boundary layer, which reflects the link between atmospheric stability and the vertical distribution of BrO. The observed growth in the LT-VCD during the day indicates the production or lifetime of reactive bromine is not static, but production increases throughout the day or losses decrease. The BrO VCD_{200m} also showed an increase during times of high aerosol particle extinction; however, the lack of a clear relationship between aerosol particle extinction and wind speed implies that blowing snow is not the sole source of aerosol particles needed for heterogeneous recycling of bromine aloft.

High wind events were not common over the course of this study. While high winds did lead to some of the highest measured columns of BrO, given the low frequency of these events, high wind events, blowing snow or otherwise, are not the sole driver of halogen activation over the course of this study, suggesting that mechanisms requiring only moderate wind speeds (e.g., wind pumping) are important for halogen activation in the Arctic.

3.7 Acknowledgements

The research at the University of Alaska was supported by the National Aeronautics and Space Administration (NASA) Cryospheric Sciences Program (CSP), and partial financial support for MAX-DOAS analysis methods was provided by the National Science Foundation under grant ARC-1023118. The Purdue group recognizes NSF support through grant ARC-1107695. K. A. Pratt was supported by a NSF Postdoctoral Fellowship in Polar Regions Research. The Purdue group acknowledges field assistance from Kyle Custard (Purdue Univ.), David Tanner (Georgia Tech), and L. Gregory Huey (Georgia Tech). The research at the Jet Propulsion Laboratory, California Institute of Technology, was supported by the NASA CSP. The authors gratefully acknowledge Chris Moore (Desert Research Inst.) for helpful discussions, as well as Alexei Rozanov from IUP Bremen for providing the SCIATRAN radiative transfer code. The authors also wish to thank UMIAQ for logistical support, and Bristow Air for providing a helicopter for the deployment of IL1.

Edited by: S. Brown

3.8 References

Abbatt, J. P. D., Thomas, J. L., Abrahamsson, K., Boxe, C., Granfors, A., Jones, A. E., King, M. D., Saiz-Lopez, A., Shepson, P. B., Sodeau, J., Toohey, D. W., Toubin, C., von Glasow, R., Wren, S. N., and Yang, X.: Halogen activation via interactions with environmental ice and snow in the polar lower troposphere and other regions, Atmos. Chem. Phys., 12, 6237–6271, doi: 10.5194/acp-12-6237-2012, 2012.

Barrie, L. A., Bottenheim, J. W., Schnell, R. C., Crutzen, P. J., and Rasmussen, R. A.: Ozone destruction and photochemical reactions at polar sunrise in the lower Arctic atmosphere, Nature, 334, 138–141, doi: 10.1038/334138a0, 1988.

Bottenheim, J. W., Fuentes, J. D., Tarasick, D. W., and Anlauf, K. G.: Ozone in the Arctic lower troposphere during winter and spring 2000 (ALERT2000), Atmos. Environ., 36, 2535–2544, doi: 10.1016/S1352-2310(02)00121-8, 2002.

Boylan, P., Helmig, D., Staebler, R., Turnipseed, A., Fairall, C., and Neff, W.: Boundary layer dynamics during the Ocean-Atmosphere-Sea-Ice-Snow (OASIS) 2009 experiment at Barrow, AK, J. Geophys. Res.-Atmos., 119, 2261–2278, doi: 10.1002/2013JD020299, 2014.

Carlson, D., Donohoue, D., Platt, U., and Simpson, W. R.: A low power automated MAX-DOAS instrument for the Arctic and other remote unmanned locations, Atmos. Meas. Tech., 3, 429–439, doi: 10.5194/amt-3-429-2010, 2010.

Chance, K.: Analysis of BrO measurements from the global ozone monitoring experiment, Geophys. Res. Lett., 25, 3335–3338, 1998.

Chance, K. V. and Spurr, R. J.: Ring effect studies: Rayleigh scattering, including molecular parameters for rotational Raman scattering, and the Fraunhofer spectrum, Appl. Optics, 36, 5224–5230, 1997.

Deutschmann, T., Beirle, S., Frieß, U., Grzegorski, M., Kern, C., Kritten, L., Platt, U., Prados-Román, C., Puķıte, J., Wagner, T., Werner, B., and Pfeilsticker, K.: The Monte Carlo atmospheric radiative transfer model McArtim: Introduction and validation of Jacobians and 3D features, J. Quant. Spectrosc. Ra., 112, 1119–1137, doi: 10.1016/j.jqsrt.2010.12.009, 2011.

Fan, S.-M., and Jacob, D. J.: Surface ozone depletion in Arctic spring sustained by bromine reactions on aerosols, Nature, 359, 522–524, doi: 10.1038/359522a0, 1992.

Fayt, C., De Smedt, I., Letocart, V., Merlaud, A., Pinardi, G., Van Roozendael, M., and Roozendael, M. V. A. N.: QDOAS Software User Manual, available at: http://uv-vis.aeronomie.be/software/QDOAS/index.php (last access: 10 March 2014), 2011.

Fickert, S., Adams, J. W., and Crowley, J. N.: Activation of Br_2 and BrCl via uptake of HOBr onto aqueous salt solutions, J. Geophys. Res., 104, 23719–23727, doi: 10.1029/1999JD900359, 1999.

Foster, K. L., Plastridge, R. A., Bottenheim, J. W., Shepson, P. B., Finlayson-Pitts, B. J., and Spicer, C. W.: The role of Br_2 and BrCl in surface ozone destruction at polar sunrise, Science, 291, 471–474, 2001.

Frieß, U.: Dynamics and chemistry of tropospheric bromine explosion events in the Antarctic coastal region, J. Geophys. Res., 109, D06305, doi: 10.1029/2003JD004133, 2004.

Frieß U., Monks, P. S., Remedios, J. J., Rozanov, A., Sinreich, R., Wagner, T., and Platt, U.: MAX-DOAS O_4 measurements: a new technique to derive information on atmospheric aerosols: 2. Modeling studies, J. Geophys. Res., 111, D14203, doi: 10.1029/2005JD006618, 2006.

Frieß U., Sihler, H., Sander, R., Pöhler, D., Yilmaz, S., and Platt, U.: The vertical distribution of BrO and aerosols in the Arctic: measurements by active and passive differential optical absorption spectroscopy, J. Geophys. Res., 116, D00R04, doi: 10.1029/2011JD015938, 2011.

Halfacre, J. W., Knepp, T. N., Shepson, P. B., Thompson, C. R., Pratt, K. A., Li, B., Peterson, P. K., Walsh, S. J., Simpson, W. R., Matrai, P. A., Bottenheim, J. W., Netcheva, S., Perovich, D. K., and Richter, A.: Temporal and spatial characteristics of ozone depletion events from measurements in the Arctic, Atmos. Chem. Phys., 14, 4875–4894, doi: 10.5194/acp-14-4875-2014, 2014.

Hara, K., Osada, K., Matsunaga, K., Iwasaka, Y., Shibata, T., and Furuya, K.: Atmospheric inorganic chlorine and bromine species in Arctic boundary layer of the winter/spring, J. Geophys. Res., 107, 4361, doi: 10.1029/2001JD001008, 2002.

Helmig, D., Boylan, P., Johnson, B., Oltmans, S., Fairall, C., Staebler, R., Weinheimer, A., Orlando, J., Knapp, D. J., Montzka, D. D., Flocke, F., Frieß, U., Sihler, H., and Shepson, P. B.: Ozone dynamics and snow-atmosphere exchanges during ozone depletion events at Barrow, Alaska, J. Geophys. Res.-Atmos., 117, D20303, doi: 10.1029/2012JD017531, 2012.

Hermans, C., Vandaele, A., Coquart, B., Jenouvrier, A., Merienne, M. F., Fally, S., Carleer, M., and Colin, R.: Absorption bands of O_2 and its collision-induced bands in the 30 000–7500 cm^{-1} wavenumber region, in: IRS 2000: Current Problems in Atmospheric Radiation, edited by: Smith, W. L. and Timofeyev, Y. M., Hampton, VA, Deepak, 639–642, 2001.

Hönninger, G., von Friedeburg, C., and Platt, U.: Multi axis differential optical absorption spectroscopy (MAX-DOAS), Atmos. Chem. Phys., 4, 231–254, doi: 10.5194/acp-4-231-2004, 2004.

Huff, A. K. and Abbatt, J. P. D.: Gas-phase Br_2 production in heterogeneous reactions of Cl_2, HOCl, and BrCl with halide-ice surfaces, J. Phys. Chem. A, 104, 7284–7293, doi: 10.1021/jp001155w, 2000.

Jones, A. E., Anderson, P. S., Begoin, M., Brough, N., Hutterli, M. A., Marshall, G. J., Richter, A., Roscoe, H. K., and Wolff, E. W.: BrO, blizzards, and drivers of polar tropospheric ozone depletion events, Atmos. Chem. Phys., 9, 4639–4652, doi: 10.5194/acp-9-4639-2009, 2009.

Jones, A. E., Anderson, P. S., Wolff, E. W., Roscoe, H. K., Marshall, G. J., Richter, A., Brough, N., and Colwell, S. R.: Vertical structure of Antarctic tropospheric ozone depletion events: characteristics and broader implications, Atmos. Chem. Phys., 10, 7775–7794, doi: 10.5194/acp-10-7775-2010, 2010.

Koo, J.-H., Wang, Y., Kurosu, T. P., Chance, K., Rozanov, A., Richter, A., Oltmans, S. J., Thompson, A. M., Hair, J. W., Fenn, M. A., Weinheimer, A. J., Ryerson, T. B., Solberg, S., Huey, L. G., Liao, J., Dibb, J. E., Neuman, J. A., Nowak, J. B., Pierce, R. B., Natarajan, M., and Al-Saadi, J.: Characteristics of tropospheric ozone depletion events in the Arctic spring: analysis of the ARCTAS, ARCPAC, and ARCIONS measurements and satellite BrO observations, Atmos. Chem. Phys., 12, 9909–9922, doi: 10.5194/acp-12-9909-2012, 2012.

Krnavek, L., Simpson, W. R., Carlson, D., Domine, F., Douglas, T. A., and Sturm, M.: The chemical composition of surface snow in the Arctic: examining marine, terrestrial, and atmospheric influences, Atmos. Environ., 50, 349–359, doi: 10.1016/j.atmosenv.2011.11.033, 2012.

Lehrer, E., Hönninger, G., and Platt, U.: A one dimensional model study of the mechanism of halogen liberation and vertical transport in the polar troposphere, Atmos. Chem. Phys., 4, 2427–2440, doi: 10.5194/acp-4-2427-2004, 2004.

Liao, J., Sihler, H., Huey, L. G., Neuman, J. A., Tanner, D. J., Friess, U., Platt, U., Flocke, F. M., Orlando, J. J., Shepson, P. B., Beine, H. J., Weinheimer, A. J., Sjostedt, S. J., Nowak, J. B., Knapp, D. J., Staebler, R. M., Zheng, W., Sander, R., Hall, S. R., and Ullmann, K.: A comparison of Arctic BrO measurements by chemical ionization mass spectrometry and long path-differential optical absorption spectroscopy, J. Geophys. Res., 116, 1–14, doi: 10.1029/2010JD014788, 2011.

Liao, J., Huey, L. G., Tanner, D. J., Flocke, F. M., Orlando, J. J., Neuman, J. A., Nowak, J. B., Weinheimer, A. J., Hall, S. R., Smith, J. N., Fried, A., Staebler, R. M., Wang, Y., Koo, J.-H., Cantrell, C. A., Weibring, P., Walega, J., Knapp, D. J., Shepson, P. B., and Stephens, C. R.: Observations of inorganic bromine (HOBr, BrO, and Br_2) speciation at Barrow, Alaska, in spring 2009, J. Geophys. Res., 117, D00R16, doi: 10.1029/2011JD016641, 2012.

Liao, J., Huey, L. G., Liu, Z., Tanner, D. J., Cantrell, C. A., Orlando, J. J., Flocke, F. M., Shepson, P. B., Weinheimer, A. J., Hall, S. R., Ullmann, K., Beine, H. J., Wang, Y., Ingall, E. D., Stephens, C. R., Hornbrook, R. S., Apel, E. C., Riemer, D., Fried, A., Mauldin III, R. L., Smith, J. N., Staebler, R. M., Neuman, J. A., and Nowak, J. B.: High levels of molecular chlorine in the Arctic atmosphere, Nat. Geosci., 7, 91–94, doi: 10.1038/ngeo2046, 2014.

Malicet, J., Daumont, D., Charbonnier, J., Parisse, C., Chakir, A., and Brion, J.: Ozone UV spectroscopy. II. Absorption cross-sections and temperature dependence, J. Atmos. Chem., 21, 263–273, doi: 10.1007/BF00696758, 1995.

McConnell, J. C., Henderson, G. S., Barrie, L., Bottenheim, J., Niki, H., Langford, C. H., and Templeton, E. M. J.: Photochemical bromine production implicated in Arctic boundary-layer ozone depletion, Nature, 355, 150–152, doi: 10.1038/355150a0, 1992.

McElroy, C. T., McLinden, C. A., and McConnell, J. C.: Evidence for bromine monoxide in the free troposphere during the arctic polar sunrise, Nature, 397, 338–341, 1999.

Moore, C. W., Obrist, D., Steffen, A., Staebler, R. M., Douglas, T. A., Richter, A., and Nghiem, S. V.: Convective forcing of mercury and ozone in the Arctic boundary layer induced by leads in sea ice., Nature, 506, 81–84, doi: 10.1038/nature12924, 2014.

Mozurkewich, M.: Mechanisms for the release of halogens from sea-salt particles by free radical reactions, J. Geophys. Res., 100, 14199–14207, 1995.

Neuman, J. A., Nowak, J. B., Huey, L. G., Burkholder, J. B., Dibb, J. E., Holloway, J. S., Liao, J., Peischl, J., Roberts, J. M., Ryerson, T. B., Scheuer, E., Stark, H., Stickel, R. E., Tanner, D. J., and Weinheimer, A.: Bromine measurements in ozone depleted air over the Arctic Ocean, Atmos. Chem. Phys., 10, 6503–6514, doi: 10.5194/acp-10-6503-2010, 2010.

Nghiem, S. V., Clemente-Colón, P., Douglas, T., Moore, C., Obrist, D., Perovich, D. K., Pratt, K. A., Rigor, I. G., Simpson, W., Shepson, P. B., Steffen, A., and Woods, J.: Studying bromine, ozone, and mercury chemistry in the Arctic, EOS T. Am. Geophys. Un., 94, 289–291, doi: 10.1002/2013EO330002, 2013.

Oltmans, S. J., Johnson, B. J., and Harris, J. M.: Springtime boundary layer ozone depletion at Barrow, Alaska: meteorological influence, year-to-year variation, and long-term change, J. Geophys. Res., 117, D00R18, doi: 10.1029/2011JD016889, 2012.

Parrella, J. P., Jacob, D. J., Liang, Q., Zhang, Y., Mickley, L. J., Miller, B., Evans, M. J., Yang, X., Pyle, J. A., Theys, N., and Van Roozendael, M.: Tropospheric bromine chemistry: implications for present and pre-industrial ozone and mercury, Atmos. Chem. Phys., 12, 6723–6740, doi: 10.5194/acp-12-6723-2012, 2012.

Payne, V. H., Clough, S. A., Shephard, M. W., Nassar, R., and Logan, J. A.: Information-centered representation of retrievals with limited degrees of freedom for signal: application to methane from the tropospheric emission spectrometer, J. Geophys. Res., 114, D10307, doi: 10.1029/2008JD010155, 2009.

Piot, M. and von Glasow, R.: The potential importance of frost flowers, recycling on snow, and open leads for ozone depletion events, Atmos. Chem. Phys., 8, 2437–2467, doi: 10.5194/acp-8-2437-2008, 2008.

Platt, U., and Hönninger, G.: The role of halogen species in the troposphere, Chemosphere, 52, 325–338, doi: 10.1016/S0045-6535(03)00216-9, 2003.

Pöhler, D., Vogel, L., Friess, U., and Platt, U.: Observation of halogen species in the Amundsen Gulf, Arctic, by active long-path differential optical absorption spectroscopy, P. Natl. Acad. Sci. USA, 107, 6582–6587, doi: 10.1073/pnas.0912231107, 2010.

Pratt, K. A., Custard, K. D., Shepson, P. B., Douglas, T. A., Pöhler, D., General, S., Zielcke, J., Simpson, W. R., Platt, U., Tanner, D. J., Gregory Huey, L., Carlsen, M., and Stirm, B. H.: Photochemical production of molecular bromine in Arctic surface snowpacks, Nat. Geosci., 6, 351–356, doi: 10.1038/ngeo1779, 2013.

Richter, A., Wittrock, F., Eisinger, M., and Burrows, J. P.: GOME observations of tropospheric BrO in Northern Hemispheric spring and summer 1997, Geophys. Res. Lett., 25, 2683–2686, 1998.

Rodgers, C. D.: Inverse Methods For Atmospheric Sounding: Theory and Practice, World Scientific, Singapore, ISBN:978-981-02-2740-1 , 2000.

Rozanov, A., Bovensmann, H., Bracher, A., Hrechanyy, S., Rozanov, V., Sinnhuber, M., Stroh, F., and Burrows, J.: NO_2 and BrO vertical profile retrieval from SCIAMACHY limb measurements: sensitivity studies, Adv. Space Res., 36, 846–854, doi: 10.1016/j.asr.2005.03.013, 2005.

Saiz-Lopez, A. and von Glasow, R.: Reactive halogen chemistry in the troposphere, Chem. Soc. Rev., 41, 6448–6472, 2012.

Salawitch, R. J., Canty, T., Kurosu, T., Chance, K., Liang, Q., da Silva, A., Pawson, S., Nielsen, J. E., Rodriguez, J. M., Bhartia, P. K., Liu, X., Huey, L. G., Liao, J., Stickel, R. E., Tanner, D. J., Dibb, J. E., Simpson, W. R., Donohoue, D., Weinheimer, A., Flocke, F., Knapp, D., Montzka, D., Neuman, J. A., Nowak, J. B., Ryerson, T. B., Oltmans, S., Blake, D. R., Atlas, E. L., Kinnison, D. E., Tilmes, S., Pan, L. L., Hendrick, F., Van Roozendael, M., Kreher, K., Johnston, P. V., Gao, R. S., Johnson, B., Bui, T. P., Chen, G., Pierce, R. B., Crawford, J. H., and Jacob, D. J.: A new interpretation of total column BrO during Arctic spring, Geophys. Res. Lett., 37, L21805, doi: 10.1029/2010GL043798, 2010.

Schroeder, W., Anlauf, K., Barrie, L., and Lu, J.: Arctic springtime depletion of mercury, Nature, 16–17, 394, doi: 10.1038/28530, 1998.

Sihler, H., Platt, U., Beirle, S., Marbach, T., Kühl, S., Dörner, S., Verschaeve, J., Frieß, U., Pöhler, D., Vogel, L., Sander, R., and Wagner, T.: Tropospheric BrO column densities in the Arctic derived from satellite: retrieval and comparison to ground-based measurements, Atmos. Meas. Tech., 5, 2779–2807, doi: 10.5194/amt-5-2779-2012, 2012.

Simpson, W. R., Carlson, D., Hönninger, G., Douglas, T. A., Sturm, M., Perovich, D., and Platt, U.: First-year sea-ice contact predicts bromine monoxide (BrO) levels at Barrow, Alaska better than potential frost flower contact, Atmos. Chem. Phys., 7, 621–627, doi: 10.5194/acp-7-621-2007, 2007a.

Simpson, W. R., von Glasow, R., Riedel, K., Anderson, P., Ariya, P., Bottenheim, J., Burrows, J., Carpenter, L. J., Frieß, U., Goodsite, M. E., Heard, D., Hutterli, M., Jacobi, H.-W., Kaleschke, L., Neff, B., Plane, J., Platt, U., Richter, A., Roscoe, H., Sander, R., Shepson, P., Sodeau, J., Steffen, A., Wagner, T., and Wolff, E.: Halogens and their role in polar boundary-layer ozone depletion, Atmos. Chem. Phys., 7, 4375-4418, doi: 10.5194/acp-7-4375-2007, 2007b.

Spicer, C. W., Plastridge, R. A., Foster, K. L., Finlayson-Pitts, B. J., Bottenheim, J. W., Grannas, A. M., and Shepson, P. B.: Molecular halogens before and during ozone depletion events in the Arctic at polar sunrise: concentrations and sources, Atmos. Environ., 36, 2721–2731, doi: 10.1016/S1352-2310(02)00125-5, 2002.

Steffen, A., Douglas, T., Amyot, M., Ariya, P., Aspmo, K., Berg, T., Bottenheim, J., Brooks, S., Cobbett, F., Dastoor, A., Dommergue, A., Ebinghaus, R., Ferrari, C., Gardfeldt, K., Goodsite, M. E., Lean, D., Poulain, A. J., Scherz, C., Skov, H., Sommar, J., and Temme, C.: A synthesis of atmospheric mercury depletion event chemistry in the atmosphere and snow, Atmos. Chem. Phys., 8, 1445–1482, doi: 10.5194/acp-8-1445-2008, 2008.

Sturm, M. and Stuefer, S.: Wind-blown flux rates derived from drifts at arctic snow fences, J. Glaciol., 59, 21–34, doi: 10.3189/2013JoG12J110, 2013.

Stutz, J., Thomas, J. L., Hurlock, S. C., Schneider, M., von Glasow, R., Piot, M., Gorham, K., Burkhart, J. F., Ziemba, L., Dibb, J. E., and Lefer, B. L.: Longpath DOAS observations of surface BrO at Summit, Greenland, Atmos. Chem. Phys., 11, 9899–9910, doi: 10.5194/acp-11-9899-2011, 2011.

Tackett, P. J., Cavender, A. E., Keil, A. D., Shepson, P. B., Bottenheim, J. W., Morin, S., Deary, J., Steffen, A., and Doerge, C.: A study of the vertical scale of halogen chemistry in the Arctic troposphere during Polar Sunrise at Barrow, Alaska, J. Geophys. Res., 112, D07306, doi: 10.1029/2006JD007785, 2007.

Tarasick, D. W. and Bottenheim, J. W.: Surface ozone depletion episodes in the Arctic and Antarctic from historical ozonesonde records, Atmos. Chem. Phys., 2, 197–205, doi: 10.5194/acp-2-197-2002, 2002.

Theys, N., Van Roozendael, M., Errera, Q., Hendrick, F., Daerden, F., Chabrillat, S., Dorf, M., Pfeilsticker, K., Rozanov, A., Lotz, W., Burrows, J. P., Lambert, J.-C., Goutail, F., Roscoe, H. K., and De Mazière, M.: A global stratospheric bromine monoxide climatology based on the BASCOE chemical transport model, Atmos. Chem. Phys., 9, 831–848, doi: 10.5194/acp-9-831-2009, 2009.

Theys, N., Van Roozendael, M., Hendrick, F., Yang, X., De Smedt, I., Richter, A., Begoin, M., Errera, Q., Johnston, P. V., Kreher, K., and De Mazière, M.: Global observations of tropospheric BrO columns using GOME-2 satellite data, Atmos. Chem. Phys., 11, 1791–1811, doi: 10.5194/acp-11-1791-2011, 2011.

Toom-Sauntry, D. and Barrie, L. A.: Chemical composition of snowfall in the high Arctic: 1990–1994, Atmos. Environ., 36, 2683–2693, 2002.

Toyota, K., McConnell, J. C., Staebler, R. M., and Dastoor, A. P.: Air-snowpack exchange of bromine, ozone and mercury in the springtime Arctic simulated by the 1-D model PHANTAS – Part 1: In-snow bromine activation and its impact on ozone, Atmos. Chem. Phys., 14, 4101–4133, doi: 10.5194/acp-14-4101-2014, 2014.

Tuckermann, M., R., A., Golz, C., Lorenzen-Schmidt, H., Senne, T., Stutz, J., Trost, B., Unold, W., and Platt, U.: DOAS-observation of halogen radical-catalysed arctic boundary layer ozone destruction during the ARCTOC-campaigns 1995 and 1996 in Ny-Alesund, Spitsbergen, Tellus B, 49, 533–555, doi: 10.1034/j.1600-0889.49.issue5.9.x, 1997.

Vandaele, A., Hermans, C., Simon, P., Carleer, M., Colin, R., Fally, S., Mérienne, M., Jenouvrier, A., and Coquart, B.: Measurements of the NO_2 absorption cross-section from 42 000 cm^{-1} to 10 000 cm^{-1} (238–1000 nm) at 220 K and 294 K, J. Quant. Spectrosc. Ra., 59, 171–184, doi: 10.1016/S0022-4073(97)00168-4, 1998.

von Clarmann, T. and Grabowski, U.: Elimination of hidden a priori information from remotely sensed profile data, Atmos. Chem. Phys., 7, 397–408, doi: 10.5194/acp-7-397-2007, 2007.

Wagner, T. and Platt, U.: Satellite mapping of enhanced BrO concentrations in the troposphere, Nature, 395, 486–490, 1998.

Wilmouth, D. M., Hanisco, T. F., Donahue, N. M., and Anderson, J. G.: Fourier transform ultraviolet spectroscopy of the $A^2\Pi_{3/2} \leftarrow X^2\Pi_{3/2}$ transition of BrO, J. Phys. Chem. A, 103, 8935–8945, doi: 10.1021/jp991651o, 1999.

Wren, S. N., Donaldson, D. J., and Abbatt, J. P. D.: Photochemical chlorine and bromine activation from artificial saline snow, Atmos. Chem. Phys., 13, 9789–9800, doi: 10.5194/acp-13-9789-2013, 2013.

Yang, X., Pyle, J. A., Cox, R. A., Theys, N., and Van Roozendael, M.: Snow-sourced bromine and its implications for polar tropospheric ozone, Atmos. Chem. Phys., 10, 7763–7773, doi: 10.5194/acp-10-7763-2010, 2010.

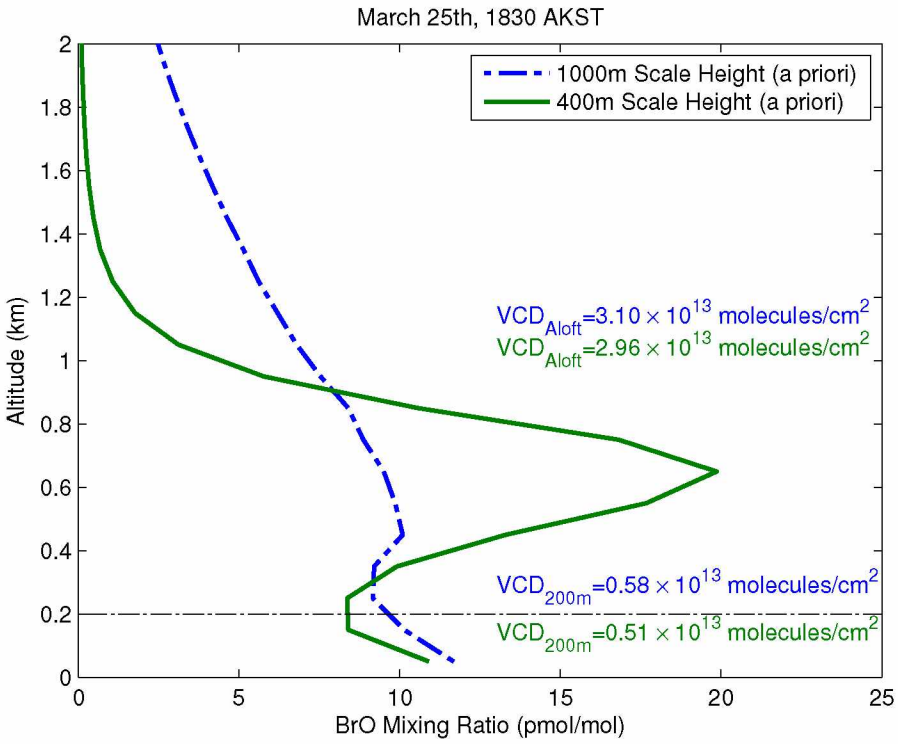

Figure 3.1: A sample profile retrieval of BrO at the BARC building. The blue line represents the profile retrieved using an a priori profile that exponentially decays with a scale height of 1000 m, while the green represents quantities retrieved using an a priori profile that exponentially decays with a scale height of 400 m (a priori used for this study). The dashed lines indicate layer boundaries determined from the ensemble of retrievals over the course of this study. The partial VCD values noted on the figure correspond to layer selections used in this study. The $VCD_{200\,m}$ is the integral of the retrieved profile from 0–200 m and the VCD_{Aloft} is integrated from 200 to 2000 m.

Table 3.1: Absorber cross sections used in the MAX-DOAS fitting.

Species	Cross Section
BrO (223K)	Wilmouth et al. (1999)
O_3 (243K)	Malicet et al. (1995)
NO_2 (220K)	Vandaele et al. (1998)
O_4	Hermans et al. (2001)
Ring	Determined from zenith spectra using Chance and Spurr (1997)

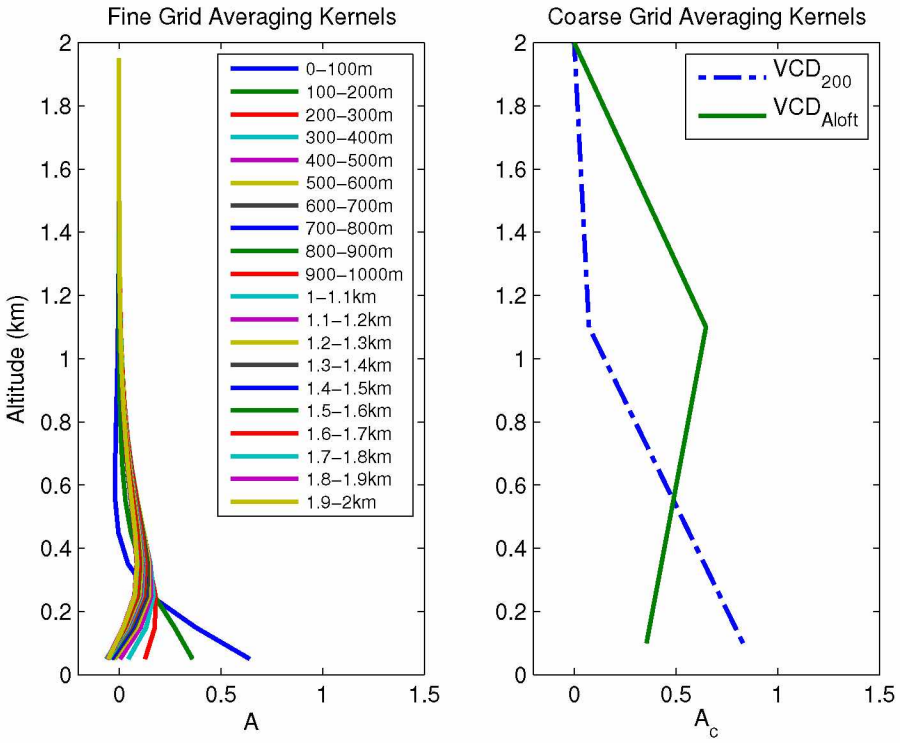

Figure 3.2: An illustration of the grid coarsening of the BrO averaging kernels. These averaging kernels correspond to the retrieval shown in green on Fig. 3.1. Averaging kernels for the original retrieval (left) and for the coarse grid (right).

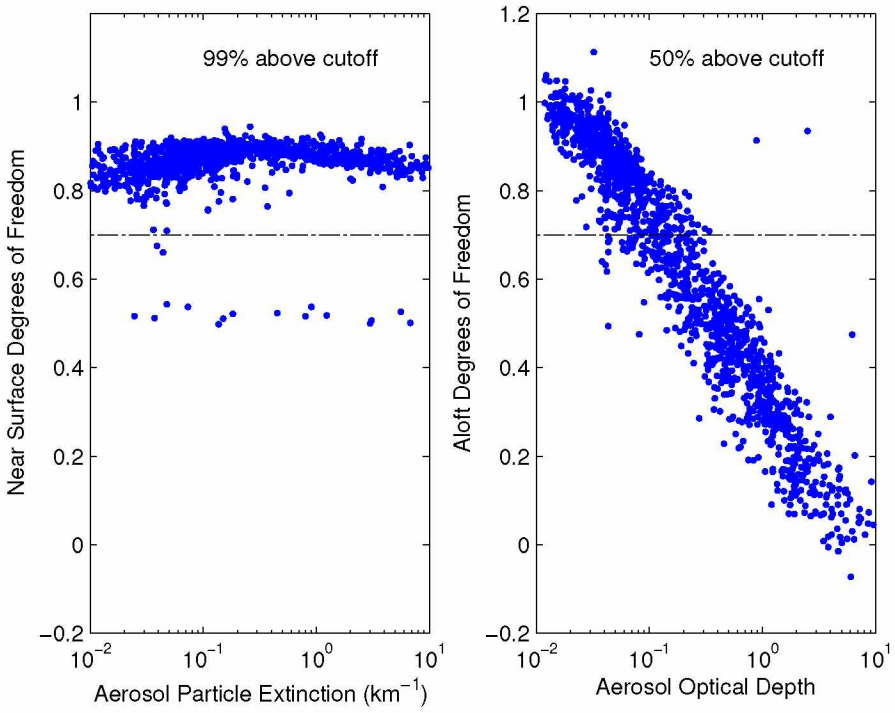

Figure 3.3: The left panel shows the degrees of freedom associated with the VCD_{200m} as a function of near-surface aerosol particle extinction. The right panel shows the degrees of freedom associated with the $VCD_{Residual}$ as a function of the aerosol optical depth. The dashed line illustrates the cutoff we have chosen for sufficient information content.

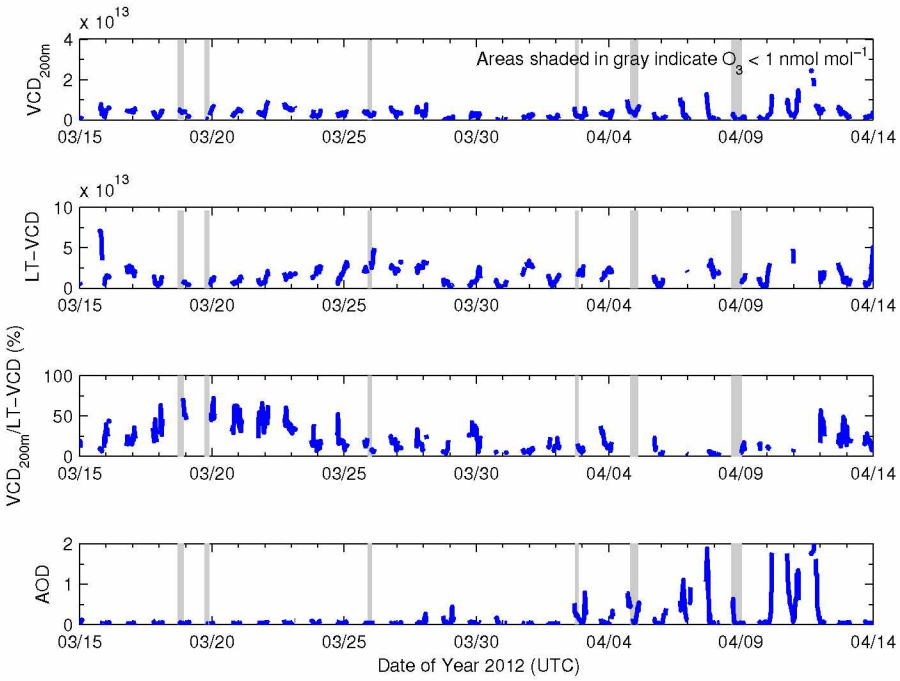

Figure 3.4: A portion of the timeseries of BrO observed during this study. The top panel represents the VCD_{200}, the second panel represents the LT-VCD, both of which have units of molecules cm^{-2}. The third panel shows the percentage of the LT-VCD observed in the lowest 200 m, while the bottom panel shows the aerosol optical depth over the course of this study. In the third panel, ratios are not calculated for events that have a LT-VCD below 5×10^{12} molecules cm^{-2}. Shaded areas represent potentially titrated air masses near the surface (Ozone < 1 nmol mol^{-1}). The full timeseries can be found in the Supplement.

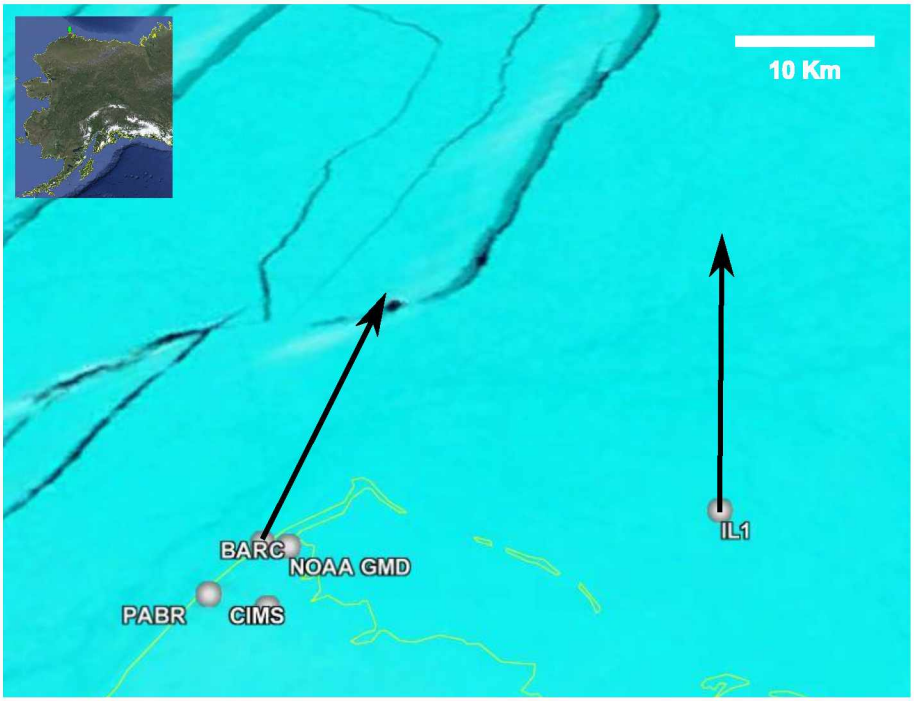

Figure 3.5: Field locations during the BROMEX field campaign overlain on Moderate Resolution Imaging Spectrometer data from the Aqua satellite (7,2,1 bands). This ice cover image is from March 13th, 2012. These locations are Barrow Arctic Research Center (BARC), Chemical Ionization Mass Spectrometry (CIMS), NOAA Global Monitoring Division (NOAA GMD) station, IceLander 1 (IL1) buoy, and Barrow Airport (PABR), nearby where most of Barrow's population resides. The distance between BARC and IL1 is about 36 km. Viewing azimuths for each DOAS instrument are indicated with black arrows. The inset map of Alaska shows the study location marked in green.

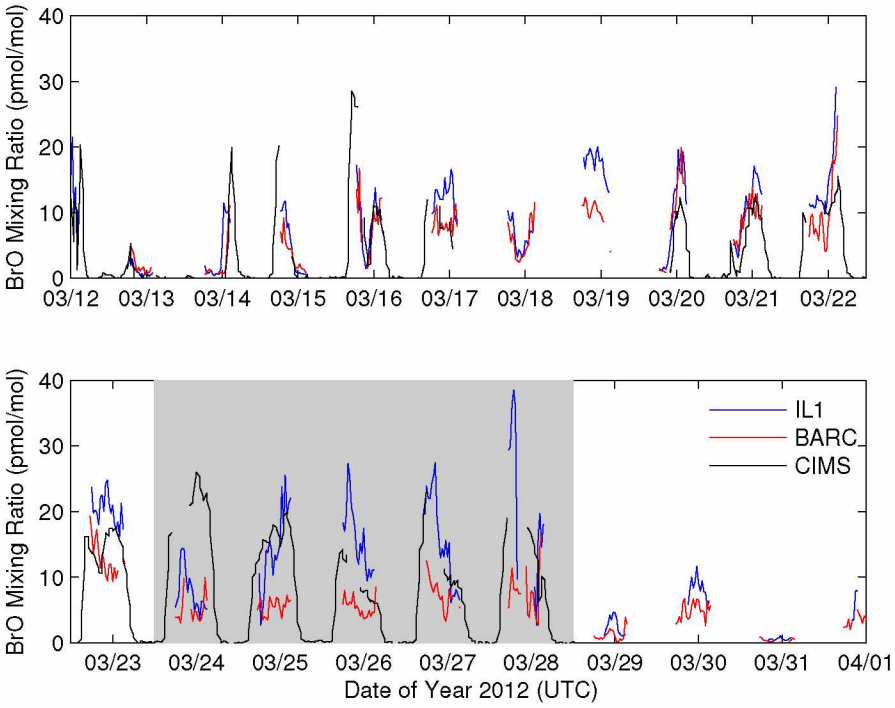

Figure 3.6: A timeseries of 30 min averaged BrO measured using CIMS, compared with average BrO in the lowest 100 m measured by MAX-DOAS at two different sites. The grey area indicates times when there were significant differences in BrO observed between MAX-DOAS sites at the BARC Building and on land fast ice 36 km NE of the BARC building (IL1).

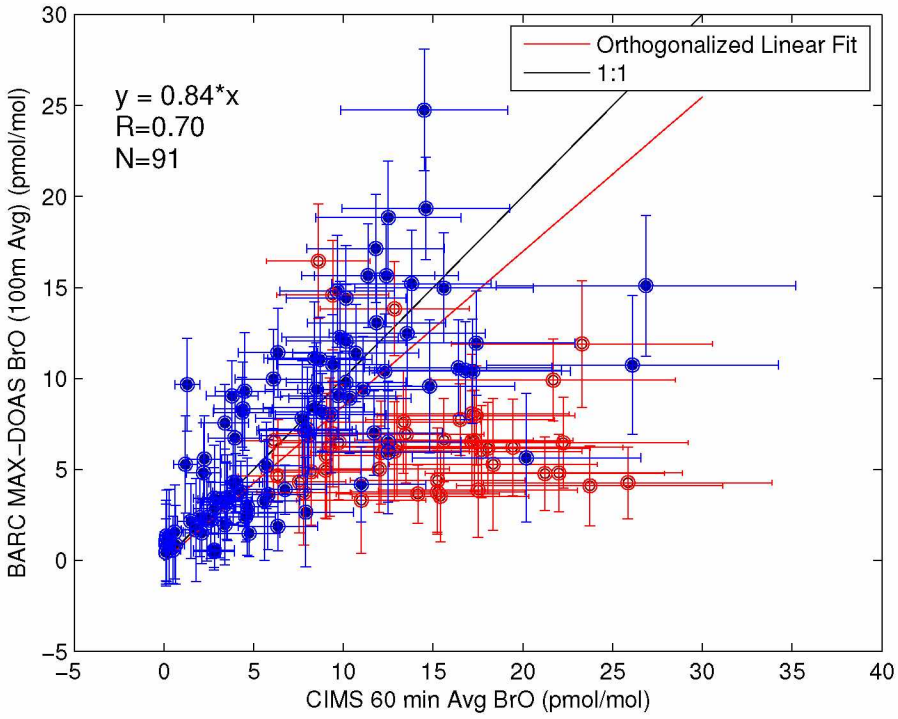

Figure 3.7: The correlation of 60 min averaged CIMS BrO with BrO retrieved in the lowest 100 m using MAX-DOAS. Red circles indicate times when we observed a chemical gradient between field sites, which are excluded from this correlation.

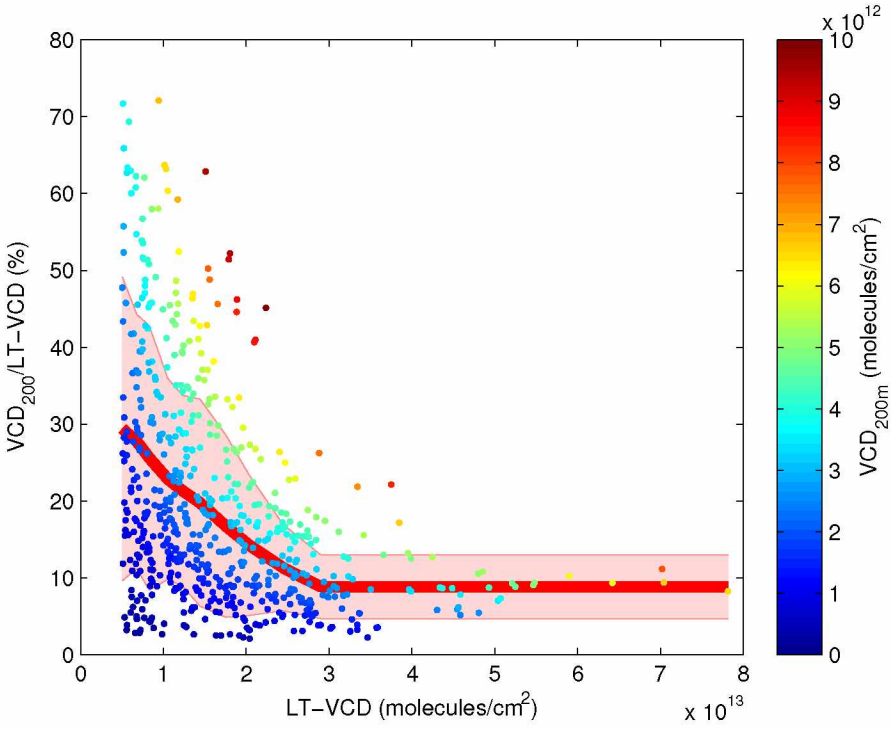

Figure 3.8: The relationship between the total BrO activation, as measured by the LT-VCD, and the vertical structure of the activation event. The red line represents the mean percentage of BrO in the lowest 200 m as a function of the LT-VCD, calculated from deciles on the x axis, while the shaded region represents one standard deviation. The coloration indicates the $\mathrm{VCD}_{200\,\mathrm{m}}$. In this plot LT-VCD values below 5×10^{12} molecules cm^{-2} are eliminated to avoid calculating percentages from near zero amounts of BrO.

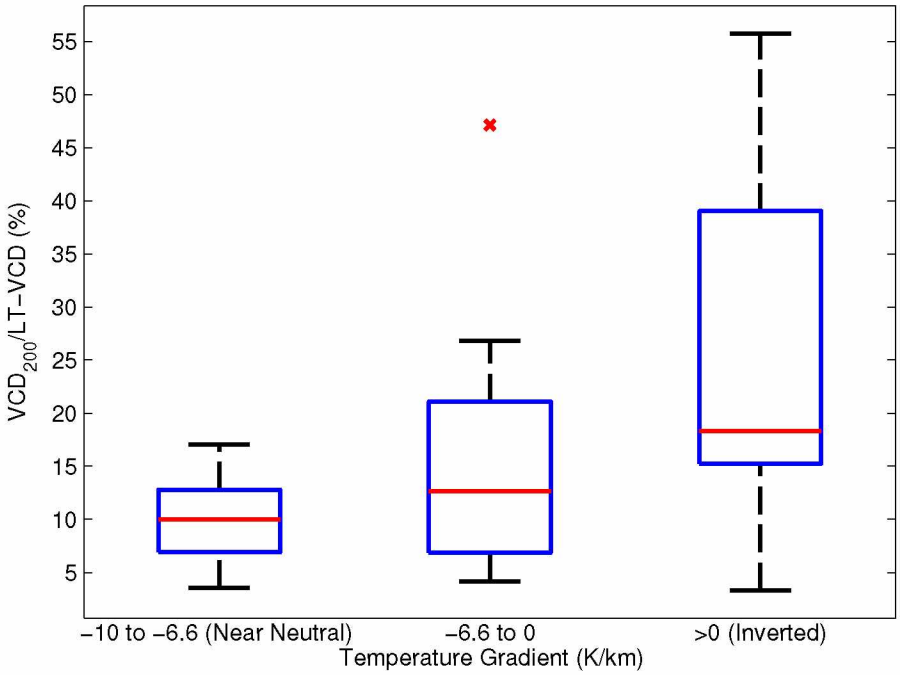

Figure 3.9: The relationship between daily estimated temperature gradients vs. the average percentage of BrO observed in the near surface layer during that day is shown here using a box and whisker plot. The data are split such that each bin comprises ≈ 20 days worth of data. The red lines show the median value for each bin, while the blue box encloses the 25–75th percentile and the whiskers show the full range of data excluding outliers ($\times$). Outliers are points that are outside 3σ for the corresponding group.

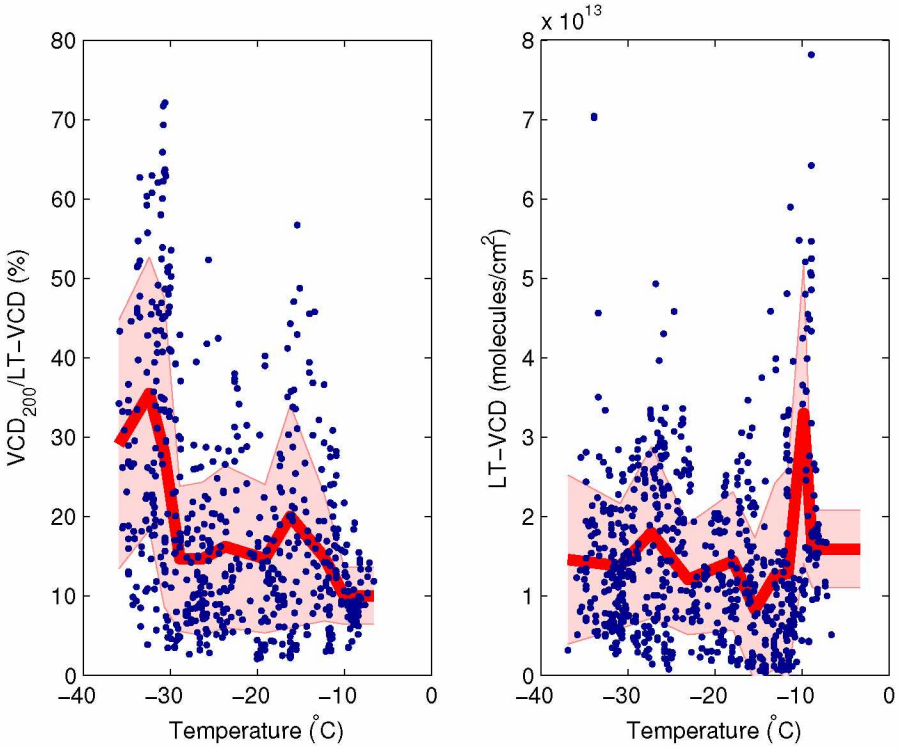

Figure 3.10: The relationship between BrO and temperature. The left panel shows the percentage of BrO in the lowest 200 m vs. the near-surface temperature, while the right panel shows the LT-VCD vs. the near-surface temperature. The red line represents the mean, calculated from deciles on the x axis, while the shaded region represents one standard deviation. In the left panel, LT-VCD values below 5×10^{12} molecules cm^{-2} are eliminated to avoid calculating percentages from near zero amounts of BrO.

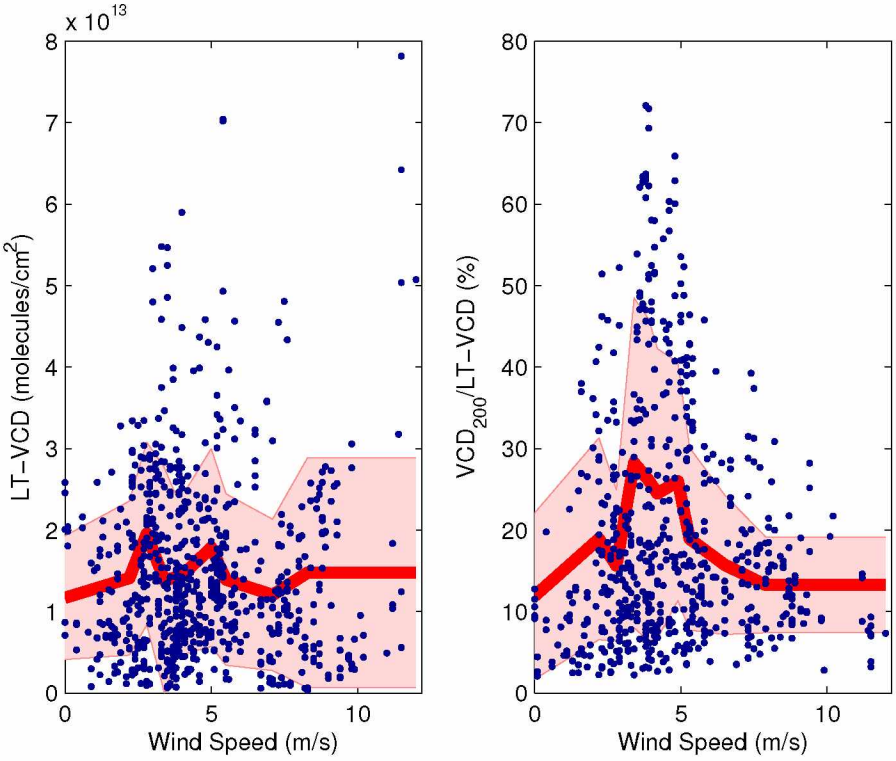

Figure 3.11: The left panel shows the relationship between the BrO LT-VCD and wind speed, while the right panel shows percentage of BrO in the lowest 200 m vs. the wind speed. In both cases, the red line represents the mean as a function of wind speed, calculated from deciles on the x axis, while the shaded region represents one standard deviation.

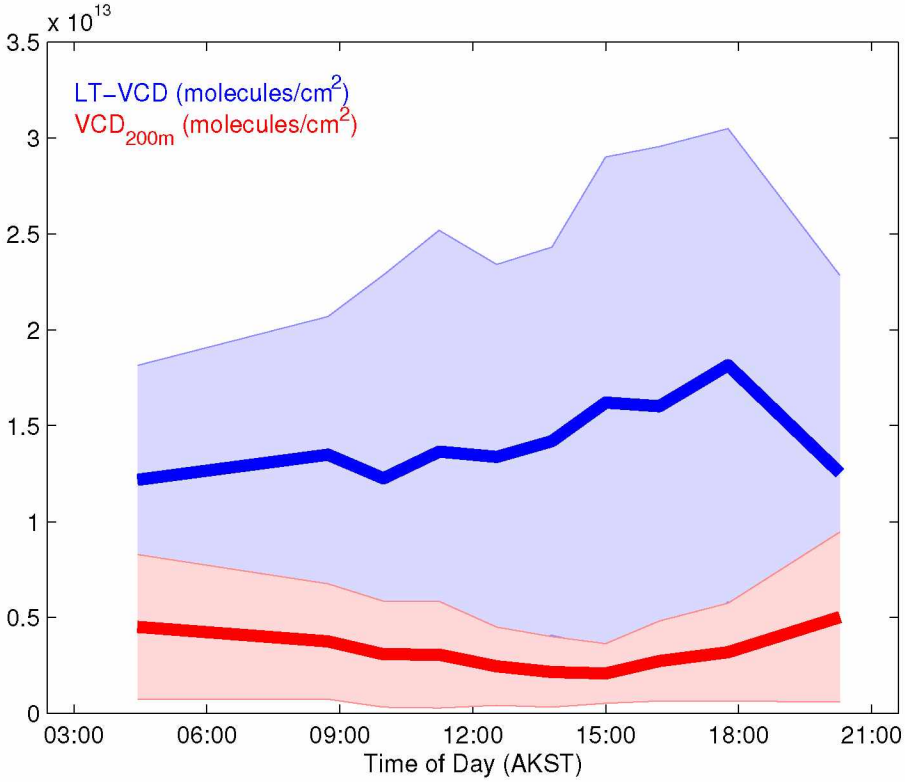

Figure 3.12: The diurnal cycling of the BrO LT-VCD (blue) and $VCD_{200\,m}$ (red). The solid lines represents the mean VCD as a function of time of day, while the shaded region represents one standard deviation. The shaded regions are symmetric about the mean in both cases, however the cycling of the $VCD_{200\,m}$ is overlain on the cycling of the LT-VCD, partially obscuring the standard deviation of the LT-VCD.

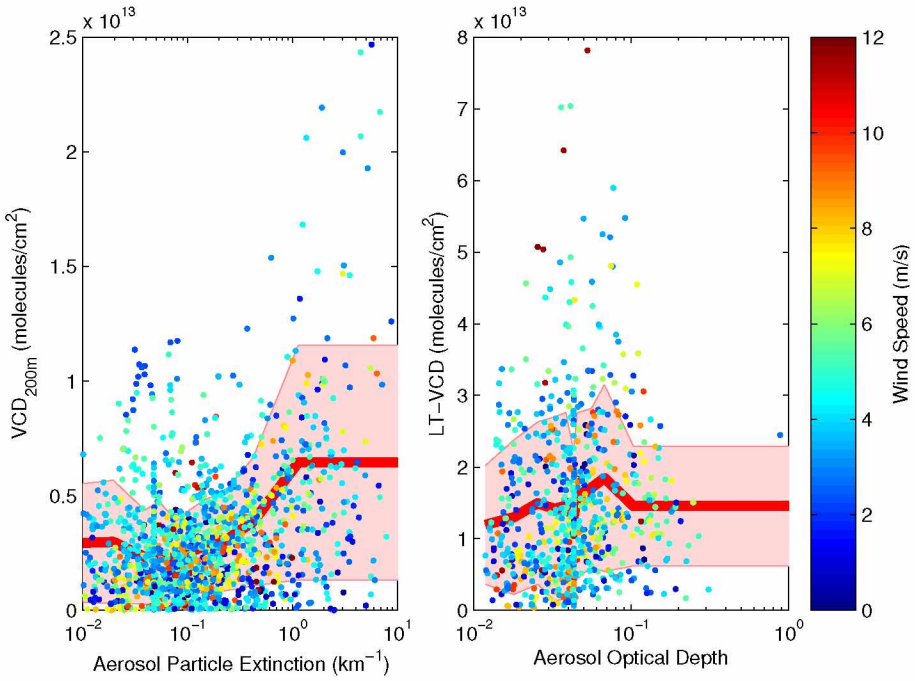

Figure 3.13: The left panel shows the relationship between the BrO $VCD_{200\,m}$ and the near-surface aerosol particle extinction. The right panel shows the relationship between the BrO LT-VCD and the aerosol optical depth. In both plots the x axis is a log scale. The red line represents the mean VCD, calculated from deciles on the x axis, while the shaded region represents one standard deviation. In both cases, the coloration indicates the wind speed.

Chapter 4

Interannual Variability of Observed Bromine Monoxide Over a Four Year Period at Barrow, Alaska[1]

4.1 Abstract

Multiple axis differential absorption spectroscopy (MAX-DOAS) measured bromine monoxide (BrO) in March through May of 2008, 2009, 2012, and 2013 at Barrow, Alaska, as well as at ice-tethered buoys in the Arctic Ocean in 2011 and 2012. For each season of Barrow measurements, we examined the air mass histories using back trajectory modeling and ice coverage maps generated from satellite-based-instrument scatterometery. Over the course of this study, the short term (half-hourly averaged) linear correlation (R=0.38) observed between time in first year sea ice (FYI) areas and observed BrO lower tropospheric vertical column densities (LT-VCD) is weak. These data show evidence of a non-linear increase of LT-VCD BrO with low average activation in the absence of ice contact increasing and apparently saturating at longer (multi-day) ice contact. Annual averages of BrO and time in FYI areas are highly correlated (R=0.93), indicating that the inter-annual variability of BrO at coastal sites is driven by air mass history rather than pan-Arctic sea ice trends. We find no relationship between BrO and potential frost flower contact over this time period. We compared BrO LT-VCDs at Barrow to measurements from drifting buoys to examine differences in halogen activation events between coastal and on-ice locations. A comparison of these two data sets show a wide range of BrO LT-VCDs are observed at on-ice locations, implying that while an air mass spending time in FYI areas may be required to observe halogen activation, it does not by itself imply halogen chemistry is occurring, and the influence of FYI on the overall level of activation is likely non-linear.

4.2 Introduction

The return of sunlight to the polar regions has shown to alter the oxidative chemistry of the polar atmosphere through the release of halogen radicals (e.g. Br, Cl, I). These halogens have been implicated in the depletion of boundary layer ozone (*Barrie et al.*, 1988; *Simpson et al.*, 2007a) and enhanced deposition of gaseous elemental mercury in the polar spring (*Schroeder et al.*, 1998; *Steffen et al.*, 2008). Because this chemistry is known to occur on saline ice surfaces, first year ice (FYI), which tends to be more saline than multi-year ice (*Perovich and Richter-Menge*, 1994) has been implicated in halogen activation chemistry (*Simpson et al.*, 2007b).

[1]P. K. Peterson, W. R. Simpson, and S. V. Nghiem, Interannual Variability of Observed Bromine Monoxide Over a Four Year Period at Barrow, Alaska. Prepared for submission to Journal of Geophysical Research

Currently, sea ice cover in the Arctic is undergoing a rapid transformation to become more dominated by younger, more saline, first year ice (*Nghiem et al.*, 2007; *Kwok*, 2007; *Maslanik et al.*, 2011). First year sea ice areas contain a wide variety of environmental ice surfaces that may influence halogen activation. First year ice, because it is younger, tends to be thinner and more prone to lead formation (areas of open water in predominantly sea ice areas). While not directly implicated in halogen activation, multiple studies show that lead opening potentially changes the vertical distribution of BrO through enhanced vertical mixing (e.g. *McElroy et al.*, 1999; *Moore et al.*, 2014). Airborne studies by *McElroy et al.* (1999) suggest that the opening of leads causes transport of reactive halogens beyond the near surface layer into the free troposphere. More recently, *Moore et al.* (2014) observed that lead opening facilitates vertical mixing, as evidenced by transport of ozone and mercury from aloft into the near surface layer. *Peterson et al.* (2015) found that the vertical extent of halogen events is tied to local atmospheric stability, implying that lead induced vertical mixing could facilitate the transport of reactive halogens out of the near surface layer. *Nghiem et al.* (2012) showed a rising air parcel model with bromine sourced from recently opened leads reproduced BrO vertical column densities observed via satellite instruments. The prevalence of open water in a young ice pack also has the potential to change the characteristics of Arctic aerosol particles (*Browse et al.*, 2014), which have been implicated in halogen activation processes (*Hara et al.*, 2002).

Freshly opened leads that are re-freezing are also conducive to the formation of frost flowers. Frost flowers are a vapor-deposited ice form that have a variety of impacts on the local environment (*Barber et al.*, 2014). Frost flowers are hypothesized to impact reactive halogen chemistry due to their high bulk salinity and presumed specific surface area (*Rankin et al.*, 2002; *Kaleschke et al.*, 2004). It is also thought that changes in sea ice could lead to more frost flowers being present throughout the Arctic (*Douglas et al.*, 2012). However, work by *Dominé et al.* (2005) shows that frost flowers have comparable specific surface area to snow. This finding, combined with the low abundance of frost flowers when compared to snow, suggests that saline snow, which is prevalent in sea ice regions, is a more important source of reactive halogens. This theory is supported by recent laboratory studies (e.g. *Wren et al.*, 2013), field studies (e.g. *Simpson et al.*, 2005; *Stutz et al.*, 2011; *Pratt et al.*, 2013), and modeling work (e.g. *Piot and von Glasow*, 2008; *Thomas et al.*, 2012; *Toyota et al.*, 2014). Recent changes in sea ice cover also have implications for the overlying snowpack, as delays in formation of new sea ice in the fall due to a warming climate could lead to decreased snow depth on top of new sea ice (*Webster et al.*, 2014).

Multiple short term field studies have attempted to ascertain the dependence of observed halogen activation on contact with first year sea ice areas by using a combination of BrO measurements and back trajectory modeling (e.g. *Frieß*, 2004; *Simpson et al.*, 2007b; *Frieß et al.*, 2011).

Both *Frieß* (2004) and *Simpson et al.* (2007b) used low elevation differential slant column density (dSCD) measurements of BrO to examine the relationship between FYI contact times and levels of BrO, finding a relationship between time in sea ice areas and BrO. In particular, *Simpson et al.* (2007b) found that observed BrO was highly correlated with first year ice contact (R=0.74) during a 40 day field study in 2005 at Barrow, Alaska. However, dSCD measurements depend not only on the amount of BrO present, but also the visibility at the time of the measurement, complicating the interpretation of these BrO data. *Frieß et al.* (2011) account for visibility differences using optimal estimation to retrieve BrO concentration profiles versus altitude, as well as lower tropospheric vertical column densities (LT-VCD) with a combination of dSCD measurements, radiative transfer modeling, and an assumed a priori distribution. They found their observations of BrO and FYI contact at Barrow were not correlated (R<0.2) to the degree seen in *Simpson et al.* (2007b). Again, these results are also from a month long study at Barrow, Alaska, in 2009, and thus might not properly reflect the full extent of the relationship between BrO and time spent in first year ice areas. Additionally, work by *Gilman et al.* (2010) showed that ozone measurements, which decrease during halogen activation events, were best anti-correlated (R=-0.86) with sea ice contact in general, regardless of ice age. Similarly, studies using back trajectory analysis to examine the origins of ozone depletion events (e.g *Bottenheim and Chan*, 2006; *Oltmans et al.*, 2012) show that ozone depleted air masses observed at coastal sites typically originate in sea ice areas, but do not explore the role of first year ice versus multi-year ice areas.

Given the differing degrees of correlation observed in previous work, it is clear that questions remain about the role of FYI contact, and sea ice contact in general, in halogen activation. Thus, it is clear a longer term study is needed to clarify the role of FYI and sea ice areas in the activation and recycling of halogens. To that end, this present work uses MAX-DOAS observations of BrO from 2008, 2009, 2012, and 2013 to examine the influence of FYI on the amount of BrO retrieved at Barrow, Alaska. This study explores the correlation between multiple types of sea ice contact and BrO LT-VCDs at the BARC building over multiple years. Additionally, we use BrO observations from ice-tethered buoys (O-Buoys) in the Arctic ocean to investigate halogen activation events at remote sea ice sites.

4.3 Methods

4.3.1 BrO Measurements

We used multiple-axis differential optical absorption spectroscopy (MAX-DOAS) (*Hönninger et al.*, 2004) in conjunction with radiative transfer modeling (*Rozanov et al.*, 2005; *Deutschmann et al.*, 2011) to obtain BrO concentration profiles near Barrow, Alaska, from the top of the Barrow

Arctic Research Center (BARC) building, located at 71.325° N , 156.668° W. The particular MAX-DOAS instrument used is described in *Peterson et al.* (2015). This instrument measured scattered sunlight at 1°, 2°, 5°, 10°, 20°, and 90° (zenith) over a 30 minute span to obtain dSCDs for both O_4 and BrO using QDOAS software (*Fayt et al.*, 2011). This software fits the relative absorption of each low elevation spectrum to the temporally coincident zenith spectrum in the 346 to 364 nm wavelength region using a linear combination of absorption cross-sections (See Table 4.1), a 3rd order polynomial to account for broadband scattering processes, such as Rayleigh and Mie scattering, and a spectral offset to account for light scattered within the spectrometer. The absorption cross-sections were convoluted with an instrumental resolution function determined from spectra of a low pressure Hg lamp (334 nm peak) prior to being used by QDOAS. Fitting errors for each MAX-DOAS campaign used in this study are given in Table A.1. These dSCDs were then used to obtain lower tropospheric vertical column densities (LT-VCD) of BrO using analysis procedures fully detailed in *Peterson et al.* (2015) and briefly described here.

We combined the O_4 and BrO dSCD measurements with radiative transfer modeling to obtain profiles of BrO using techniques previously published in *Frieß et al.* (2011). Briefly, O_4 dSCDs are used in conjunction with the radiative transfer model SCIATRAN (*Rozanov et al.*, 2005) to obtain a profile of aerosol particle extinction in the lowest two kilometers of the atmosphere using optimal estimation (*Frieß et al.*, 2006). This retrieval requires a priori assumptions which are identical to those used in *Frieß et al.* (2006) for this analysis. BrO profiles are also retrieved in the same fashion using the Monte Carlo radiative transfer model McArtim (*Deutschmann et al.*, 2011) and the previously retrieved aerosol particle extinction profile (*Frieß et al.*, 2011). Again, the BrO a priori assumptions required to retrieve the BrO profile are identical to those used in *Frieß et al.* (2011). The result of this two step inversion procedure is a profile of average BrO mixing ratios in 100 m thick layers, up to two kilometers. *Peterson et al.* (2015) detail a method to reduce the retrieved profiles to two quantities, the integrated column of BrO in the lowest 200m, and the integrated column from the surface to 2 km, which is referred to as the lower tropospheric vertical column density (LT-VCD). The ability to observe the entire BrO LT-VCD with MAX-DOAS is highly contingent on visibility, with the degrees of freedom in the aloft layer being an effective proxy for ability to observe the full LT-VCD of BrO. For this study, we only analyze LT-VCDs with 0.7 degrees of freedom in the aloft layer, which is consistent with previous work examining reducing the influence of a priori assumptions on quantities retrieved using inverse methods. (*Payne et al.*, 2009). Additionally, we do not analyze data where O_3 is less than 1 nmol mol^{-1}, to account for potential altering of the partitioning of reactive bromine at low ozone (*Simpson et al.*, 2007b; *Helmig et al.*, 2012). LT-VCD errors for each MAX-DOAS campaign used in this study are given in Table 4.3.

4.3.2 O-Buoy Measurements

The O-Buoy is an autonomous platform designed to be deployed in sea ice and collect chemical measurements while drifting with the ice floe on which it is deployed (*Knepp et al.*, 2010). MAX-DOAS instruments on each buoy (*Carlson et al.*, 2010) are used to retrieve BrO using the same methods described above. Figure 4.1 shows the locations where we retrieved BrO using O-Buoys. O-Buoy 2 (OB2) was deployed in the Beaufort Sea in October of 2010, after drifting through the winter, it measured BrO from April 5th, 2011 until August 22nd, 2011. The MAX-DOAS instrument on OB2 uses an Ocean Optics HR2000 spectrometer with a spectral range of 318 to 455 nm. O-Buoy 6 (OB6) was deployed at the North Pole Environmental Observatory on April 10th, 2012 and collected data until July 2nd, 2012. The MAX-DOAS instrument on OB6 uses a Maya Pro spectrometer with a spectral range of 323 to 450 nm, the entrance optics on OB6 are upgraded from that of OB2 with the addition of a MEMS tilt meter. In both buoys, the spectrometer is passively cooled through contact with the buoy hull, which is in contact with the ocean, maintaining an operating instrument temperature of 6°C. To facilitate comparison with data from the BARC building, we restricted further analysis to data collected prior to June 1st for both O-Buoy timeseries.

4.3.3 Back Trajectory Modeling and Sea Ice Masks

We calculated contact time with different ice types using a combination of back trajectory modeling (HYSPLIT trajectory model (*Draxler and Rolph*, 2013)) and remotely sensed sea ice concentration data. We calculated 72 hour back trajectories hourly with a 50 m arrival height (*Simpson et al.*, 2007b) using meteorological fields derived from the NCEP Global Data Assimilation System (GDAS) modeling.

Because perennial ice and seasonal ice have differing physical characteristics, satellite scatterometery can be used to generate ice masks that classify sea ice areas as one of three types, first year ice (FYI), multi-year ice (MYI), or a combination of the two (MIX) (*Nghiem et al.*, 2005, 2006, 2007). For this study, we calculated ice contact times for each trajectory by overlaying the calculated back trajectories on quarter degree resolution monthly sea ice age masks derived from QuickSCAT data for 2008 and 2009. For 2012 and 2013, Oceansat-2 data were used to generate the sea ice age masks. We defined contact time with FYI as a sum of the contact time with mixed ice (MIX) and FYI. Figure 4.2 shows a sample trajectory from April 15th 2012, overlain on the sea ice mask. For each trajectory calculation, we calculated ice contact following the methods outlined in *Simpson et al.* (2007b). We accounted for uncertainties in the back trajectory by calculating average ice contact over a circular region with a radius starting at zero, and expanding by 2 km for every

hour along the back trajectory. To account for an air mass losing contact with sea ice due to vertical transport, we only considered data where the air parcel was at an altitude of less than 100 m. These methods use daily sea ice concentration data provided by the National Snow and Ice Data Center (NSIDC) (*Cavalieri et al.*, 1996) to calculate ice contact by weighting time spent in each 25 km^2 pixel by the concentration of sea ice observed in each pixel. These ice concentration data are a different data set than used in the *Simpson et al.* (2007b) work, however the correlation of the ice contact values generated by these methods for the study period in the *Simpson et al.* (2007b) work was high (R = 0.85). Thus, while the sea ice contact values presented in this paper are generated from different ice concentration data, they are still comparable to the contact values generated in the 2005 data set used in *Simpson et al.* (2007b).

4.3.4 Calculation of Potential Frost Flower Contact

To analyze the potential impacts of frost flowers on BrO, we used a combination of back trajectory modeling, satellite sea ice concentration observations, and modeling results (*Simpson et al.*, 2007b). Frost flower coverage is a function of the amount of recently grown sea ice available, as well as the air temperature (*Kaleschke et al.*, 2004). *Kaleschke et al.* (2004) developed a maximum frost flower coverage parameterization that we used, along with daily sea ice concentration data provided by the National Snow and Ice Data Center (NSIDC), to calculate potential frost flower contact along a 72 hr back trajectory generated with HYSPLIT (*Draxler and Rolph*, 2013). For each point along a trajectory, we calculated maximum fractional frost flower coverage, using the open water fraction, which is an average over an increasing geographic radius as described above, and modeled surface temperature. We then multiplied the maximal frost flower coverage by the open water fraction to obtain a weighting factor for time spent at the point. Points where the trajectory was higher than 100 m were not included in the calculation. Calculating the sum over the trajectory provides a number, which we refer to as hours of frost flower contact over the 72 hour trajectory (*Simpson et al.*, 2007b).

4.4 Results

4.4.1 Overall Airmass History

Figure 4.3, left panel, shows the time spent in areas that are predominantly FYI is highly correlated with time in contact with all types of sea ice (R=0.93). The linear fit shows that on average, an airmass in sea ice areas spends 85% of that time in FYI dominated areas. This correlation implies that coastal measurements at Barrow are not suitable for comparing the effectiveness of FYI areas and MYI areas in general in activation of reactive halogens. In contrast, the right panel of Fig. 4.3

shows there is no correlation (R=0.04) between time spent in FYI areas and time in potential frost flower areas, implying that these data are suitable for examining the relationship between BrO and potential frost flowers independently of sea ice contact.

4.4.2 Correlation Between BrO and Types of Ice Regions

We examined the correlation between contact with sea ice areas and retrieved BrO LT-VCDs at Barrow for three differing types of sea ice areas. Figure 4.4 shows the correlation coefficients for each analysis. First, we examined the correlation of BrO and time spent in FYI areas over the previous three days. While the overall linear correlation is weak (R = 0.38), we observed a general increase in the average magnitude of the BrO LT-VCDs with increased time in FYI areas. We also examined the correlation with time in sea ice areas in general (Fig. 4.4, middle panel) and found, over the course of this study, that BrO and time in sea ice areas was similar to that of FYI (R=0.39). However, as noted above, all ice contact is highly correlated with FYI, so the correlation between BrO and either ice type is necessarily similar.

Figure 4.5 illustrates the short term linear correlation between time spent over FYI areas and the BrO LT-VCDs. The red line shows the mean LT-VCD calculated for each decile of data. This line is near zero when there is less than 6 hours spent in FYI areas in the past three days, and gradually increases to a plateau with $\approx$ 1.5 days spent over FYI areas. The inset histogram shows the distribution of time spent in FYI areas for the measured air masses. As shown by the inset histogram, the majority of observations during this study were of air masses that spent more than half a day in FYI areas over the three day back trajectory. While Fig. 4.5 shows low short term correlation between time in FYI areas and LT-VCDs of BrO, the red trend line does show that high LT-VCD values typically do not occur when the observed air mass has spent less than 12 hours in FYI areas over the previous three days.

Figure 4.6 shows the relationship between potential frost flower contact and halogen activation. The inset histogram shows that the majority of observations do not accumulate more than an hour in PFF areas. The small fraction of air masses that accumulate more overall time in PFF areas do not exhibit increased BrO, in fact the opposite behavior is observed. Additionally, the overall correlation observed is low (R = 0.04). It is also important to note there is a large spread in BrO LT-VCDs with no time spent in PFF areas, implying it is unlikely that time spent in PFF areas plays a significant immediate role in the activation of bromine.

4.4.3 Interannual variability at Coastal Site

The right panel of Fig. 4.7 shows the range of BrO LT-VCD values retrieved from the BARC building over the course of this study, binned by the year of the observations. Similarly, the middle panel shows the range of hourly in-situ ozone values provided by the National Oceanic and Atmospheric Administration (NOAA) Earth Systems Research Laboratory/Global Monitoring Division (ESRL/GMD), also binned by year. The right panel shows the portion of the three day back trajectory that the observed air mass spent over sea ice areas. In each plot, the red lines represent the median and the blue dot represents the average, which shows the general year to year trends. Figure 4.7 illustrates the year to year variability in these three quantities is related, with lower LT-VCDs coinciding with lower FYI contact and higher O_3. We also performed a one way analysis of variance (ANOVA) to compare the distributions of these three variables from year to year. This analysis and a subsequent multiple comparison test showed that the enhanced BrO LT-VCDs retrieved in 2012 are significantly higher than other years at the 95% confidence level. These enhanced levels of BrO are coincident with lower amounts of observed boundary layer O_3 and enhanced sea ice contact over the three days prior to measurement, which are also significantly different from other years at the 95% confidence level.

The top left panel of Fig. 4.8 shows the average magnitude of halogen activation events for a given year as a function of the average days of the three day back trajectory that air masses spent in contact with sea ice in the same year. From this limited sample (four seasons of data), we see a strong linear relationship (R=0.93) between the average percentage of time spent in FYI areas and the average magnitude of BrO LT-VCDs. The y-intercept of the linear fit is within error of zero, which one would expect if time spent in sea ice areas was a prerequisite to observe BrO. In contrast, the right panel of Fig. 4.8 shows the average magnitude of halogen activation events plotted versus the FYI extent for the given year. We calculated the FYI extent by subtracting the minimum extent for the prior year from the maximum extent for the current year. Any ice present during the sea ice minimum has survived a melt cycle and is considered multi-year ice, thus the difference in the two extents can be attributed solely to the growth of new FYI. Both extent values were obtained from the NSIDC (*Fetterer et al.*, 2014). Figure 4.8, top right panel, shows no linear correlation (R=-0.04) between these two quantities, the linear fit implies that BrO would decrease as FYI extent increases, which seems unlikely given what we currently know about halogen activation, and the short term linear correlation observed above. These results suggest there is no linear relationship between pan-Arctic FYI extent and BrO observations at Barrow. Similarly, the bottom panels of Fig. 4.8 show the linear correlation between pan-Arctic

sea ice extent and annual averageBrO is low (R=0.53), while time spent in sea ice areas is highly correlated with annual average BrO (R=0.94).

4.4.4 Comparison of Coastal and On Sea Ice Sites

Figure 4.11 shows the probability of observing a BrO LT-VCD of a level specified on the x-axis, both at Barrow, and at remote on-ice sites. The blue line shows the overall distribution of LT-VCDs at all sites over the course of this study. Given the variation of sea ice contact times for air masses observed at the BARC building, we split the BARC observations into two bins. One bin consists of observations where the air mass spent less than 6 hours in FYI areas (red line), and the other is the remainder of observations at the BARC building. The distribution of LT-VCDs for air masses with minimal sea ice contact shows the majority of these air masses contain little BrO. In contrast, air masses that have spent a larger percentage of the previous three days in FYI areas (green line) are more likely to contain higher LT-VCDs of BrO. At the ice-tethered O-Buoys (teal, purple) which are heavily influenced by sea ice due to their deployment location, we see variability in the BrO LT-VCD. At OB2, which we deployed in the Beaufort Sea, we see the distribution tends to lower amounts of BrO than retrieved at Barrow, while at OB6, deployed at the North Pole Environmental Observatory (NPEO), shows large amounts of BrO throughout the measurement period. Given that these O-Buoy deployments are not concurrent, we can not draw conclusions about the effectiveness of differing ice environments from these data. Additionally, because OB6 was deployed very close to the geographic North Pole, the daylength was essentially constant and much longer compared to other sites during this time period, which could have an unknown effect on BrO. However, it is important to note that despite both buoys being deployed in remote sea ice areas, we still observe times of near-zero BrO, and a large variability in the retrieved LT-VCDs.

4.5 Discussion

4.5.1 Influence of FYI on BrO

Calculations of three day back trajectories show that in the three days preceding our measurements at the BARC building, the majority of air masses observed spent a significant amount of time over FYI areas, which has been shown to lead to an increased amount of observed BrO compared to non-sea ice influenced measurements (*Simpson et al.*, 2007b; *Wagner et al.*, 2007), as well as being more likely to observe a boundary layer ozone depletion event (ODE) (*Oltmans et al.*, 2012). Figure 4.4 shows that we do not observe the high correlation of BrO and time in FYI areas seen in *Simpson et al.* (2007b) (R=0.74) or moderate correlation observed by *Wagner et al.* (2007)

(R=0.57), regardless of ice type, however, we do observe a higher correlation than seen in *Frieß et al.* (2011) (R < 0.2).

One issue potentially complicating the comparison of the current work to previous studies is the differing BrO metrics used. Recent developments in the analysis of MAX-DOAS data mean that more recent papers (e.g. *Frieß et al.*, 2011) use LT-VCDs of BrO retrieved using optimal estimation (*Rodgers*, 2000), while older papers (e.g *Frieß*, 2004; *Wagner et al.*, 2007; *Simpson et al.*, 2007b) use less processed dSCD data when examining these correlations. In principle, the retrieved LT-VCD is the better metric for BrO because it uses radiative transfer modeling to account for the influence of varying viewing geometry and visibility on measured dSCDs, leading to a more accurate estimation of the amount of BrO present. Examining the correlation between the dSCD values for BrO used in this study and calculated time in FYI areas leads to similar correlation as reported in this work (R=0.40, a figure similar to Fig. 4.5 can be found in the supplemental material), thus we are confident that the lower correlation observed in this work when compared to previous work is not due to differing BrO metrics.

The lower degree of correlation observed over a longer study period implies that the degree of correlation between time spent in FYI areas and BrO seen in *Simpson et al.* (2007b) is not normally observed at Barrow. It should also be noted that the observed relationship between retrieved BrO and time spent in FYI areas is likely non-linear. The trendline in Fig. 4.5 shows a steady rise to a plateau between 1 and 2 days of FYI contact, as well as a similar deviation in LT-VCD values at all amounts of time spent in FYI areas. Figure 4.10 shows the distribution of time spent in first year ice areas is different between the two data sets. During the period examined in the *Simpson et al.* (2007b) work (left panel), the distribution of time spent in FYI areas was centered around 1 day, while the FYI contact calculated in the data set (right panel) used in this work is more evenly distributed. Because half the 2005 data set is clustered around one day of FYI contact, with less data in the plateau area, it is reasonable that the relationship could appear more linear in the 2005 data than in the more extensive recent data set. Thus, it is likely that these differing observed FYI contact distributions, and the limited nature of the 2005 data set are responsible for the differences in observed short term correlation.

The expectation of short-term linear correlation between time spent in FYI areas and BrO LT-VCDs is driven by the assumption that the observed LT-VCD is primarily influenced by time in FYI areas. *Peterson et al.* (2015) showed that the LT-VCD is dependent on local atmospheric stability, with events more distributed throughout the lowest kilometer of the atmosphere having higher LT-VCDs despite their lower near-surface concentrations. They also showed that the LT-VCD of BrO exhibits diurnal cycling, with the LT-VCD increasing to a peak in the late afternoon before rapidly decaying at twilight (Solar Zenith Angle > 85°). Additionally, factors such as

variations in available aerosol particles (*Frieß et al.*, 2011), snowpack pH, and the bromide to chloride ratio in the snowpack (*Pratt et al.*, 2013) are also likely to influence the amount of observed halogen activation. While these factors may serve to confound the relationship between BrO and FYI areas in the short-term, it is likely that they do not affect the annual average behavior of BrO to the same extent as trends in air mass history.

Figure 4.5 shows that the retrieved BrO in air masses that have spent most of their time over sea ice areas is still variable, varying from near-zero to 8×10^{13}molecules/cm^2. Despite the differences in short-term correlation, this expanded data set also shows that contact with first year ice areas is more predictive of enhanced halogen activation than potential frost flower contact, and that the magnitude of a halogen event, while tied to time spent over sea ice areas, is also dependent on other environmental parameters. It is important to note that these contact times are derived from quarter degree pixels categorized using scatterometery. While these methods do provide useful information about the role of sea ice areas, they can not evaluate the effectiveness of specific features of the sea ice environment (e.g. leads, frost flowers, saline snow) as halogen sources. However, assuming that the parameterization put forth in *Kaleschke et al.* (2004) is correct, Fig. 4.6 shows it is unlikely frost flowers play a direct role in the activation of bromine over this study period. Thus, while we observe lower correlation between BrO and time spent in FYI areas in these data, this long term study still supports the conclusions of *Simpson et al.* (2007b).

4.5.2 Interannual Variations

Oltmans et al. (2012) tie variability in ozone observations at Barrow to the origin of the air mass, with more depleted air masses originating in the Arctic ocean. They also note large interannual variability in air mass origin and local meteorology. As shown in Fig. 4.7, we observe similar trends with our halogen observations, with enhanced observations of halogens coinciding with years where most observed air masses were in contact with sea ice. Figure 4.8 shows that the year to year variability in BrO LT-VCDs is highly correlated with time spent in FYI areas, with enhanced BrO LT-VCDs in 2012 coinciding with high levels of sea ice contact. Additionally, Fig. 4.9 shows that air masses that spend a significant time over land do not contain large amounts of BrO. If one defines highly activated events as events in the top quartile of events over the study period, Fig. 4.9 shows highly activated events do not typically occur when an airmass has not spent time over FYI areas, and the the probability of observing a highly activated event shows a non-linearly increasing trend with time in sea ice areas.

Figure 4.8 illustrates the need to consider interannual variability in air mass origins prior to using data from coastal sites to comment on pan-Arctic trends. Recent studies (e.g. *Spolaor et al.*, 2013a,b) use coastal ice core halogen measurements at Svalbard and Talos Dome, Antarctica to

estimate past sea ice extent. However, the right panels of Fig. 4.8 shows that the relationship between BrO observed at coastal sites and pan-Arctic sea ice extent is unclear. This work suggests these reconstructions may be more reflective of variations in transport to the measurement site than trends in sea ice extent. This finding also implies that using coastal measurements to examine pan-Arctic trends in bromine activation, as well as subsequent ozone depletion and mercury deposition, should be done with caution.

4.5.3 Coastal vs Remote Site Comparison

Multiple studies (e.g. *Bottenheim and Chan*, 2006; *Oltmans et al.*, 2012) have observed more frequent ozone depletion in air masses that spend time in the Arctic Ocean prior to arriving at coastal measurement sites. *Bottenheim and Chan* (2006) suggest this is due to ozone depletion chemistry taking place in specific regions in the high Arctic prior to observations at coast sites while *Gilman et al.* (2010) observed the correlation between ice contact and boundary layer ozone levels increased at higher latitudes. Given that ozone has a longer lifetime (days) than BrO (minutes, in the absence of heterogeneous recycling), using ozone measurements to examine active halogen activation requires caution; However, these findings to indicate that a comparison of halogen activation events observed at lower latitude coastal sites and on ice observations at higher latitudes may yield useful information.

Figure 4.11 illustrates the differing distributions of BrO LT-VCDs at a variety of sites. Both O-Buoy deployments show a large degree of variability in BrO while being deployed in remote sea ice regions, with nearly all transport to the O-buoy passing over some type of sea ice, implying that while sea ice contact is required for bromine activation, BrO remains highly variable, indicating that other controls play an important role in affecting bromine activation. Additionally, the large LT-VCDs retrieved at OB6, which was deployed in a multi-year ice dominated area, shows that MYI areas may be capable of facilitating bromine activation and recycling, although the interpretation of the OB6 data is complicated by the essentially 24 hour day length during this measurement period when compared to sites at lower latitudes that have a day/night diurnal cycle. Given that the release of reactive halogens from ice surfaces and resulting ozone depletion is driven by photochemical processes, it is likely that the increased sunlight and lack of nocturnal reservoir formation during this time period play a role in determining the level of BrO observed, in addition to the characteristics of the ice environment where OB6 was deployed.

Pratt et al. (2013) found that saline snow is much more effective in facilitating bromine activation than an actual sea ice surface and that the release of Br_2, a precursor to BrO, was more effective when the snow exhibited an acidic pH and enhanced bromide to chloride ratio, indicating that some atmospheric processing is needed for the release of bromine. Thus, it is reasonable

that the snowpack in multi-year ice areas could also be effective recycling bromine, despite the decreased salinity of the snowpack in MYI areas compared to FYI areas (*Krnavek et al.*, 2012). This conclusion is also supported by our observation that BrO levels are slightly better correlated with time in sea ice areas as opposed to time spent solely FYI areas as well as the observations of *Stutz et al.* (2011) that showed bromine activation taking place at Summit, Greenland, far from FYI areas.

4.6 Conclusions

This work examines correlations between BrO LT-VCDs and a variety of ice types, finding that of the three types examined, BrO is most highly correlated with time spent in sea ice areas, although the correlation with time spent in FYI areas is nearly identical. We find no relationship between time spent in PFF areas and BrO, supporting the idea that time spent in areas of potential frost flower contact does not play a direct role in the activation of reactive bromine. While the overall linear correlation between BrO and time in FYI areas is weak, the average magnitude of an event, as well as the probability of observing a highly activated air mass, steadily increases with time spent in FYI areas.

Examining the inter-annual variability in our measurements at the BARC building shows that much of the variability in observations at Barrow is tied to variations in air mass history, rather than a response of halogen activation to changing sea ice characteristics. In 2012 we retrieved high LT-VCDs relative to the rest of this study due to enhanced sea ice contact that year. Because these variations in calculated sea ice contact are not necessarily tied to pan-Arctic trends, using measurements at coastal sites to evaluate pan-Arctic BrO trends and the response of halogen chemistry to changing sea ice conditions should be done with caution.

O-Buoy measurements show that observed halogen activation is highly variable across the Arctic, with BrO LT-VCDs ranging from near-zero levels to 8×10^{13} molecules cm^{-2}, even in remote on-ice locations. The high levels of BrO retrieved by OB6, which measured BrO in an area that is predominantly multi-year ice may suggest a potential role for multi-year ice areas in facilitating halogen activation, although the presence of 24 hour daylight at this deployment location complicates interpretation of these data.

4.7 Acknowledgements

The research at the University of Alaska was supported by the National Aeronautics and Space Administration (NASA) Cryospheric Sciences Program (CSP), as well as the National Science Foundation under grant ARC-1023118. The authors gratefully acknowledge the NOAA Air Resources Laboratory (ARL) for the provision of the HYSPLIT transport and dispersion model used in this publication, as well as Alexei Rozanov from IUP Bremen for providing the SCIATRAN

radiative transfer code. The deployment of the OB2 was carried out with the assistance of Carlton Rauschenberg (Bigelow), Kris Newhall (WHOI), the 2010 JOIS science team, and the crew of the CCGS Louis St. Laurent. OB6 was deployed by Steve Walsh (UAF) and Chris Williams (CRREL). The research at the Jet Propulsion Laboratory, California Institute of Technology, was supported by the NASA CSP.

4.8 References

Barber, D. G., J. K. Ehn, M. Pućko, S. Rysgaard, J. W. Deming, J. S. Bowman, T. Papakyriakou, R. J. Galley, and D. H. Søgaard (2014), Frost flowers on young Arctic sea ice: The climatic, chemical and microbial significance of an emerging ice type, *Journal of Geophysical Research: Atmospheres*, pp. n/a–n/a, doi: 10.1002/2014JD021736.

Barrie, L. A., J. W. Bottenheim, R. C. Schnell, P. J. Crutzen, and R. A. Rasmussen (1988), Ozone destruction and photochemical reactions at polar sunrise in the lower Arctic atmosphere, *Nature*, *334*(6178), 138–141, doi: 10.1038/334138a0.

Bottenheim, J. W., and E. Chan (2006), A trajectory study into the origin of spring time Arctic boundary layer ozone depletion, *Journal of Geophysical Research*, *111*(D19), D19,301, doi: 10.1029/2006JD007055.

Browse, J., K. S. Carslaw, G. W. Mann, C. E. Birch, S. R. Arnold, and C. Leck (2014), The complex response of Arctic aerosol to sea-ice retreat, *Atmospheric Chemistry and Physics*, *14*(14), 7543–7557, doi: 10.5194/acp-14-7543-2014.

Carlson, D., D. Donohoue, U. Platt, and W. R. Simpson (2010), A low power automated MAX-DOAS instrument for the Arctic and other remote unmanned locations, *Atmospheric Measurement Techniques*, *3*(2), 429–439, doi: 10.5194/amt-3-429-2010.

Cavalieri, D. J., C. L. Parkinson, P. Gloersen, and H. Zwally (1996), Sea Ice Concentrations from Nimbus-7 SMMR and DMSP SSM/I-SSMIS Passive Microwave Data.

Chance, K. V., and R. J. Spurr (1997), Ring effect studies: Rayleigh scattering, including molecular parameters for rotational Raman scattering, and the Fraunhofer spectrum., *Applied Optics*, *36*(21), 5224–30.

Deutschmann, T., S. Beirle, U. Frieß, M. Grzegorski, C. Kern, L. Kritten, U. Platt, C. Prados-Román, J. Puķıte, T. Wagner, B. Werner, and K. Pfeilsticker (2011), The Monte Carlo atmospheric radiative transfer model McArtim: Introduction and validation of Jacobians and 3D features, *Journal of Quantitative Spectroscopy and Radiative Transfer*, *112*(6), 1119–1137, doi: 10.1016/j.jqsrt.2010.12.009.

Dominé, F., A. S. Taillandier, W. R. Simpson, and K. Severin (2005), Specific surface area, density and microstructure of frost flowers, *Geophysical Research Letters*, *32*(13), 2–5, doi: 10.1029/2005GL023245.

Douglas, T. A., F. Dominé, M. Barret, C. Anastasio, H. J. Beine, J. Bottenheim, A. Grannas, S. Houdier, S. Netcheva, G. Rowland, R. Staebler, and A. Steffen (2012), Frost flowers growing in the Arctic ocean-atmosphere-sea ice-snow interface: 1. Chemical composition, *Journal of Geophysical Research*, *117*, D00R09, doi: 10.1029/2011JD016460.

Draxler, R., and G. Rolph (2013), HYSPLIT (HYbrid Single-Particle Lagrangian Integrated Trajectory) Model access via NOAA ARL READY Website.

Fayt, C., I. De Smedt, V. Letocart, A. Merlaud, G. Pinardi, M. Van Roozendael, and M. V. A. N. Roozendael (2011), QDOAS Software User Manual.

Fetterer, F., K. Knowles, W. Meier, and M. Savoie (2014), Sea Ice Index: Arctic Median April 1981-2014, *Tech. rep.*, National Snow and Ice Data Center, Boulder, Colorado USA, doi: 10.7265/N5QJ7F7W.

Frieß, U. (2004), Dynamics and chemistry of tropospheric bromine explosion events in the Antarctic coastal region, *Journal of Geophysical Research*, *109*(D6), D06,305, doi: 10.1029/2003JD004133.

Frieß U., P. S. Monks, J. J. Remedios, A. Rozanov, R. Sinreich, T. Wagner, and U. Platt (2006), MAX-DOAS O_4 measurements: A new technique to derive information on atmospheric aerosols: 2. Modeling studies, *Journal of Geophysical Research*, *111*(D14), doi: 10.1029/2005JD006618.

Frieß U., H. Sihler, R. Sander, D. Pöhler, S. Yilmaz, and U. Platt (2011), The vertical distribution of BrO and aerosols in the Arctic: Measurements by active and passive differential optical absorption spectroscopy, *Journal of Geophysical Research*, *116*, doi: 10.1029/2011JD015938.

Gilman, J. B., J. F. Burkhart, B. M. Lerner, E. J. Williams, W. C. Kuster, P. D. Goldan, P. C. Murphy, C. Warneke, C. Fowler, S. A. Montzka, B. R. Miller, L. Miller, S. J. Oltmans, T. B. Ryerson, O. R. Cooper, A. Stohl, and J. A. de Gouw (2010), Ozone variability and halogen oxidation within the Arctic and sub-Arctic springtime boundary layer, *Atmospheric Chemistry and Physics*, *10*(21), 10,223–10,236, doi: 10.5194/acp-10-10223-2010.

Hara, K., K. Osada, K. Matsunaga, Y. Iwasaka, T. Shibata, and K. Furuya (2002), Atmospheric inorganic chlorine and bromine species in Arctic boundary layer of the winter/spring, *Journal of Geophysical Research*, *107*(D18), 4361, doi: 10.1029/2001JD001008.

Helmig, D., P. Boylan, B. Johnson, S. Oltmans, C. Fairall, R. Staebler, A. Weinheimer, J. Orlando, D. J. Knapp, D. D. Montzka, F. Flocke, U. Frieß, H. Sihler, and P. B. Shepson (2012), Ozone dynamics and snow-atmosphere exchanges during ozone depletion events at Barrow, Alaska, *Journal of Geophysical Research: Atmospheres*, *117*(D20), doi: 10.1029/2012JD017531.

Hermans, C., A. Vandaele, B. Coquart, A. Jenouvrier, M. F. Merienne, S. Fally, M. Carleer, and R. Colin (2001), Absorption bands of O_2 and its collision-induced bands in the 30,000-7500 cm^{-1} wavenumber region, in *IRS 2000: Current Problems in Atmospheric Radiation*, edited by W. L. Smith and Y. M. Timofeyev, pp. 639–642, Hampton, VA.

Hönninger, G., C. von Friedeburg, and U. Platt (2004), Multi axis differential optical absorption spectroscopy (MAX-DOAS), *Atmospheric Chemistry and Physics*, *4*(1), 231–254, doi: 10.5194/acp-4-231-2004.

Kaleschke, L., A. Richter, J. Burrows, O. Afe, G. Heygster, J. Notholt, A. M. Rankin, H. K. Roscoe, J. Hollwedel, T. Wagner, and H. W. Jacobi (2004), Frost flowers on sea ice as a source of sea salt and their influence on tropospheric halogen chemistry, *Geophysical Research Letters*, *31*(16), doi: 10.1029/2004GL020655.

Knepp, T. N., J. Bottenheim, M. Carlsen, D. Carlson, D. Donohoue, G. Friederich, P. A. Matrai, S. Netcheva, D. K. Perovich, R. Santini, P. B. Shepson, W. Simpson, T. Valentic, C. Williams, and P. J. Wyss (2010), Development of an autonomous sea ice tethered buoy for the study of ocean-atmosphere-sea ice-snow pack interactions: the O-buoy, *Atmospheric Measurement Techniques*, *3*(1), 249–261, doi: 10.5194/amt-3-249-2010.

Krnavek, L., W. R. Simpson, D. Carlson, F. Dominé, T. A. Douglas, and M. Sturm (2012), The chemical composition of surface snow in the arctic: Examining marine, terrestrial, and atmospheric influences, *Atmospheric Environment*, *50*(0), 349 – 359, doi: http://dx.doi.org/10.1016/j.atmosenv.2011.11.033.

Kwok, R. (2007), Near zero replenishment of the Arctic multiyear sea ice cover at the end of 2005 summer, *Geophysical Research Letters*, *34*(5), L05,501, doi: 10.1029/2006GL028737.

Malicet, J., D. Daumont, J. Charbonnier, C. Parisse, A. Chakir, and J. Brion (1995), Ozone UV spectroscopy. II. Absorption cross-sections and temperature dependence, *Journal of Atmospheric Chemistry*, *21*(3), 263–273, doi: 10.1007/BF00696758.

Maslanik, J., J. Stroeve, C. Fowler, and W. Emery (2011), Distribution and trends in Arctic sea ice age through spring 2011, *Geophysical Research Letters*, *38*(13), n/a–n/a, doi: 10.1029/2011GL047735.

McElroy, C. T., C. A. Mclinden, and J. C. McConnell (1999), Evidence for bromine monoxide in the free troposphere during the Arctic polar sunrise, *Nature*, *397*, 338–341, doi: 10.1038/16904.

Moore, C. W., D. Obrist, A. Steffen, R. M. Staebler, T. A. Douglas, A. Richter, and S. V. Nghiem (2014), Convective forcing of mercury and ozone in the Arctic boundary layer induced by leads in sea ice., *Nature*, doi: 10.1038/nature12924.

Nghiem, S. V., M. L. Van Woert, and G. Neumann (2005), Rapid formation of a sea ice barrier east of Svalbard, *Journal of Geophysical Research*, *110*(C11), C11,013, doi: 10.1029/2004JC002654.

Nghiem, S. V., Y. Chao, G. Neumann, P. Li, D. K. Perovich, T. Street, and P. Clemente-Colón (2006), Depletion of perennial sea ice in the East Arctic Ocean, *Geophysical Research Letters*, *33*(17), L17,501, doi: 10.1029/2006GL027198.

Nghiem, S. V., I. G. Rigor, D. K. Perovich, P. Clemente-Colón, J. W. Weatherly, and G. Neumann (2007), Rapid reduction of Arctic perennial sea ice, *Geophysical Research Letters*, *34*(19), L19,504, doi: 10.1029/2007GL031138.

Nghiem, S. V., I. G. Rigor, A. Richter, J. P. Burrows, P. B. Shepson, J. Bottenheim, D. G. Barber, A. Steffen, J. Latonas, F. Wang, G. Stern, P. Clemente-Colón, S. Martin, D. K. Hall, L. Kaleschke, P. Tackett, G. Neumann, and M. G. Asplin (2012), Field and satellite observations of the formation and distribution of Arctic atmospheric bromine above a rejuvenated sea ice cover, *Journal of Geophysical Research*, *117*, D00S05, doi: 10.1029/2011JD016268.

Oltmans, S. J., B. J. Johnson, and J. M. Harris (2012), Springtime boundary layer ozone depletion at Barrow, Alaska: Meteorological influence, year-to-year variation, and long-term change, *Journal of Geophysical Research*, *117*(19), D00R18, doi: 10.1029/2011JD016889.

Payne, V. H., S. A. Clough, M. W. Shephard, R. Nassar, and J. A. Logan (2009), Information-centered representation of retrievals with limited degrees of freedom for signal: Application to methane from the Tropospheric Emission Spectrometer, *Journal of Geophysical Research*, *114*(D10), D10,307, doi: 10.1029/2008JD010155.

Perovich, D. K., and J. A. Richter-Menge (1994), Surface characteristics of lead ice, *Journal of Geophysical Research*, *99*, 16,341–16,350, doi: 10.1029/94JC01194.

Peterson, P. K., W. R. Simpson, K. A. Pratt, P. B. Shepson, U. Frieß, J. Zielcke, U. Platt, S. J. Walsh, and S. V. Nghiem (2015), Dependence of the vertical distribution of bromine monoxide in the lower troposphere on meteorological factors such as wind speed and stability, *Atmospheric Chemistry and Physics*, *15*(4), 2119–2137, doi: 10.5194/acp-15-2119-2015.

Piot, M., and R. von Glasow (2008), The potential importance of frost flowers, recycling on snow, and open leads for ozone depletion events, *Atmospheric Chemistry and Physics*, *8*(9), 2437–2467, doi: 10.5194/acp-8-2437-2008.

Pratt, K. A., K. D. Custard, P. B. Shepson, T. A. Douglas, D. Pöhler, S. General, J. Zielcke, W. R. Simpson, U. Platt, D. J. Tanner, L. Gregory Huey, M. Carlsen, and B. H. Stirm (2013), Photochemical production of molecular bromine in Arctic surface snowpacks, *Nature Geoscience*, doi: 10.1038/ngeo1779.

Rankin, A. M., E. W. Wolff, and S. Martin (2002), Frost flowers: Implications for tropospheric chemistry and ice core interpretation, *Journal of Geophysical Research*, *107*(D23), doi: 10.1029/2002JD002492.

Rodgers, C. D. (2000), *Inverse Methods For Atmospheric Sounding: Theory and Practice*, World Scientific, Singapore.

Rozanov, A., H. Bovensmann, A. Bracher, S. Hrechanyy, V. Rozanov, M. Sinnhuber, F. Stroh, and J. Burrows (2005), NO_2 and BrO vertical profile retrieval from SCIAMACHY limb measurements: Sensitivity studies, *Advances in Space Research*, *36*(5), 846–854, doi: 10.1016/j.asr.2005.03.013.

Schroeder, W., K. Anlauf, L. Barrie, and J. Lu (1998), Arctic springtime depletion of mercury, *Nature*, pp. 16–17, doi: 10.1038/28530.

Simpson, W., L. Alvarez-Aviles, T. A. Douglas, M. Sturm, and F. Dominé (2005), Halogens in the coastal snow pack near Barrow, Alaska: Evidence for active bromine air-snow chemistry during springtime, *Geophysical Research Letters*, *32*, doi: 10.1029/2004GL021748.

Simpson, W. R., R. von Glasow, K. Riedel, P. Anderson, P. Ariya, J. Bottenheim, J. Burrows, L. J. Carpenter, U. Frieß, M. E. Goodsite, D. Heard, M. Hutterli, H.-W. Jacobi, L. Kaleschke, B. Neff, J. Plane, U. Platt, A. Richter, H. Roscoe, R. Sander, P. Shepson, J. Sodeau, A. Steffen, T. Wagner, and E. Wolff (2007a), Halogens and their role in polar boundary-layer ozone depletion, *Atmospheric Chemistry and Physics*, *7*(16), 4375–4418, doi: 10.5194/acp-7-4375-2007.

Simpson, W. R., D. Carlson, G. Hönninger, T. A. Douglas, M. Sturm, D. Perovich, and U. Platt (2007b), First-year sea-ice contact predicts bromine monoxide (BrO) levels at Barrow, Alaska better than potential frost flower contact, *Atmospheric Chemistry and Physics*, *7*(3), 621–627, doi: 10.5194/acp-7-621-2007.

Spolaor, A., J. Gabrieli, T. Martma, J. Kohler, M. B. Björkman, E. Isaksson, C. Varin, P. Vallelonga, J. M. C. Plane, and C. Barbante (2013a), Sea ice dynamics influence halogen deposition to Svalbard, *The Cryosphere*, *7*(5), 1645–1658, doi: 10.5194/tc-7-1645-2013.

Spolaor, A., P. Vallelonga, J. M. C. Plane, N. Kehrwald, J. Gabrieli, C. Varin, C. Turetta, G. Cozzi, R. Kumar, C. Boutron, and C. Barbante (2013b), Halogen species record Antarctic sea ice extent over glacial-interglacial periods, *Atmospheric Chemistry and Physics*, *13*(13), 6623–6635, doi: 10.5194/acp-13-6623-2013.

Steffen, A., T. Douglas, M. Amyot, P. Ariya, K. Aspmo, T. Berg, J. Bottenheim, S. Brooks, F. Cobbett, A. Dastoor, A. Dommergue, R. Ebinghaus, C. Ferrari, K. Gardfeldt, M. E. Goodsite, D. Lean, A. J. Poulain, C. Scherz, H. Skov, J. Sommar, and C. Temme (2008), A synthesis of atmospheric mercury depletion event chemistry in the atmosphere and snow, *Atmospheric Chemistry and Physics*, *8*(6), 1445–1482, doi: 10.5194/acp-8-1445-2008.

Stutz, J., J. L. Thomas, S. C. Hurlock, M. Schneider, R. von Glasow, M. Piot, K. Gorham, J. F. Burkhart, L. Ziemba, J. E. Dibb, and B. L. Lefer (2011), Longpath DOAS observations of surface BrO at Summit, Greenland, *Atmospheric Chemistry and Physics*, *11*(18), 9899–9910, doi: 10.5194/acp-11-9899-2011.

Thomas, J. L., J. E. Dibb, L. G. Huey, J. Liao, D. Tanner, B. Lefer, R. von Glasow, and J. Stutz (2012), Modeling chemistry in and above snow at Summit, Greenland - Part 2: Impact of snowpack chemistry on the oxidation capacity of the boundary layer, *Atmospheric Chemistry and Physics*, *12*(14), 6537–6554, doi: 10.5194/acp-12-6537-2012.

Toyota, K., J. C. McConnell, R. M. Staebler, and A. P. Dastoor (2014), Air-snowpack exchange of bromine, ozone and mercury in the springtime Arctic simulated by the 1-D model PHANTAS - Part 1: In-snow bromine activation and its impact on ozone, *Atmospheric Chemistry and Physics*, *14*(8), 4101–4133, doi: 10.5194/acp-14-4101-2014.

Vandaele, A., C. Hermans, P. Simon, M. Carleer, R. Colin, S. Fally, M. Mérienne, A. Jenouvrier, and B. Coquart (1998), Measurements of the NO_2 absorption cross-section from 42 000 cm^{-1} to 10 000 cm^{-1} (238-1000 nm) at 220 K and 294 K, *Journal of Quantitative Spectroscopy and Radiative Transfer*, *59*(3-5), 171–184, doi: 10.1016/S0022-4073(97)00168-4.

Wagner, T., O. Ibrahim, R. Sinreich, U. Frieß, R. von Glasow, and U. Platt (2007), Enhanced tropospheric BrO over Antarctic sea ice in mid winter observed by MAX-DOAS on board the research vessel Polarstern, *Atmospheric Chemistry and Physics*, *7*(12), 3129–3142, doi: 10.5194/acp-7-3129-2007.

Webster, M. A., I. G. Rigor, S. V. Nghiem, N. T. Kurtz, S. L. Farrell, D. K. Perovich, and M. Sturm (2014), Interdecadal changes in snow depth on Arctic sea ice, *Journal of Geophysical Research: Oceans*, pp. n/a–n/a, doi: 10.1002/2014JC009985.

Wilmouth, D. M., T. F. Hanisco, N. M. Donahue, and J. G. Anderson (1999), Fourier Transform Ultraviolet Spectroscopy of the $A\ ^2\Pi_{3/2} \leftarrow X\ ^2\Pi_{3/2}$ Transition of BrO, *The Journal of Physical Chemistry A*, *103*(45), 8935–8945, doi: 10.1021/jp991651o.

Wren, S. N., D. J. Donaldson, and J. P. D. Abbatt (2013), Photochemical chlorine and bromine activation from artificial saline snow, *Atmospheric Chemistry and Physics*, *13*(19), 9789–9800, doi: 10.5194/acp-13-9789-2013.

Figure 4.1: Deployment locations for O-Buoys used in this study. OB2 is on the bottom, in the Beaufort Sea. The label represents the location where we first started collecting data in April of 2011. OB6 is the northernmost deployment, and was deployed at the North Pole in April of 2012

Table 4.1: Absorber cross sections used in the MAX-DOAS fitting.

Species	Cross Section
BrO (223K)	*Wilmouth et al.* (1999)
O_3 (243K)	*Malicet et al.* (1995)
NO_2 (220K)	*Vandaele et al.* (1998)
O_4	*Hermans et al.* (2001)
Ring	Determined from zenith spectra using *Chance and Spurr* (1997)

Table 4.2: 1 σ errors for MAX-DOAS fitting over all deployments.

Location and Year	Mean RMS	BrO dSCD Error	O_4 dSCD Error
Barrow 2008	3.4×10^{-4}	1.7×10^{13} molecules cm^{-2}	4.1×10^{41} molecules^2 cm^{-5}
Barrow 2009	3.3×10^{-4}	1.7×10^{13} molecules cm^{-2}	4.0×10^{41} molecules^2 cm^{-5}
Barrow 2012	3.9×10^{-4}	1.9×10^{13} molecules cm^{-2}	5.1×10^{41} molecules^2 cm^{-5}
Barrow 2013	3.7×10^{-4}	1.8×10^{13} molecules cm^{-2}	4.9×10^{41} molecules^2 cm^{-5}
O-Buoy 2 2011	5.6×10^{-4}	2.4×10^{13} molecules cm^{-2}	6.8×10^{41} molecules^2 cm^{-5}
O-Buoy 6 2012	3.3×10^{-4}	1.6×10^{13} molecules cm^{-2}	4.3×10^{41} molecules^2 cm^{-5}

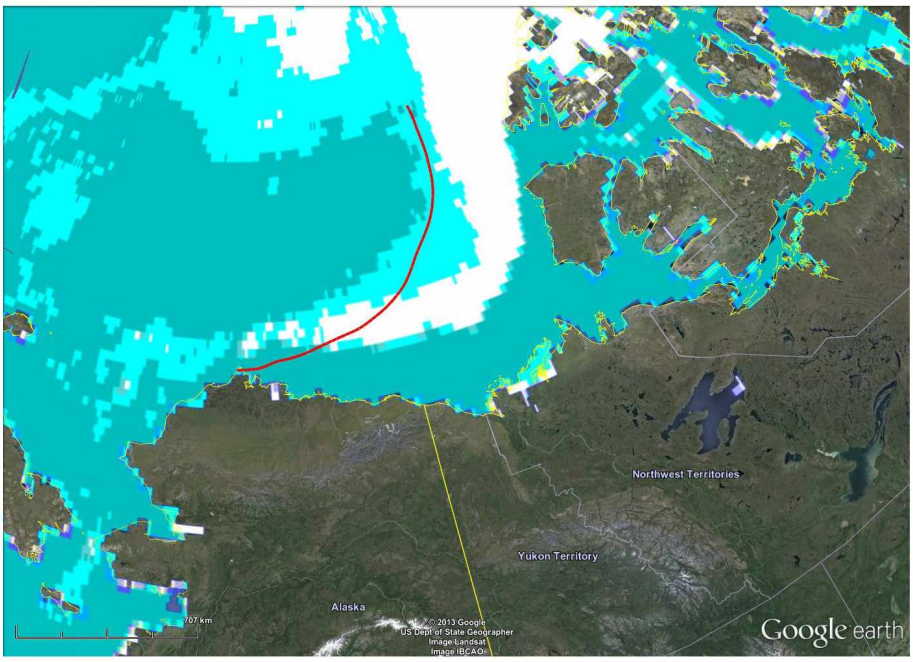

Figure 4.2: Example 72 hr back trajectory calculation from April 15th, 2012. The three day back trajectory calculated using HYSPLIT is shown using the red line, starting at Barrow, Alaska. This trajectory is overlaid on a three color mask of sea ice classifications. White areas represent MYI, while teal areas represent FYI and the transition between the two represents pixels that are classified as a mixture of both types. For the purposes of this study, we classify both shades of blue as FYI areas.

Table 4.3: 1 σ errors for BrO LT-VCD retrieval over all deployments.

Location and Year	BrO LT-VCD Error
Barrow 2008	4.0×10^{12} molecules cm^{-2}
Barrow 2009	4.0×10^{12} molecules cm^{-2}
Barrow 2012	3.8×10^{12} molecules cm^{-2}
Barrow 2013	4.3×10^{12} molecules cm^{-2}
O-Buoy 2 2011	4.8×10^{12} molecules cm^{-2}
O-Buoy 6 2012	7.3×10^{12} molecules cm^{-2}

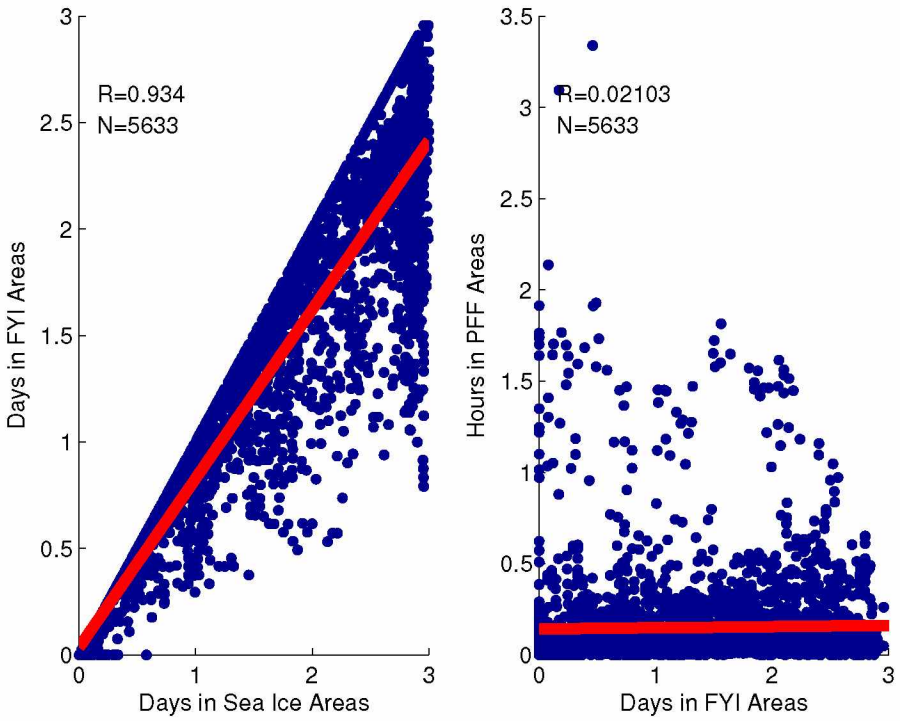

Figure 4.3: The calculated correlation between ice types examined in this study. The left panel shows the correlation between time spent in sea ice areas and time spent in areas that are predominantly FYI, while the right panel shows the relationship between potential frost flower contact and time spent in FYI areas. The red line shows the linear trend in each case.

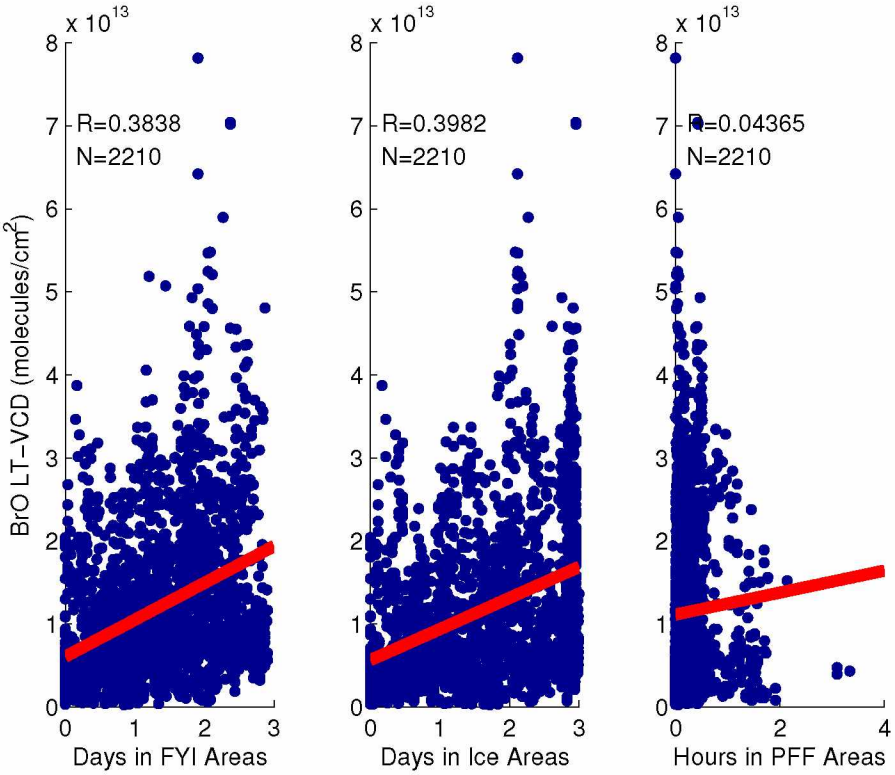

Figure 4.4: Correlation between BrO and time spent in areas with ice of various types. The red lines show a linear trendline. The left panel shows the relationship with first year ice, while the middle shows the relationship with all ice and the right panel shows the relationship with potential frost flowers. Note that the right panel x axis is in units of hours rather than days.

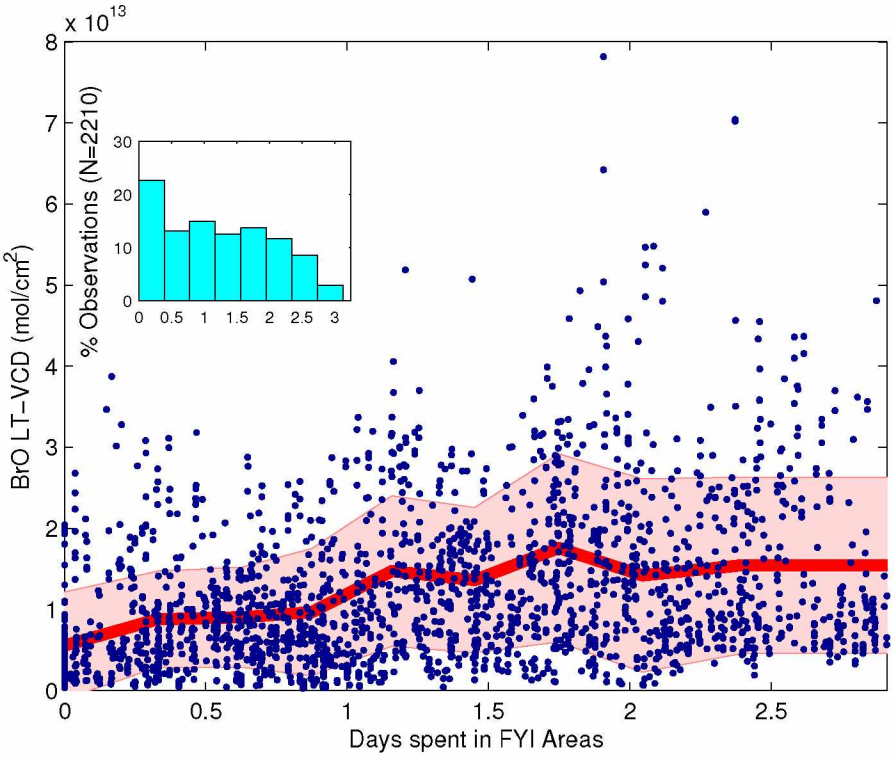

Figure 4.5: Observed BrO LT-VCD at the BARC building versus time spent in FYI areas. The red line represents the mean LT-VCD as a function of time spent in FYI areas, calculated from deciles on the x axis, while the shaded region represents one standard deviation. The inset histogram shows the overall percentage of observations taking place at various amounts of time in contact with sea ice.

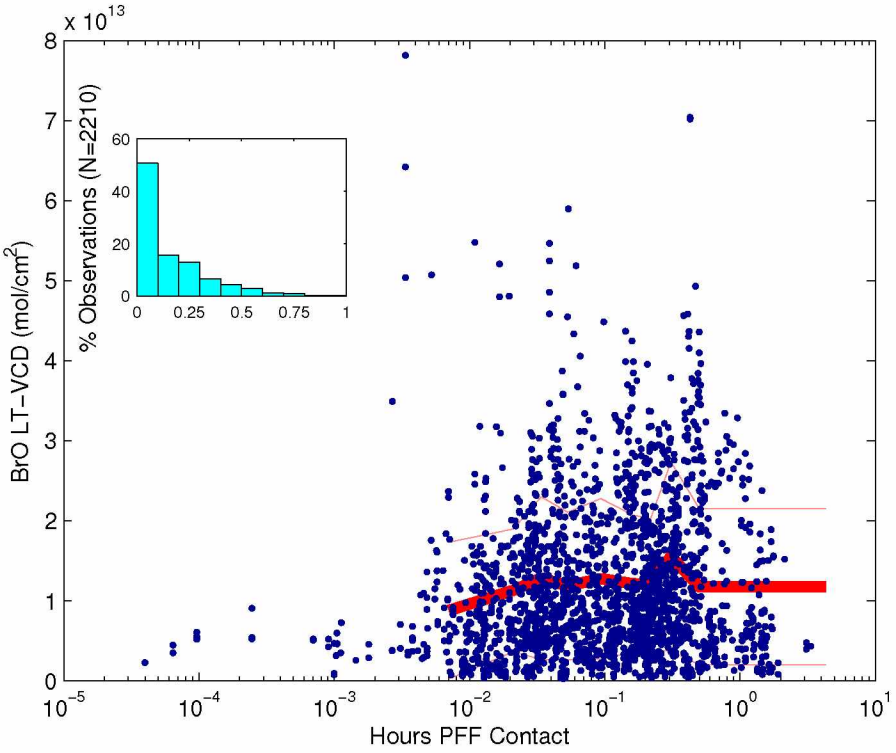

Figure 4.6: Observed BrO LT-VCD at the BARC building versus the amount of time spent in areas with potential frost flowers (PFF). The red line represents the mean LT-VCD as a function of PFF contact, calculated from deciles on the x axis, while the outlined region represents one standard deviation. The inset histogram shows the overall percentage of observations taking place at various amounts of time in areas with PFF.

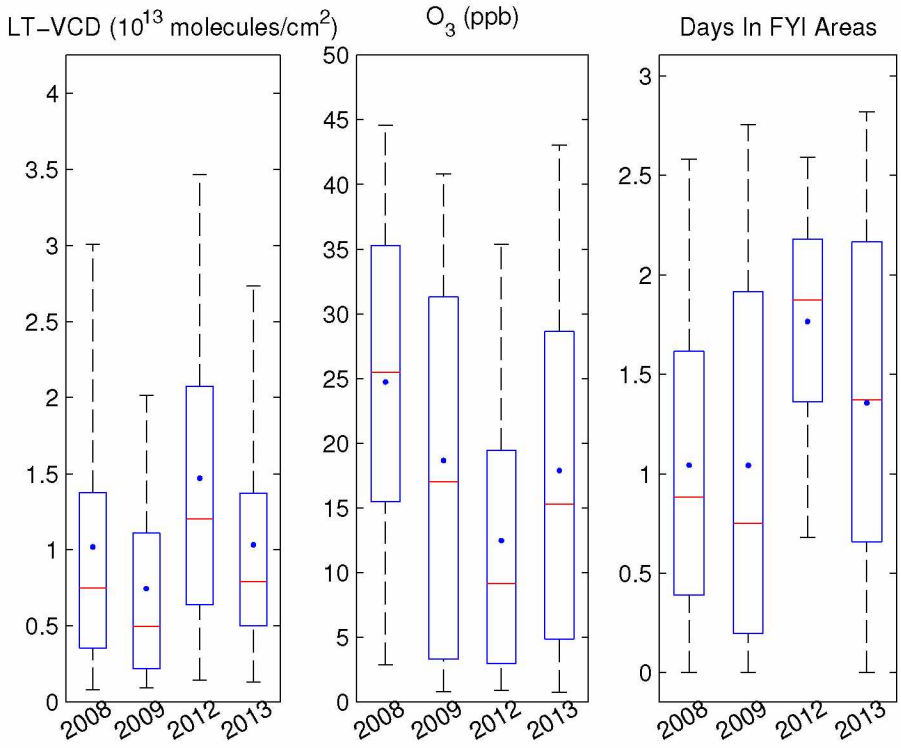

Figure 4.7: The year to year variability of BrO, O_3 and time in FYI areas prior to the measured airmass arriving at Barrow is shown here using a box and whisker plot. The red line is the median value, while the blue box shows the 25th to 75th percentile. Average values for each bin are shown using blue dots. The bars are drawn such that 95% of the data are included. Outliers are not shown.

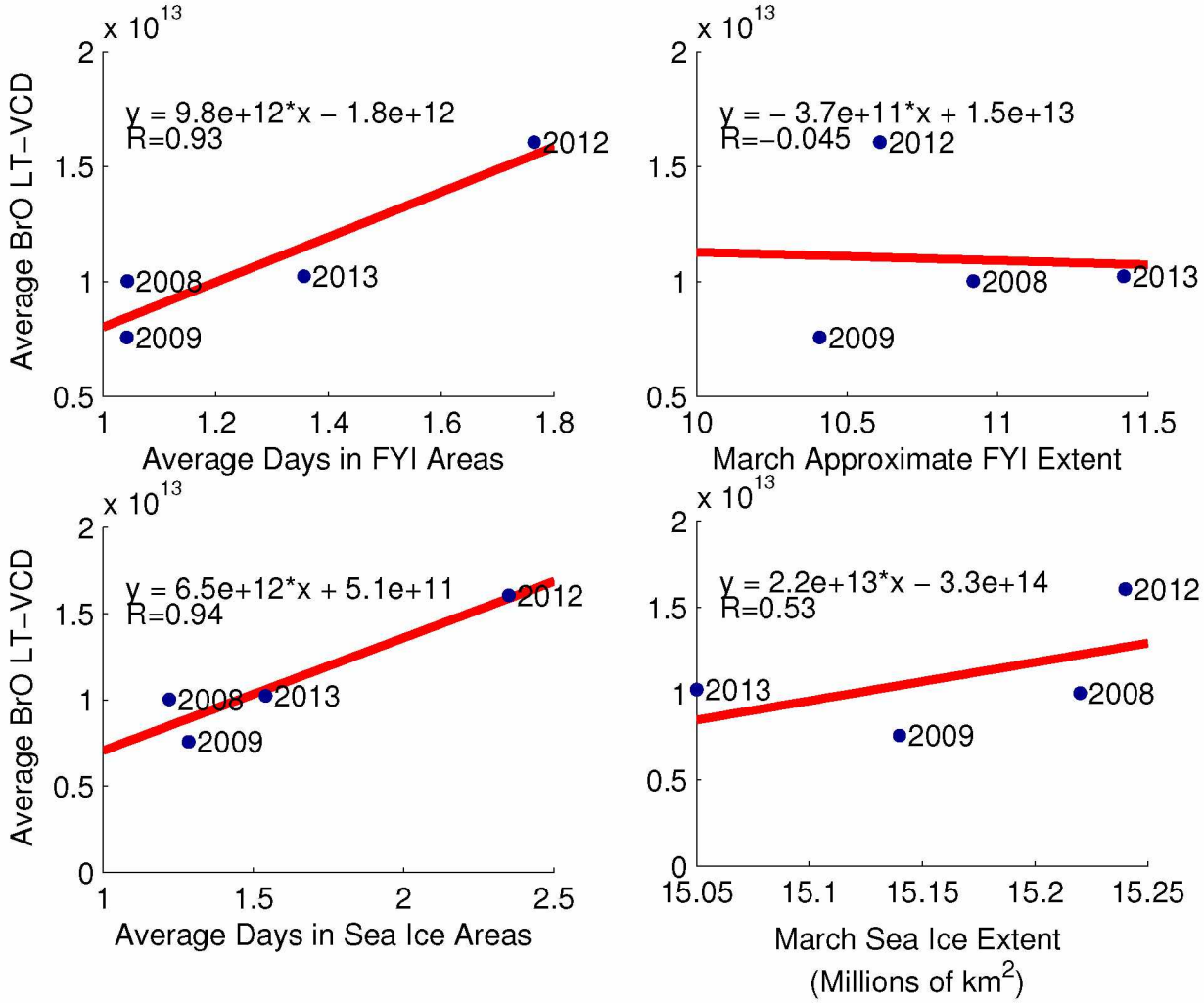

Figure 4.8: Observed relationship between BrO LT-VCDs and sea ice. The top left panel shows the annual average magnitude of BrO LT-VCDs at Barrow as a function of the amount of the previous three days spent in FYI areas while the top right panel shows the annual average BrO LT-VCD as a function of FYI extent. The bottom left panel shows the annual average magnitude of BrO LT-VCDs at Barrow as a function of the amount of the previous three days spent in all sea ice areas while the top right panel shows the annual average BrO LT-VCD as a function of March sea ice extent for the given year.

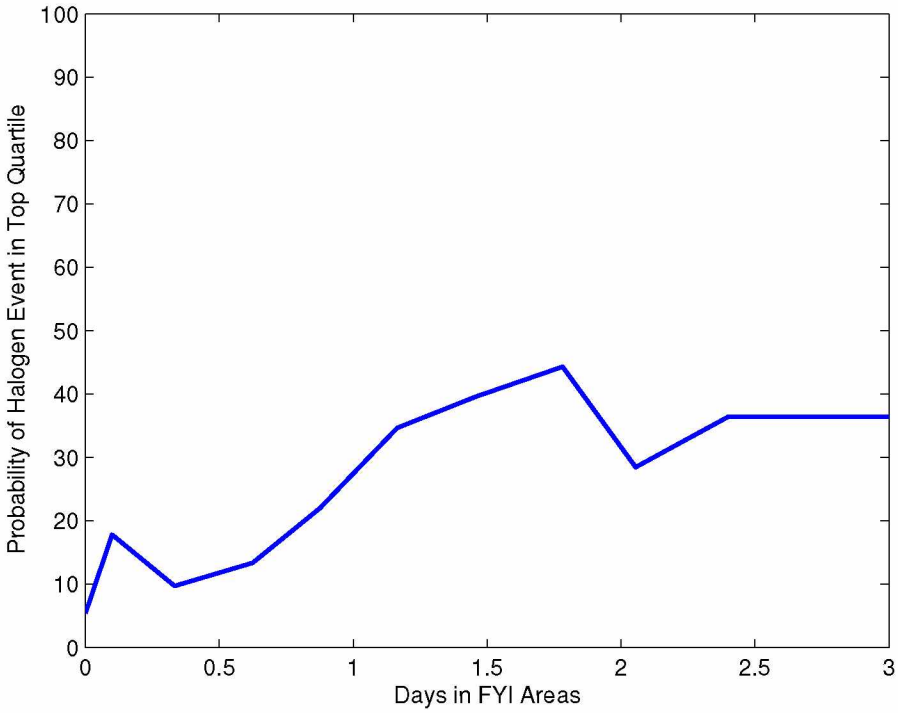

Figure 4.9: The probability of observing an airmass with bromine activation in the top quartile of observed halogen events over the study period as a function of time spent in FYI areas. Probabilities are calculated for each decile along the x axis.

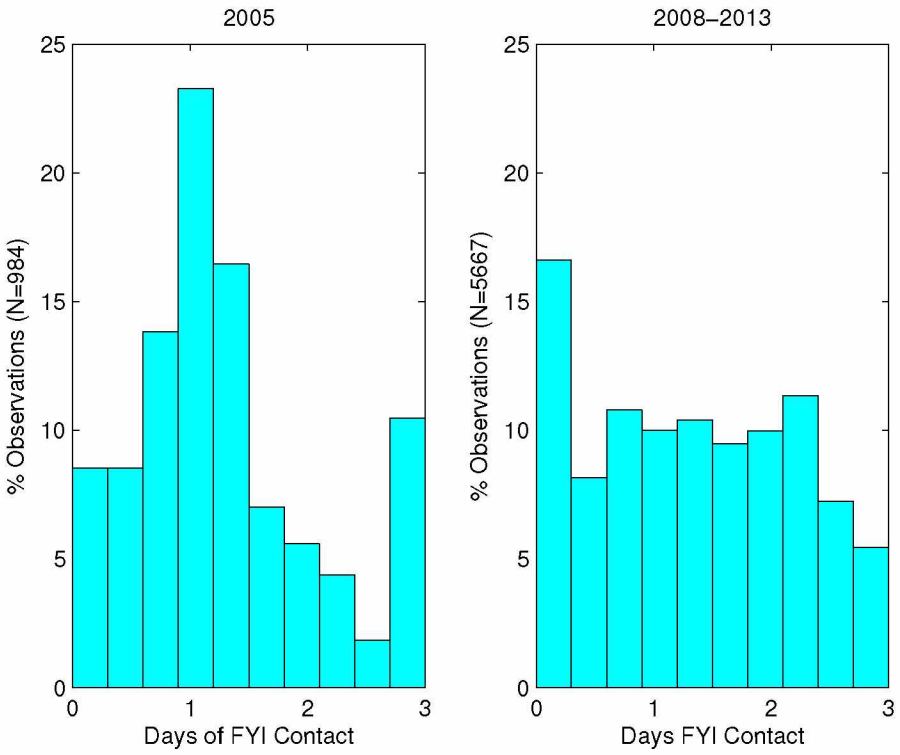

Figure 4.10: Histograms comparing first year ice contact calculated in *Simpson et al.* (2007a) with the current study. The left panel shows the FYI contact values from 2005, while the right panel shows the FYI contact calculated for this study.

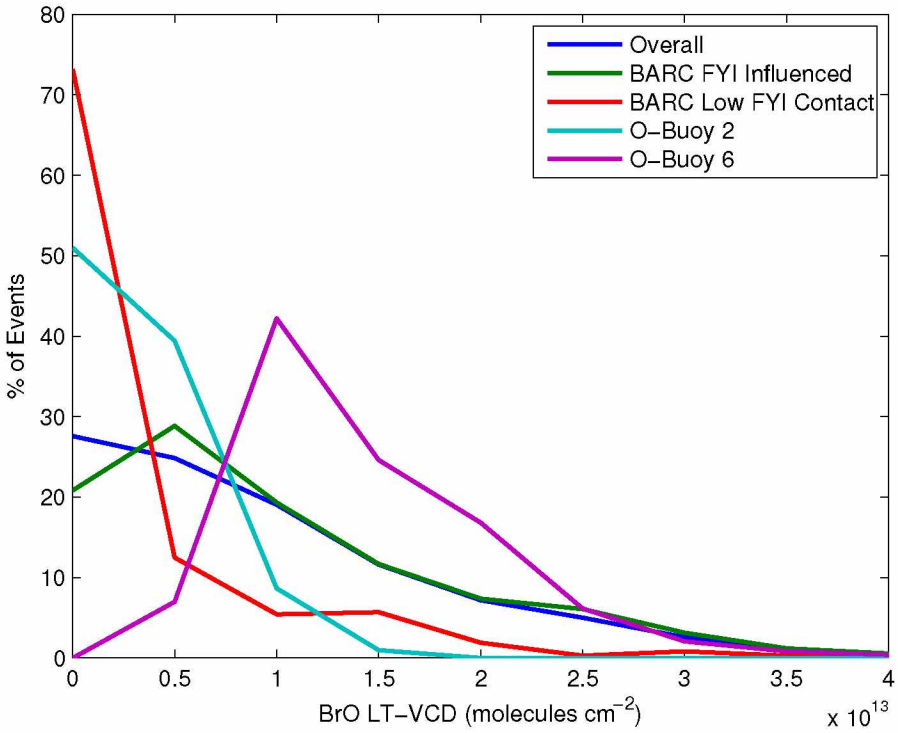

Figure 4.11: The probability of observing an activation event of a certain intensity. Observations from the BARC building are split into two bins, one with sea ice contact less than 6 hours in the last three days, and one with sea ice contact greater than 6 hours in the last three days. These curves are generated from bins 0.5×10^{13} molecules cm^{-2} wide.

Chapter 5
Conclusion and Future Outlook

5.1 Results

This dissertation outlines a new method to reduce MAX-DOAS observations to long term, visibility corrected, timeseries of lower tropospheric BrO column measurements at both coastal and remote on-ice measurement sites around the Arctic. This dissertation focuses primarily on quasi-continuous observations of BrO at Barrow, Alaska from 2008-2013. We used data collected at Barrow during the 2012 BROMEX field campaign to link the vertical distribution of BrO in the Arctic boundary layer to the local atmospheric stability. The near surface diurnal cycling of BrO observed at Barrow points to a surface snowpack source of bromine diluting throughout an expanding boundary layer, while the overall growth of boundary layer BrO points to concurrent activation of BrO aloft on aerosol particles. Given the lack of dependence of the observed aerosol particle extinction on wind speed, we find it is unlikely that these aerosol particles aloft are provided by concurrent blowing snow events requiring wind speeds above 8 miles per hour.

Obtaining four years of BrO LT-VCDs from Barrow led to the first long term examination of the influence of air mass history, specifically time in sea ice areas, on observed BrO at coastal sites. While multiple short term studies have previously examined this relationship, there are differing conclusions about the degree of influence of time spent in various ice areas on BrO in previous literature. The relationships examined in the larger data set show that time spent in PFF areas does not explain any of the observed variance in BrO at Barrow. In contrast, there is a relationship between time spent in FYI areas and BrO. This relationship appears to be non-linear, and shows that while time spent in FYI areas at some point in the previous three days is usually needed to observe BrO, it does not by itself control the observed level of halogen activation at Barrow. Despite the relatively weak linear correlation on half-hourly time scales, annual averages of BrO observed at Barrow are still well predicted (R=0.93) by the air mass history and contact with FYI areas. The weak short-term linear correlation is potentially due to other environmental parameters driving variability in the observed LT-VCDs. In Chapter 3, we showed that both the near-surface BrO and LT-VCD exhibit characteristic diurnal cycling, with LT-VCDs generally increasing throughout the day. Additionally, we showed that the LT-VCD is dependent on atmospheric stability, with more distributed column events having larger LT-VCDs. While these factors may serve to confound in the short-term, it is doubtful that they affect annual average behavior of BrO. A comparison of annual average BrO and time in FYI areas suggests that interannual variability of BrO observations at coastal sites is largely driven by air mass history, rather than pan-Arctic trends in sea ice cover.

In addition to examining the influence of large spatial scale ice types, it is important to examine the ice microstructures on which these reactions take place. This dissertation contributes to our overall understanding of ice/brine microstructures by non-destructively imaging the microstructure of these systems in three dimensions. These images show that brine is located in distinct regions rather than evenly thoughout the sample, and that ice surfaces of ice/brine systems are unevenly coated with brine.

5.2 Outlook

Our tomography work detailed in Chapter 2 has provided useful information on how brine is distributed in ice/brine systems and how much brine is available for chemical reactions required to sustain the bromine explosion annually observed in the polar regions. Many current efforts to model the influence of ice/brine systems on Arctic boundary layer chemistry assume uniform surface coverages based purely on bulk concentration. Given the findings of this dissertation, it is clear that that approach does not accurately capture the effect of ice/brine microstructures and that new modeling approaches taking the heterogeneous nature of brine on ice surfaces into account are needed.

Our analysis of trace gas retrieval using MAX-DOAS detailed in Chapter 3 has improved the communities understanding of the limitations of vertical profile data retrieved from ground based MAX-DOAS instruments via optimal estimation, as well as provided a broadly applicable method for obtaining visibility corrected LT-VCDs. Chapter 4 used four years of MAX-DOAS data at Barrow to clarify the role of various ice regions in halogen activation chemistry.

While Chapter 4 only details the role of sea ice areas in the activation of BrO, the techniques outlined in Chapter 3 also allow us to examine the influence of multiple environmental factors on BrO. In addition to air mass history, we also examined the influence of temperature (Fig. 5.1), surface ozone (Fig. 5.2), and wind speed (Fig. 5.3) on observed BrO. Figure 5.1 shows there is no linear correlation (R=-0.20) between temperature and BrO. The figure also clearly shows that halogens are not observed above freezing temperatures, which given the reliance of halogen chemistry on heterogeneous chemistry on ice surfaces, was obvious prior to this work. Figure 5.2 shows the relationship between BrO and O_3 is clearly non-linear (R = -0.15), with low amounts of BrO observed at both low and high amounts of ozone. The low amounts at low ozone are explained by ozone titration altering the partitioning of BrO_x as outlined in Chapter 3, while the low amounts of BrO at high O_3 simply imply that there is no active ozone depletion happening. Figure 5.3 shows there is no clear relationship between wind speed and BrO. The overall correlation is non-existent (R=0.03). This is a noteworthy finding, because as more fully detailed in Chapters 1 and 3, many people believe that "blowing snow" events at high wind

speeds play a large role in halogen activation, and most modeling work on these events uses a simple parameterization based solely on wind speed. Figure 5.3 coupled with the more detailed analysis shown in Chapter 3, show that this approach does not explain observed variability in BrO LT-VCDs, and that if blowing snow events are a source of reactive halogens, modeling of blowing snow events must be based on more then the presence of snow and high windspeed. It should also be pointed out that, of the variables studied, ice contact exhibits the highest observed linear correlation (R=0.39) with BrO.

Although these simple univariate analyses provide some useful information about the production of BrO, it is clear that simple univariate analysis fails to explain the observed variance in BrO, and that a multivariate analysis of the relationship between environmental parameters and our BrO observations may be useful. However, given the many multivariate regression techniques generally assume some degree of linear correlation between input variables, this may not be overly informative. It is likely that chemical mechanisms contribute to the non-linearity of the relationships between BrO and environmental parameters.

The results shown in Chapter 4 make it abundantly clear that more work is needed to fully understand the role of FYI regions in activation of halogens. While coastal measurements provide some insights, it is clear more analysis of on ice measurements at remote sea ice locations is needed. FYI is a complex region with a lot of variation in ice properties on the scale of the ice concentration data used in Chapter 4. A synthesis of higher resolution remote sensing data and on ice BrO measurements could help clarify the specific aspects of FYI areas that are effective in the release of reactive halogens.

The deployment of MAX-DOAS instruments at a variety of locations around the Arctic (See Figure 5.4), enables the use of the analysis techniques laid out in Chapters 3 and 4 to provide information on the horizontal and vertical distribution of BrO in the Arctic boundary layer over large timescales at a variety of locations, as well as validation of LT-VCDs retrieved via satellite-based instruments. Using ground-based measurements to improve the retrieval of LT-VCDs from satellite on a basin scale will allow for greater insight into pan-Arctic BrO trends. Given the extensive nature of this data set, the application of methods outlined in this work will greatly enhance our ability to evaluate potential physical mechanisms behind halogen activation, allowing us to better understand how chemical processes taking place in the Arctic boundary layer will change as a result of declining perennial sea ice.

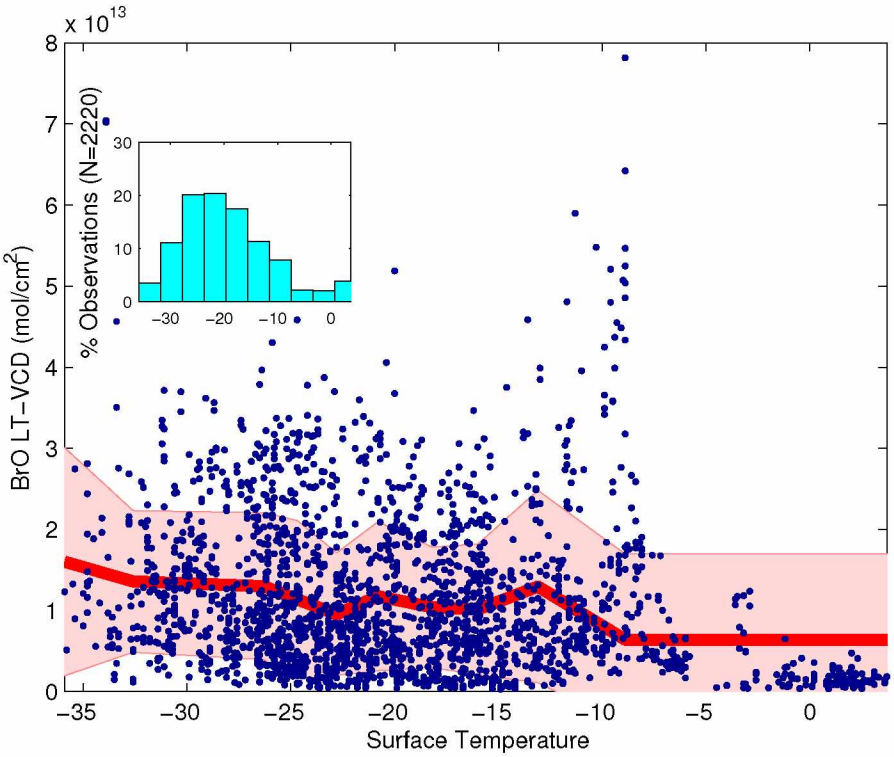

Figure 5.1: Observed BrO LT-VCD at the BARC building versus the near surface air temperature (R=-0.20). The red line represents the mean LT-VCD as a function of temperature, calculated from deciles on the x axis, while the outlined region represents one standard deviation. The inset histogram shows the overall percentage of observations taking place at various temperatures.

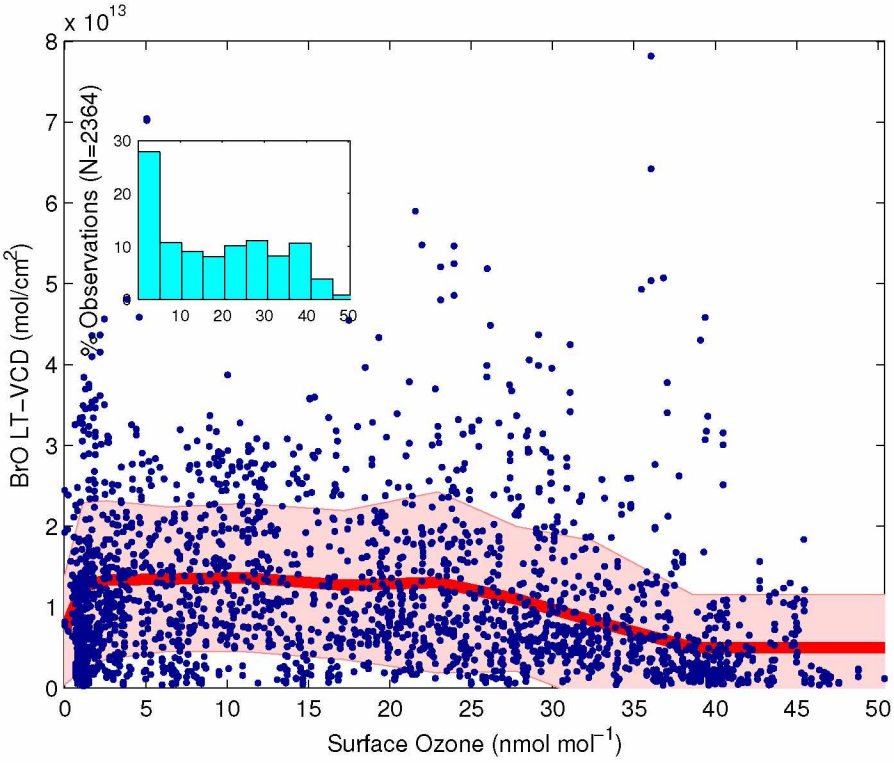

Figure 5.2: Observed BrO LT-VCD at the BARC building versus the near surface ozone (R=-0.15). The red line represents the mean LT-VCD as a function of ozone mixing ratio, calculated from deciles on the x axis, while the outlined region represents one standard deviation. The inset histogram shows the overall percentage of observations taking place at various ozone mixing ratios.

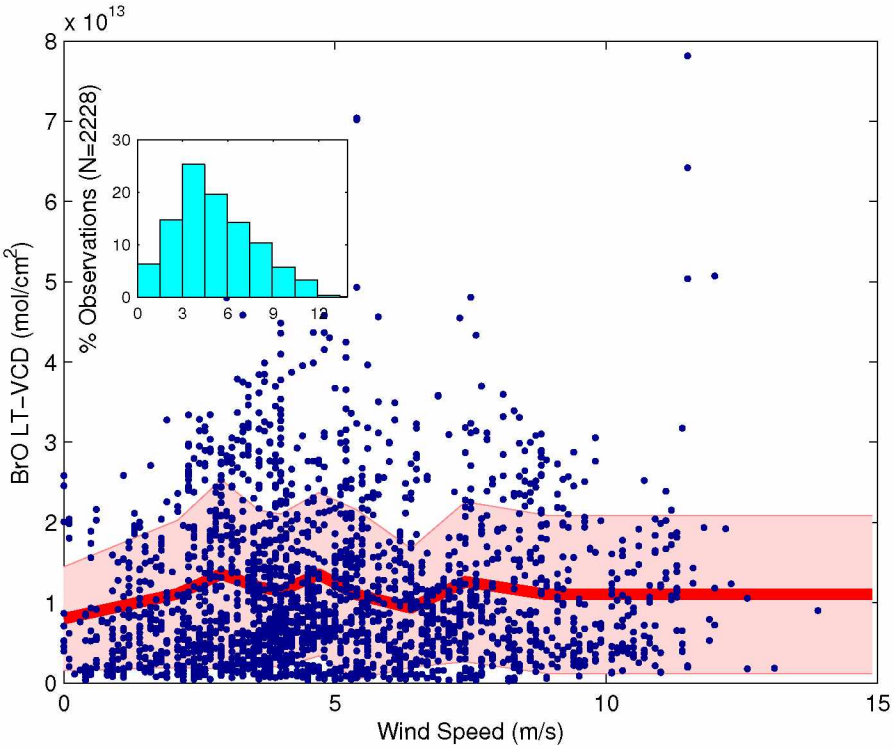

Figure 5.3: Observed BrO LT-VCD at the BARC building versus the near surface wind speed (R=0.03). The red line represents the mean LT-VCD as a function of wind speed, calculated from deciles on the x axis, while the outlined region represents one standard deviation. The inset histogram shows the overall percentage of observations taking place at various wind speeds.

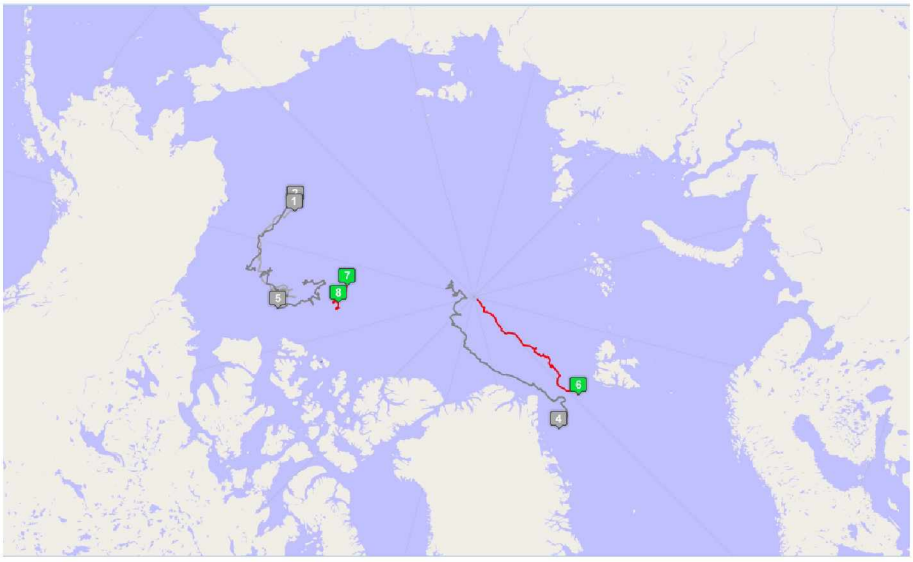

Figure 5.4: Examples of various instrument deployment locations. Locations of instruments active at the time of this screen capture are shown in green, with GPS tracks in red indicate locations of previous measurements. Gray labels and tracks indicate previously deployed instruments.

Appendix A

Supplementary Information for "Meteorological Controls on the Vertical Distribution of Bromine Monoxide in the Lower Troposphere"

A.1 2.1 MAX-DOAS measurements

Table A.1 gives the dSCD retrieval errors as a function of elevation angle.

A.2 2.4 Reduction of the Full Profile

Figures A.1 and A.2 show the remainder of the timeseries shown in Fig. 4 of the manuscript.

A.3 2.5 Other Fieldsites

The sampling inlet used was nearly identical to that described by Liao et al. (2011). The outer portion of the inlet was a 4.6 cm ID aluminum pipe that extended $\approx$ 9 cm beyond the wall of the sampling building. A blower was used to pull a total flow of $\approx$ 300 lpm through 33 cm of the aluminum pipe. 7.4 lpm of this flow was sampled into a 30°C heated 25 cm, 0.65 cm ID PFA path that included a custom three-way valve for calibration and background measurements. Following the valve, 2.0 lpm entered the CIMS flow reactor through a 0.51 mm diameter orifice. $I \cdot (H_2O)_n^-$ was produced in the flow reactor by passing 1.7 lpm of 5 ppm methyl iodide (CH_3I) in N_2 through a 210Po ionizer with water addition in N_2 (0.12 lpm) from a room temperature ($\approx$ 20°C) 1 L bubbler to the flow reactor, which was held at a constant pressure of 13 Torr. The primary difference between the CIMS instrument used by Liao et al. (2011) and that used herein is that two 77 l/s turbomolecular pumps are utilized on the vacuum region instead of two 250 ls^{-1} pumps. In addition, the quadrupole mass analyzer has a 9 mm o.d. compared to 18 mm (Liao et al., 2011).

Ambient CIMS measurements were interrupted for other experiments, as well as backgrounds and calibrations. Glass wool, used for the background scrubber, has been shown to remove halogen species at $>$ 95% efficiency (Neuman et al., 2010; Liao et al., 2012). CIMS sensitivity to Br_2 varied through the BROMEX study depending on H2O addition and detector sensitivity. Correspondingly, BrO sensitivity (at mass 224) ranged from 2-16 Hz per ppt. To account for this changing sensitivity, the signals were normalized to the reagent ion at mass 147 ($I \cdot (H_2^{18}O)^-$). The normalized calibration Br_2 calibration factor, defined as mass 287/([Br_2]*mass 147) was 0.00270 ($\pm$0.00008) Hz Hz^{-1} mol $pmol^{-1}$. A relative sensitivity of BrO (mass 224) relative to Br_2 (mass 287) of 0.47 was utilized for BrO calibration Liao et al. (2011).

A.4 References

Liao, J., Sihler, H., Huey, L. G., Neuman, J. A., Tanner, D. J., Friess, U., Platt, U., Flocke, F. M., Orlando, J. J., Shepson, P. B., Beine, H. J., Weinheimer, A. J., Sjostedt, S. J., Nowak, J. B., Knapp, D. J., Staebler, R. M., Zheng, W., Sander, R., Hall, S. R., and Ullmann, K.: A comparison of Arctic BrO measurements by chemical ionization mass spectrometry and long path-differential optical absorption spectroscopy, Journal of Geophysical Research, 116, 1–14, doi: 10.1029/2010JD014788, URL http://www.agu.org/pubs/crossref/2011/2010JD014788.shtml, 2011.

Liao, J., Huey, L. G., Tanner, D. J., Flocke, F. M., Orlando, J. J., Neuman, J. A., Nowak, J. B., Weinheimer, A. J., Hall, S. R., Smith, J. N., Fried, A., Staebler, R. M., Wang, Y., Koo, J.-H., Cantrell, C. A., Weibring, P., Walega, J., Knapp, D. J., Shepson, P. B., and Stephens, C. R.: Observations of inorganic bromine (HOBr, BrO, and Br 2) speciation at Barrow, Alaska, in spring 2009, Journal of Geophysical Research, 117, D00R16, doi: 10.1029/2011JD016641, URL http://doi.wiley.com/10.1029/2011JD016641, 2012.

Neuman, J. A., Nowak, J. B., Huey, L. G., Burkholder, J. B., Dibb, J. E., Holloway, J. S., Liao, J., Peischl, J., Roberts, J. M., Ryerson, T. B., Scheuer, E., Stark, H., Stickel, R. E., Tanner, D. J., and Weinheimer, a.: Bromine measurements in ozone depleted air over the Arctic Ocean, Atmospheric Chemistry and Physics, 10, 6503–6514, doi: 10.5194/acp-10-6503-2010, URL http://www.atmos-chem-phys.net/10/6503/2010/, 2010.

Table A.1: 1σ errors for MAX-DOAS fitting over all elevation angles.

Elevation Angle	Mean RMS	Mean BrO dSCD Error	Mean O_4 dSCD Error
1 Degree	4.1×10^{-4}	2.0×10^{13} molecules cm^{-2}	5.4×10^{41} molecules^2 cm^{-5}
2 Degree	4.0×10^{-4}	1.9×10^{13} molecules cm^{-2}	5.3×10^{41} molecules^2 cm^{-5}
5 Degree	3.9×10^{-4}	1.9×10^{13} molecules cm^{-2}	5.2×10^{41} molecules^2 cm^{-5}
10 Degree	3.8×10^{-4}	1.8×10^{13} molecules cm^{-2}	5.0×10^{41} molecules^2 cm^{-5}
20 Degree	3.6×10^{-4}	1.7×10^{13} molecules cm^{-2}	4.7×10^{41} molecules^2 cm^{-5}

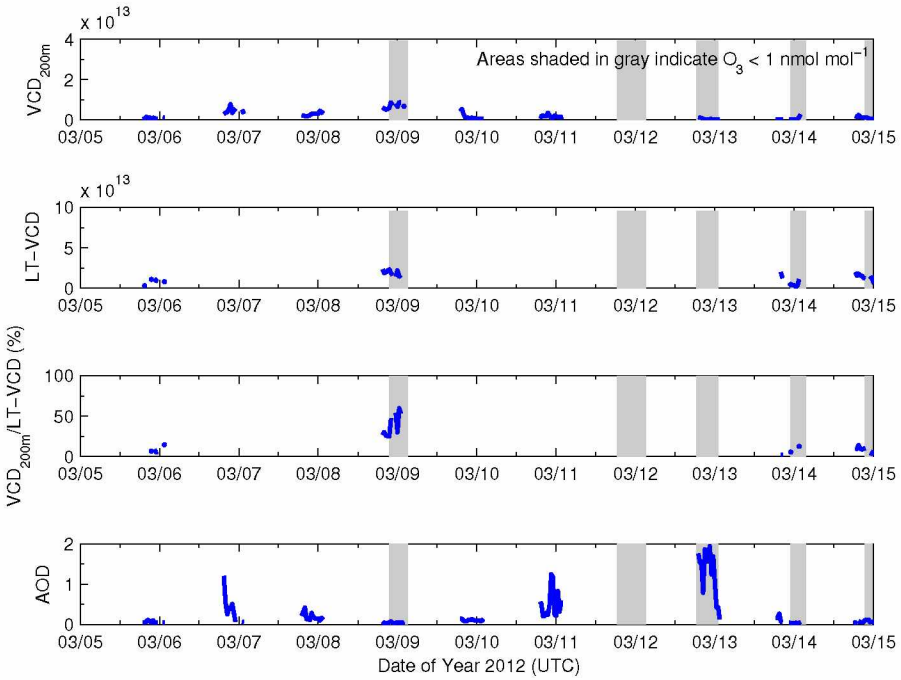

Figure A.1: A portion of the timeseries of BrO observed during this study. The top panel represents the VCD_{200}, the second panel represents the LT-VCD, both of which have units of molecules cm^{-2}. The third panel shows the percentage of the LT-VCD observed in the lowest 200m, while the bottom panel shows the aerosol optical depth over the course of this study. In the third panel, ratios are not calculated for events that have a LT-VCD below 5×10^{12}molecules cm^{-2}. Shaded areas represent potentially titrated air masses near the surface (Ozone $<$ 1nmol/mol).

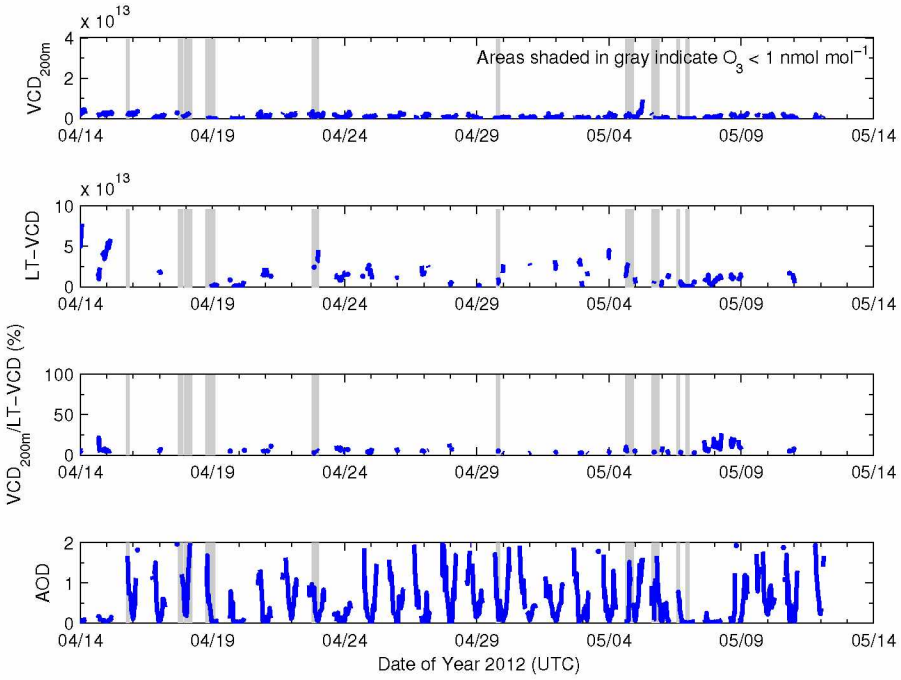

Figure A.2: A portion of the timeseries of BrO observed during this study. The top panel represents the VCD_{200}, the second panel represents the LT-VCD, both of which have units of molecules cm^{-2}. The third panel shows the percentage of the LT-VCD observed in the lowest 200m, while the bottom panel shows the aerosol optical depth over the course of this study. In the third panel, ratios are not calculated for events that have a LT-VCD below 5×10^{12}molecules cm^{-2}. Shaded areas represent potentially titrated air masses near the surface (Ozone $<$ 1nmol/mol).

Appendix B

Supplementary Information for "Interannual Variability of Observed Bromine Monoxide Over a Four Year Period at Barrow, Alaska"

B.1 5.1 Influence of FYI on BrO

Figure B.1 shows the relationship between unprocessed low elevation dSCD data and time spent in FYI areas. As discussed in the main text, the overall linear correlation (R=0.40) is similar to the linear correlation between processed LT-VCDs and time in FYI areas.

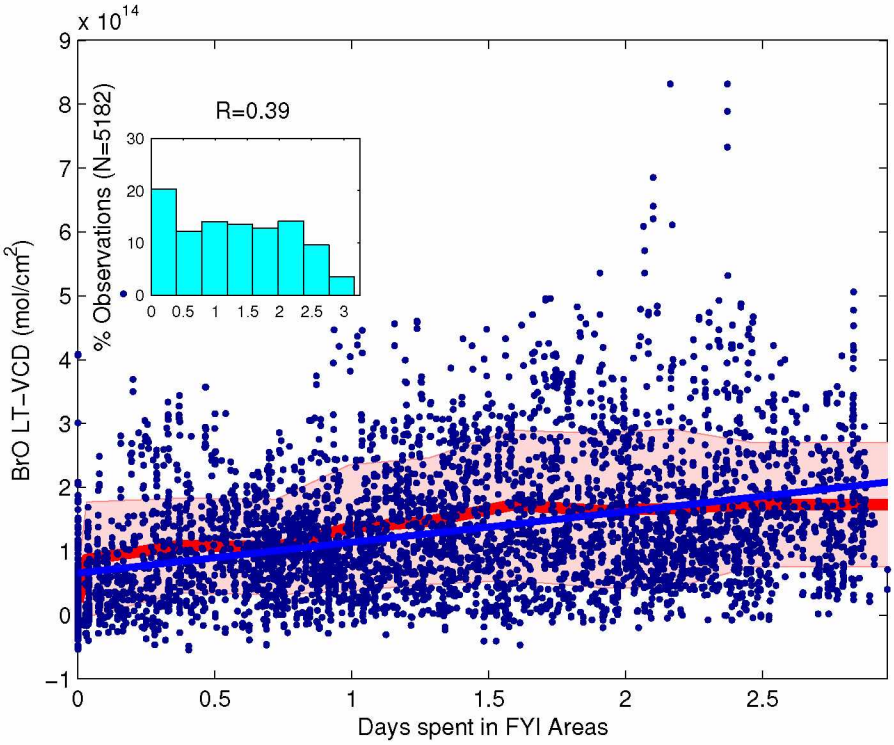

Figure B.1: Observed BrO 2 degree dSCD data at the BARC building versus time spent in FYI areas. The red line represents the mean LT-VCD as a function of time spent in FYI areas, calculated from deciles on the x axis, while the shaded region represents one standard deviation. The inset histogram shows the overall percentage of observations taking place at various amounts of time in contact with sea ice.